OUKA
The University of Osaka
Institutional Knowledge Archive

Title	An Analytical Method for Microstructure-Property Linkages Using Machine Learning and Computer Simulations
Author(s)	小島, 隆嗣
Citation	大阪大学, 2022, 博士論文
Version Type	VoR
URL	https://doi.org/10.18910/88054
rights	
Note	

The University of Osaka Institutional Knowledge Archive : OUKA

https://ir.library.osaka-u.ac.jp/

The University of Osaka

Doctoral Dissertation

An Analytical Method for Microstructure-Property Linkages Using Machine Learning and Computer Simulations

（機械学習と数値計算を用いた微細構造と材料特性の関係に関する解析手法）

Takashi Kojima

January 2022

Graduate School of Engineering
Osaka University

Preface

This dissertation presents my research on microstructure–property linkages using machine learning and computer simulation. The dissertation is the result of the studies in my Ph.D. course at the Division of Electrical, Electronic and Infocommunications Engineering, Graduate School of Engineering, Osaka University. In this dissertation, we propose a novel methodology to clarify the microstructure-property linkage using a new exploration method and a new analytical method on the microstructure using the machine learning. The proposed methodology is applied to a microstructure of filled rubber which is a main material of tire. This dissertation is organized as follows.

Chapter 1 describes the background, the motivation, and the purpose of this research. First, a filled rubber is explained. Then, we describe achievements and issues of experimental studies and computer simulation-based studies on the filled rubber in the past. Next, recent advantages of the material science using the machine learning are mentioned. Lastly, we explain the purpose of this study.

Chapter 2 proposes a high-speed simulator of filled rubber, which replaces the coarse-grained molecular dynamics (CGMD) simulation, using machine learning. This technique allows us to perform an extremely fast iterative sampling of the microstructure needed in following Chapter 3. In this study, a surrogate model using a convolutional neural network (CNN) is introduced for developing the high-speed simulator. It is reported that the microstructure in filled rubber has a hierarchal structure of aggregates composed of the filler particles. Hence, we establish the high-speed simulator which can predict the material properties in the arbitrary space scale. We demonstrate the superior prediction accuracy of the high-speed simulator through numerical examples.

In Chapter 3, we propose a sampling method to find the microstruc-

tures providing the desired property. First, we establish a method to analyze the relation between a given microstructure and material properties induced by the change of the microstructure in the course of the deformation through CGMD simulations. However, this analysis does not find a microstructure inducing the desired mechanical properties. Some novel technique must be established to automatically search a microstructure inducing the desired properties and to clarify the induction mechanism. To address this issue, we propose an efficient sampling method for the complex microstructure inducing given properties. The method is a combination of the replica exchange Markov chain Monte Carlo methods (RXMCMC) and the gradient descent method. The RXMCMC searches the microstructure in a discrete representation space of the microstructure globally, and the succeeding gradient descent method searches locally to find the microstructure providing better desired properties. In these sampling, the high-speed simulator introduced in Chapter 2 is employed to efficiently compute the mechanical property and its dependence on the microstructure for the efficient sampling. Finally, CGMD simulations are carried out to confirm the material properties of the searched microstructures. The efficiency of the proposed method is evaluated through numerical examples.

Chapter 4 proposes methods for quantitatively analyzing the microstructures obtained in Chapter 3. Two machine learning techniques are developed to extract core parts in the complex microstructure that induce the desired properties. The first method is based on a logistic regression analysis. The microstructure is quantified by persistent homology, and the core parts in the microstructure are extracted based on the trained regression coefficients. The other is a CNN based method. The core parts strongly contributing to the desired properties are highlighted by the convolution filer learnt in the CNN. Comparing the results of both methods, we clarify the features of the core parts in the microstructure and their induction mechanism of the desired properties. Lastly, the numerical simulations are performed to demonstrate

the validity of the insights obtained by our proposed method.

Chapter 5 concludes this dissertation.

Acknowledgment

I worked on this dissertation under the supervision of Prof. Takashi Washio. I would firstly like to express my sincere gratitude to him for sharing his knowledge, providing useful discussions, and pushing me to work hard.

I would also like to express my appreciation to Associate Prof. Satoshi Hara for useful discussions and his constructive suggestions.

I would like to thank Mr. Masaki Noro, CTO of The Yokohama Rubber Co.,Ltd., and Mr. Takashi Shirokawa, Associate Officer and Head of Materials Technologies Dept., for providing me this precious opportunity as a Ph.D student in Osaka University. I would like to acknowledge Dr. Masataka Koishi, Executive Fellow and Head of AI Laboratory, for his continuous support.

Finally, I would like to give special thanks to all of the people who have been involved in this research.

Contents

Chapter 1 Introduction **3**

1.1 Background 3

1.2 Purpose of this study 10

Chapter 2 CNN-based surrogate model of CGMD simulation **12**

2.1 Introduction 12

2.2 Problem setting for filled rubber 13

2.3 Data for CNN-based surrogate model 14

2.3.1 Determination of filler morphology 14

2.3.2 CGDM-measured stresses of the morphologies 16

2.3.3 Data augmentation procedure 20

2.4 Configuration of CNN-based surrogate model 24

2.5 Training of the CNN-based surrogate model and its performance evaluation 24

2.5.1 Data sets for constructing the CNN-based surrogate model . 24

2.5.2 Training of the CNN-based surrogate model 25

2.5.3 Influence of an input image size and its fringe size on accuracy 25

2.5.4 Extrapolation accuracy of CNN-based surrogate model using the test data 27

2.6 Conclusion 30

Chapter 3 Search Strategy for Rare Microstructure to Optimize Material Properties **31**

3.1 Introduction 31

3.2 Preliminary studies 33

3.3 Problem setting for filled rubber microstructure 37

3.4 Exploration method for rare filler morphology 38
3.4.1 Replica exchange MCMC for filler morphology search 39
3.4.2 Filler morphology search using the gradient ascent method . 42
3.4.3 Validation simulation of the mechanical property using computer simulation 44
3.5 Exploration performance 46
3.6 Insights on optimal filter morphologies 51
3.7 Conclusion 55

Chapter 4 Analysis on Microstructure-Property Linkages 57
4.1 Introduction 57
4.2 Problem setting for filled rubber analysis 58
4.3 Analysis method for filler morphology 61
4.3.1 LR and PH analysis 62
4.3.2 CNN–based analysis 68
4.4 Analysis result 74
4.4.1 Filler aggregates extracted by the PH and CNN methods . . 74
4.4.2 Comparison between the extracted and non-extracted filler particles 81
4.5 Validation using computer simulation 84
4.6 Conclusion 87

Chapter 5 Conclusion 88
5.1 Discussion 88
5.2 Conclusion 89

Appendix 105
A CGMD simulation 105

List of Figures

1.1 (a)Measured stress-strain curves of uniform dispersion sample and nonuniform dispersion sample, and (b) Transmission Electron Microscope (TEM) images of filled rubber. 9

2.1 Methodology of determining the filler configuration: (a) 1st step; (b) 2nd step. In the 1st step, aggregate regions where filler particles are able to be placed and exclusion polymers where the filler particles are not placed are designed. In the following 2nd step, specified number of filler particles are distributed in the aggregate regions. 15

2.2 Distributions of four input parameters for filler morphology to generate the training data for the CNN-based surrogate model. Distributions of all parameters were designed to produce the high modulus. 17

2.3 Example of visualized filler configuration. The green box is the entire region of the large-scale CGMD simulation. The red particles are the filler particles. The radius and expected values of the aggregate, the volume fraction, and the expected values of the exclusion polymer are (a) 0.7,0.3,0.3,0.1, (b) 0.7,0.6,0.5,0.1, (c) 0.8,0.6,0.5,0.1, (d) 1.0,1.0,0.1,1.0, (e) 1.5,1.0,0.1,1.0, and (f) 2.0,2.0,0.1,1.0, respectively. 18

2.4 Stress-Strain curves measured by CGMD up to a strain of 0.3. Each line represents the Stress-Strain curve induced by the filler morphology. 19

2.5 Example of a filler configuration and 3D image: (a) Visualized filler configuration and (b) 3D image. 22

2.6 Schematic for training data instance composed of the imaged filler morphology information (input data) and the material property (output data). Imaged region of dotted red frame in bottom figure is slightly larger than the green region where material property is measured, because outside region of the green region influences on the property of the green region. The material property results from the large-scale CGMD simulation. 22

2.7 Distributions of stress in the training data. The blue bars and the orange bars represent the stresses in the divided region of the CGMD space and the entire CGMD region, respectively. 23

2.8 CNN architecture. 24

2.9 Relationship between fringe size and prediction accuracy. The prediction accuracy is a ratio of the predicted stress by the CNN-based surrogate model to the CGMD-measured stress. 26

2.10 Relationship between the middle-scale region and the prediction accuracy. The prediction accuracy is the ratio of the predicted stress by the CNN-based surrogate model to the CGMD-measured stress. Here, the fringe size was 10 [σ]. 28

2.11 Comparison of the prediction stresses by the CNN-based surrogate model trained by the divided regions and the references. The results of the proposed method were compared with the stresses predicted by the CNN-based surrogate model trained by the entire regions of the CGMD simulation. 29

3.1 Filler positions for large-scale CGMD: (a) aggregated model, (b) uniformity arranged model. Red dots and green domain represent filler particles and polymer phase, respectively. 34

3.2 Simulated stress-strain curves of the uniformity arranged model and the aggregated model. 34

3.3 Decomposed stress-strain curves of the uniformity arranged model and the aggregated model: (a) bond stress and (b) nonbond stress. 35

3.4 Decomposed bond stress-strain curves of the uniformity arranged model and the aggregated model: (a) filler phase and (b) polymer phase. 36

3.5 The change in the number of aggregates during the deformation. . . 36

3.6 Result of the random sampling: (a) is the distribution of stress at strain of 0.3. (b) is a plot of the number of filler particles and stress. The stress is roughly proportional to the number of filler particles. Approximately 250 fillers are needed to reach the stress of 0.6, which is the sampling objective. 38

3.7 Schematic for extracting filler morphologies used as an initial state in the gradient ascent method from a history of replica exchange MCMC. Three morphologies were extracted in this example history. 43

3.8 Schematic drawing of the proposed method. Circles in the Step-1 represent the filler candidate positions. The filler morphologies are defined by a set of the candidate points in order to discretize the filler morphology space. The discretization of the morphology allows the morphology exploration in the wide range. Open circles and filled circles are polymer and filler, respectively. The left figure in the Step-2 is the initial state of this step, which is obtained by Step-1. In this step, the local filler morphology space is searched by the update of the filler positions as a continuous value. The right figure shows an updated filler configuration. 44

3.9 Target distributions of each temperature. The blue line, $t = t_1$, is the probability distribution at the lowest temperature. The red line, $t = t_4$, is the probability distribution at the highest temperature. The orange and green lines, $t = t_2$ and $t = t_3$, are the probabilities at the temperatures between and $t = t_1$. 48

3.10 Distributions of the CGMD-measured stress of the morphologies obtained by each method. These histograms are normalized and the width of bins is 0.02. Arrows of the same colors with the distributions represents the averages of each stress distribution. The proposed method presents the larger stress distribution than the other methods. This result elucidates the high sampling performance of the proposed method. 50

3.11 Stress distributions of the morphologies obtained by the proposed method and the morphologies sampled by the random sampling based on our existing knowledge. These histograms are normalized and the width of bins is 0.02. The resultant stresses of the proposed method exceed the stress of 0.4, which is in the top 3.5 % of the random sampling. 52

3.12 Schematic diagram illustrating the PH. (a)The balls are disconnected when the ball radius r is smaller. A loop emerges at $r_1 = \sqrt{b_1}$. Another loop emerges at $r_2 = \sqrt{b_2}$, and disappears at $r_3 = \sqrt{d_2}$. A newly loop emerges at $r_4 = \sqrt{b_3}$. The loops emerged at $r_2 = \sqrt{b_2}$ and $r_4 = \sqrt{b_3}$ disappears at $r_5 = \sqrt{d_1} = \sqrt{d_3}$. (d) PD representing the results of PH analysis. 53

3.13 Persistent diagrams: (a) filler morphologies obtained by the random sampling, the morphology on the upper left provided the stress over 0.65, while the other morphologies provided the stress from 0.6 to 0.65, and (b) filler morphologies, which provided the stress over 0.65, sampled by the proposed method. Larger death length than the persistent diagrams of the random sampling implies there are the greater aggregates of filler particles in the morphologies obtained by the proposed method. 54

4.1 Stress distribution of the morphologies obtained by the random sampling and the proposed method in Chapter 3 with a filler volume fraction of 20 vol.%. 59

4.2 RDFs of the filler particles in the positive and negative examples. The blue lines denote the RDFs of the morphologies obtained by random sampling, and the orange lines represent the RDFs of the morphologies obtained in the study of Chapter 3. The solid and dotted lines show the RDFs of the negative and positive examples, respectively. 60

4.3 Schematic illustration of the vectorization procedure. The left plots include the PDs; the center figures are the persistence surfaces; and the right histograms contain the PIs. Two morphologies are vectorized in the upper and lower figure panels. As shown in the upper center figure, the persistence surface is divided by a grid, and representative values of all grid cell are arranged along the green arrows. 63

4.4 Prediction accuracies of the validation data with different combination of hyperparameters. The accuracy was defined as the ratio of the number of morphologies that predicted the correct class to the number of validation data instances. The top row in the horizontal axis is the weight on the persistence surface β; the middle row is the standard deviation of the Gaussian distribution h; and the bottom row is the number of subdomains g. The orange bar represents the combination of parameters that produces the highest accuracy. . . . 65

4.5 Distribution of the L1 regularized LR coefficient, which predicts a stress-based class from the vectorized filler morphology. The coefficient is visualized in the PD space. The red region corresponds to the positive coefficients and contributes to the positive example. The blue region corresponds to the negative coefficients and contributes to the negative example. 66

4.6 Examples of the loops composed of filler particles, which were extracted by the PH. The green box denotes the modeled space, and the red dots represent the filler particles. 67

4.7 CNN architecture utilized in this work. The numbers in parentheses represent the dataset sizes. The input image of $32 \times 32 \times 32$ pixels is convoluted into the image of $32 \times 32 \times 32$ pixels under the periodic boundary conditions with a single kernel. The leaky ReLU function and global average pooling were applied to the convoluted image to reduce the dimension. Finally, the probability of the positive example is output using the sigmoid function. 69

4.8 Relationships between the epoch number and prediction accuracy determined by applying the validation data. The prediction accuracy was equal to the ratio of the number of morphologies that predicted the correct class to the number of validation data instances. The blue line, orange line, and green line correspond to the prediction accuracies of the kernels with sizes of $5 \times 5 \times 5$, $9 \times 9 \times 9$, and $13 \times 13 \times 13$, respectively. 70

4.9 Input and convoluted images obtained using the kernels with sizes of $5 \times 5 \times 5$, $9 \times 9 \times 9$, and $13 \times 13 \times 13$. The left figure of $9 \times 9 \times 9$ and the upper figures of $5 \times 5 \times 5$ and $13 \times 13 \times 13$ represent the superimposed images of input and convoluted images. The white circles and black areas denote the filler particles and rubber regions in the input images, respectively. The red and blue areas are visualized in the convoluted images depicted in the lower row and represent the pixels with positive and negative values, respectively. The red areas contribute to the positive example, and the blue areas contribute to the negative example. The pixels with values ranging from -0.3 to 0.3 are visualized in black to emphasize the areas with large contributions. 72

4.10 Ratio of the positive pixels in the convoluted image to the filler particles in the input image, which was defined as an A/B fraction. These histograms are normalized. Here, A is the number of pixels with positive values in the convoluted image that overlap with the filler particles in the input image. B is the total number of pixels with positive values in the convoluted image. The blue, orange, and green colors correspond to the kernel sizes $5 \times 5 \times 5$, $9 \times 9 \times 9$, and $13 \times 13 \times 13$, respectively. 73

4.11 Normalized histograms of the radius of gyration, R_g, and the number of filler particles in the loop, F, of the filler aggregate extracted by the PH. The blue bars and orange bars denote the aggregates extracted from the positive and negative examples, respectively. 75

4.12 (a) Definition of the aggregate size. The red circles and black points represent the filler particles and their centers, respectively. The size in each direction is the difference between the largest and smallest coordinates along this direction. (b) Aggregate size distribution in each direction. The blue and orange bars denote the results obtained for the positive and the negative examples, respectively. Z-direction is the elongation direction of the system, while X- and Y-directions are compressed during deformation. 76

4.13 Schematic illustration of the filler particles belonging to multiple loops. The blue and red circles denote the filler particles constituting different loops. The particles surrounded by the orange circle belong to both the i-th and j-th loops connected physically. However, these two loops are considered different aggregates. 77

4.14 Example of the aggregate extracted by the CNN and size distributions of filler aggregates. (a) Cross-section of the convoluted image. The aggregate size is defined as the difference between the largest and smallest pixel coordinates. The red/blue regions are the set of pixels with positive/negative values that contributes to the positive/negative example, respectively. The black region includes pixels with small values ranging from -0.3 to 0.3 and does not affect the output. The adjacent red pixels are extracted under the periodic boundary conditions. (b) Histograms of the size of the set of pixels with positive values, namely aggregate sizes, obtained from all morphologies in the positive (blue bars) and negative (orange bars) examples. Z is the elongation direction of the system. 78

4.15 Fractions of the filler particles extracted by the PH and CNN that contributed to the positive example. Their values were computed as the ratios of the numbers of pixels of the extracted particles to the number of pixels for all filler particles. The blue bars denote the ratios of the filler particles extracted by the CNN method only; the orange bars represent the ratios of the filler particles extracted by the PH method only; and the green bars denote ratios of the filler particles common to the fillers extracted by the CNN and the fillers extracted by the PH. 80

4.16 Spatial correlations in the YZ plane of r-space including $r = (0, 0, 0)$ of the CNN-extracted fillers from all morphology examples that contribute to the high stress and that of the non-extracted fillers (upper row figures). The isotropic spatial correlation of the fillers not extracted by the CNN suggests the isotropically shaped filler aggregates. Meanwhile, the anisotropic spatial correlation of the filler particles extracted by the CNN indicates that the probability of filler orientation along the elongation direction is high. Furthermore, bottom two figures show the spatial correlations of the extracted fillers from all positive examples and all negative examples, respectively. The higher orientation probability of the filler particles extracted from the positive example along the elongation direction suggests that the aggregate size measured along the elongation direction in the positive example is larger than the size of the negative example. 83

4.17 Distributions of the CGMD-simulated stress at a strain of 0.3. The blue bars denote the results obtained for the CNN-extracted aggregates from the positive example. The Z-direction was the elongation direction. The orange bars represent the elongation of the CNN-extracted filler aggregates along the X- and Y-directions. The elongation direction was perpendicular to the aggregate principal direction (Z) in these cases. The green bars denote the results obtained for the filler configurations, in which the particle positions were randomly determined with the filler volume equal to that for the blue bars. Schematic diagrams of the filler aggregates and elongation direction are shown in the rectangles with the frame colors identical to those of the corresponding bars. The black circles and arrows designate the filler particles and the elongation direction, respectively. 86

A.1 Example of CGMD model: (a) presents the polymer chain consisted of 20,000 beads. The pink spheres represent the polymer beads. The orange cylinders represent the polymer bond defined by Equation (A.2). The interaction between polymer beads are represented by Lennard-Jones potential described in Equation (A.1). (b) presents the filler particle. Spheres colored in dark purple represent the filler bead, and light purple cylinders represent the bond connecting adjacent filler beads. The interaction between beads and bond potential are identical with those used for the polymer chains. 107

List of Tables

1.1 The methodology proposed in this dissertation and the objective of each chapter. 11

2.1 Parameter range for filler configurations. 17

3.1 Parameters for the morphology exploration. 47

3.2 Performance comparison of the random sampling method, the combined method of the random sampling and the gradient descent, the method using the replica exchange MCMC only, and the proposed method. 49

Chapter 1

Introduction

1.1 Background

Recently, tire manufactures have focused on the development of tire performance, such as rolling resistance, abrasion durability, steering stability, and wet traction, in order to adapt to the change of mobility society risen from CASE and MaaS [DJP20][GN21]. To improve tire performance, it is necessary to improve mechanical properties of filled rubber that is a main material of tire [KK17]. For instance, low energy dissipation, higher toughness, and higher elastic modulus are suitable for lower rolling resistance, higher abrasion durability, and better steering stability, respectively. The tire is required to maintain many performances at high levels, thus material engineer must design the filled rubber to balance many properties. The filled rubber is a composite material made of polymers and nanometer-scale fine filler particles, and their properties are directly related to tire performance via the filler morphology, because the material properties are influenced on the filler morphology [Dan75][BS00][SDG03][Klü03][DB93].

The "filler morphology" means distributions and shapes of clusters consist of filler particles. For example, Figure 1.1 presents two stress-strain responses induced by different filler morphologies: uniform dispersed morphology and nonuniform dispersed morphology. As shown in this figure, the worse dispersed morphology which includes the aggregated structure leads to a high stress. It is well known that other properties, e.g., the toughness and the hysteresis, as well as the stress are depend on the filler morphologies. Many researchers have engaged in studies to reveal the strong dependencies between the mechanical properties and the filler morhpologies since carbon black has been employed as the filler par-

ticle in the 1900s. A classical research is an experimental studies employed electronic microscope, X-ray scattering, and atomic force microscopy techniques (AFM) [VHK09][FLE+14][JS09][KMHX17][TNSM19][BGD+13].

The scanning electronic microscope and the transmission electronic microscope image the microstructires and enable us to evaluate the microstructures visually [VHK09][FLE+14][JS09]. AFM can measure an asperity of the surface and local material properties of nano-mater scale, e.g., adhesive energy and Young's modulus [KMHX17]. The material engineers can evaluate the microstructure using an image visualizing the distribution of the property. However, a quantitative comparison of microstructures is relatively difficult by using these techniques, because of the lack of technology that can evaluate the features of microstructure quantitatively from the imaged microstructure. In addition, the comparison of the initial/undeformed state of the microstructure is aspired by researchers, because the material property is induced by the change of the microstructure during the deformation. However, the observations of the identical local structure in both states are difficult even if the state of the art technology is used. The X-ray scattering is used to quantify the microstructure in both the initial state and the deformed state. This can measure intensities of the aggregate structures on each scale over a wide range from nanometer to millimeter [TNSM19][BGD+13]. However, the intensities cannot fully explain features of microstructure. Thus, detailed analysis of the microstructure is difficult. Furthermore, relations of the observed nanometer-scale structure and polymer chain dynamics have been formulated based on the statistical mechanics in order to quantify the impact of the structure. [VHK09][J.9][PK20][E. 45][DE90][LK12]. Nevertheless, there are serious barriers to relate the nanometer-scale structures with meter-scale properties.

To relate them clearly, following techniques are necessary.

- Observation of the complex three-dimensional microstructures.
- Grasp of changes of the morphologies during the deformation of a millimeter scale specimen.
- Investigation of a mechanisms of the material property induced by the change of the morphologies.

In addition, specimens providing desired property need to be prepared, in order to obtain insights on achieving the property. Regarding the first topics—observation of the complex three-dimensional microstructures—, we cannot directly and accurately observe the complex three-dimensional morphologies of given specimens except for their surfaces [AYY+08][JSK+07][WM04]. Even if we could grasp the three-dimensional morphologies of a specimen, its nanometer-scale structures strongly related to the meter-scale properties are hardly identified because of the variations of the nanometer-scale structures over the specimen [R.6]. Furthermore, deformations of the nanometer-scale structures cannot be easily related with the meter-scale properties, because the deformations are not easily evaluated due to lack of information on the initial states and their deformation processes of the structures [MNW+21]. Thus, the material engineers cannot investigate the mechanisms of the material property based on the deformation. In addition, the biggest issue is that the features of the morphologies leading to the desired material property cannot be revealed directly by the observed morphologies, because the material property of the examined specimen is inferior to the desired property, e.g., extremely high stress, and low energy dissipation. As a result, an extrapolation of the nanometer-scale structure based on the experimental result is required to improve the material property.

Computer simulations, on the other hand, can be used to visualize the inside of a tire and perform virtual experiments for tire design to improve the performance [BS00][KMK14]. Regarding the filled rubber, coarse grained molecular dynamics (CGMD) simulations have been applied to analyze the relationship between nanometer scale structure and meter-scale material properties [YQ14][GLS+14] [SBS03][FKR12][RME06][PRS+17]. For example, a dependency of cavity growth on molecular structure [YQ14] and an effect of an interaction between filler and polymer on the material property, such as the elastic modulus, rupture, and density are investigated [GLS+14][SBS03][FKR12][RME06][PRS+17]. Other examples of the targeted nanometer scale structures include, e.g., entanglements of polymer chains, cross linking, modified polymer chain end, variety of nano particles, and dynamics of polymer chains in the vicinity of filler during deformation. CGMD simulations are commonly used not only for material science but also for cell bi-

ology as well [BRHS+20][PS21]. The detail of the CGMD we used is explained in Appendix A. However, to the best of our knowledge, there have been no reports virtually succeeded to clarify the relationship between nanometer-scale structure and the targeted meter-scale material properties, e.g., high elastic moduli and low hysteresis, because the simulation can measure the material properties induced by the represented microstructure as an input file of each simulation. This means that simulation engineers are required to design the microstructure providing the desired property based on the experimental results or the existing knowledge. However, the features of such microstructures have not been clear. Hence, the simulation-resultant properties are inferior to the desired properties same as the experimental studies, due to the lack of the information of the core structure controlling the material property. Therefore, the simulation based study can hardly provide the new insights extraordinary outside the existing knowledge obtained by the experimental studies.

Recently, many exploration-exploitation strategies using machine learning (ML) have been reported, called "materials informatics (MI)" [RLK19][AC19] [MP16]. MI is the application of date science to problem in materials science for materials discovery and design. For example, data mining is employed to extract information from a large database of calculated properties, whether a given material has the potential to be a good property [CMWC14]. Another example is to construct a microstructure–property linkage using ML [IKT17][ISS+19], or constructing a many-body potential energy used in molecular dynamics simulation [HZCW18][ZHW+18][WOW+19]. One of the popular approaches of the combination with computer simulation is to use density functional theory (DFT) methods to calculate properties of, e.g., thermoelectrics, ferroelectrics, battery cathodes, hydrogen storage material, and polymer dielectrics [ZHW+18][LBXY19] [CSW+12] [DCN+16][KDL+19]. With the exception of DFT, finite element method (FEM) is used to calculate the material properties of composites [YYJ+19][LWK19][YCHB21]. However, it is difficult to apply the combination of DFT or FEM and ML to the study on filled rubber, because of the large-scale gap between the filler morphologies (nanometer-scale) and DFT (femtometer-scale) or FEM (millimeter-scale). Furthermore, most of the past studies employed a Bayesian optimization to explore

the desired material and exploit the data [SLA12][Moc89]. Features representing the microstructures are required to use the Bayesian optimization, because it is a method for searching an optimal combination of 10 parameters at most. However, a technique explaining the filler morphology with the small number of features is not been established. An traditional way to explaining the features of the filler morphology is a radial distribution function which describes how density varies as a function of distance from a reference particle [EM95]. Another way is a spatial correlation function, which can consider the direction of the radial distribution [TBC88]. In addition, ML has been used to establish the features of filler morphology recently [APM$^+$21]. Nevertheless, the features which can successfully explain the complex filler morphology has not been established yet. To the best our knowledge, there is no reports addressed the analysis on the complex microstructure using ML.

The best way to study the relationship would be exploration and analysis of filler morphologies to extract the common nanometer-scale structures or features that induce the desired material properties, like as proposed in many examples of MI [CZN$^+$21][TAP$^+$19]. These past studies worked on the exploration of the desired material by solving an inverse problem. The inverse problem is a methodology to search the material providing the designated property. Exploration of the filler morphology means creating new filler morphology candidates, measuring a material property, and selecting filler morphologies providing the desired property. The two major barriers to filler morphology exploration are "the huge computational cost" and "the lack of effective exploration techniques". Several months of computation is often required to carry out a large-scale CGMD simulation that includes thousands of filler particles. Hence, the CGMD cannot be used for the iterative exploration. Regarding the exploration techniques, two types of methods have been suggested for generating possible filler morphologies: probabilistic methods such as generating filler positions based on the Poisson point process [FJF$^+$16], and deterministic methods that directly determine each filler position [HTH$^+$18][HAK$^+$07][HTH$^+$08][Tak13]. In the probabilistic methods, the stochastic parameters characterizing the filler morphology that induces the desired material properties are not easily searched, because material properties largely vary depending on the randomly sampled filler morphologies even under the same parameters

[MF17]. In the deterministic methods, the filler morphologies are fixed by the input parameters, which are the coordinates of each filler particle in a three-dimensional space. An issue concerning the deterministic methods is that the number of target parameters increases dramatically with the number of filler particles (n) as $O(n)$, which prevents sufficient morphology sampling. In addition to the two issues concerning the exploration technique: "the huge computational cost" and "the lack of effective exploration techniques", "the lack of analytical techniques" is also a challenge to be addressed. The analysis of the microstrucure means the identifying common structures or features among the desired mirostructures in order to reveal the core parts dominating the mechanical properties. To the best of our knowledge, the analysis method has not been established, whether based on experimental studies, computer simulation, or ML.

Summarising this section, the followings are the challenges to be addressed forward to the finding of the filler morpholgies providing the desired material property, e.g. extremely high stress or low energy dissipation.

- The huge computational cost.
- The lack of effective exploration techniques.
- The lack of analytical techniques.

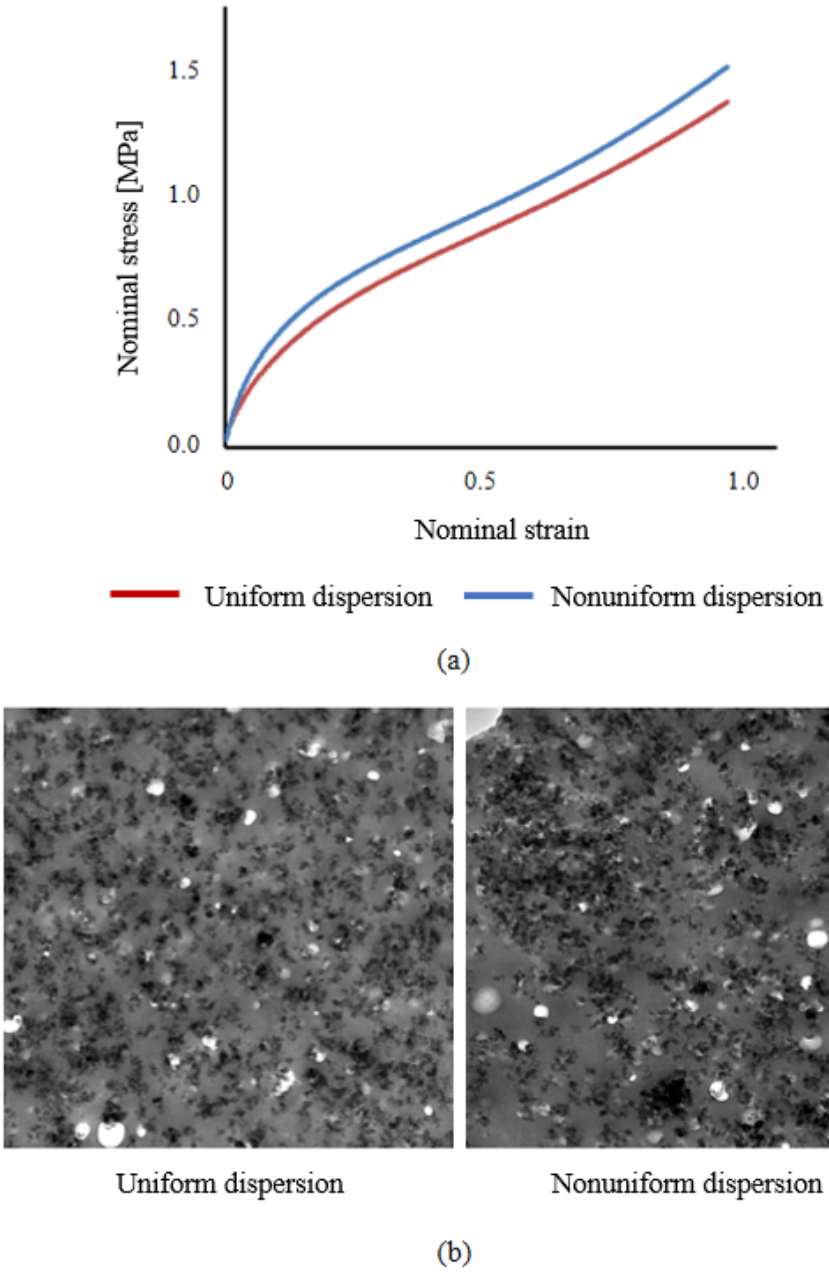


Figure 1.1: (a)Measured stress-strain curves of uniform dispersion sample and nonuniform dispersion sample, and (b) Transmission Electron Microscope (TEM) images of filled rubber.

1.2 Purpose of this study

As described in the previous section, there are mainly three barriers to reveal the features of the microstructures providing the desired property, i.e., "the huge computational cost", "the lack of effective exploration techniques", and "the lack of analytical techniques". These are more concretely paraphrased as "the computational cost for the iterative simulation during the exploration for the desired microstructure", "difficulty of finding desired microstrucrure", and "the methodology for microstructure analysis". In this dissertation, we propose a novel methodology to clarify the microstructure-property linkage using a new exploration method and a new analytical method on the microstrucrue by synthesis of computer simulation and machine learning. Namely, the purpose of this study is establishment of a novel methodology to directly find features of the desired microstructures. The proposed methodology enables us to discover the linkage between the microstructures and the desired material property which is outside the knowledge of material engineers.

To address the aforementioned three issues, we first introduce a high speed simulator in order to reduce "the huge computational cost" by replacing the CGMD simulation for an efficient morphology search. This high-speed simulator is established by ML and described in Chapter 2 (Presented in Journal: J-2). Second, we establish an efficient exploration method to find the microstructures providing the desired property in Chapter 3 (Presented in Journal: J-1, J-3, and J-5). The exploration method uses the high speed simulator. This technique resolve the problem "the lack of effective exploration techniques", and enable us to automatically explore of microstructures outside of the material engineers' knowledge. Last, in Chapter 4, an analytical methods for the microstructures is described (Presented in Journal and Conference: J-4 and C-1). We develop a methodology to extract common structures among the explored desired microstructures. This chapter works on the problem "the lack of analytical techniques". Table 1.1 presents the objectives of each chapter and the proposed methodology. Chapter 5 concludes this dissertation.

In Chapters 2, 3, and 4, application examples of each proposed method, which are to improve of the stress of filled rubber with the aim of improving the steering stability, are presented.

Table 1.1: The methodology proposed in this dissertation and the objective of each chapter.

Chapter	Objective	Methodology
2	Reduction of the computational cost by introducing the surrogate model of CGMD for an efficient exploration.	Introduction of a high speed simulator established by ML.
3	Establishment of an efficient exploration method for microstructure providing desired material property.	An automated search of the microstructure outside of the engineers' knowledge.
4	Establishment of the analysis method of microstructure.	Feature analysis by extracting the common structures among the samples.

Chapter 2

CNN-based surrogate model of CGMD simulation

2.1 Introduction

As described in Chapter 1, the best way to study the microstructure-property linkage would be exploration and analysis of microstructure to extract the common structures or features that induce the desired material properties. The exploration microstructure means creating new microstructure candidates, measuring a material property, and selecting microstructures providing the desired property. However, computer simulations, e.g., CGMD simulation commonly used for the polymer material, cannot be used for the intensive exploration, because of the huge computational cost. Hence, we developed the surrogate model in order to reduce the computational cost dramatically and consummate the efficient intensive exploration by replacing the computer simulation with a surrogate model-based simulator.

A huge amount of the training data is needed in order to achieve a highly generalized performance of the surrogate model, when the machine learning technique is employed to establish a surrogate model. Because ML provides the interpolation function of the training data. However, it is infeasible to generate enough amount of training data using the CGMD simulation due to the simulation cost. In this Chapter, we introduce a surrogate large-scale CGMD model focusing on microstructure to provide fast and accurate predictions of a material property. The surrogate model is established by a convolutional neural network (CNN) that accepts the kinetic information of microstructure as input graphical image. Because one-to-one bidirectional conversion between the quantified microstructure, i.e., an input data

for the surrogate model, and the concrete microstructure, e.g., a set of the filler positions, is required.

The major difficulty with employing an ML-based surrogate model is the shortage of training data as already mentioned, owing to the huge computational cost required to create these data by using CGMD simulations. To overcome the technical difficulties, in this Chapter, we propose a method to generate a highly accurate surrogate model that succeeds with only a small number of large-scale CGMD results.

The remainder of this chapter is organized as follows. First, the problem for the surrogate model is explained in Section 2.2. In Section 2.3, the configuration of the training data is described. The procedure of the training and the resultant performance of the CNN-based surrogate model are presented in Section 2.4 and Section 2.5, respectively. The established CNN-based surrogate model is summarized in the last Section 2.6.

2.2 Problem setting for filled rubber

In this study, stress at a strain of 0.3 under uniaxial deformation was chosen as the target property. Tire manufacturers must balance tire performances against the mechanical properties of the nanometer-scale filler morphology and the resultant effects. For example, to improve the wear resistance or the steering stability, a high elastic modulus of the tire tread where contacts the road is preferred. Although, according to finite element method-based studies, the strain of most tire tread does not reach 0.05 during rolling, the tread deformation can locally reach a strain of 0.3, such as at the bottom of a groove [BS00][KOT77][Nak11]. Therefore, stress at a strain of 0.3 was regarded as the target property.

It is well known that the stress of filled rubber is roughly proportional to volume fraction of filler [E. 45][DTT$^+$19], and filler particles percolate beyond approximately from 22 vol.% to 25 vol.% [LLJ$^+$22]. Moreover, mechanical properties change once filler particles percolate [CZC$^+$14][KMAS96]. Based on these studies, we restricted the volume fraction of filler to 15 vol.% represented by 1000 filler particles with radius of 10 $[\sigma]$(σ: unit length used in the CGMD) in a space of

300 $[\sigma] \times 300\ [\sigma] \times 300\ [\sigma]$, in order to understand the mechanisms to generate the stress in a phase not having filler percolation.

2.3 Data for CNN-based surrogate model

2.3.1 Determination of filler morphology

In this study, an exploration of the morphologies providing the high modulus was performed as an application example of the proposed method. It is well known that aggregated structure increases the elastic modulus [Klü03][VHK09][HMDT16][KK18]. Hence, various aggregates were generated and the stresses induced by the aggregate were measured using CGMD. Filler morphologies were determined using multi-step Poisson point processes such that aggregated structures can be distributed effectively [FJF$^+$16] as shown in Figure 2.1. First, both the aggregate regions (where filler particles were placed) and their exclusion (where the filler particles were not placed but the polymers were) were designated. Then, the specified number of filler particles were placed in the aggregate regions.

The first step for defining the aggregate regions and the exclusion started by determining the number of the aggregate region, N_a, and that of the polymers in the exclusion, N_e. The input parameters were the radius of aggregate region, R_a, the volume fraction of the exclusion polymer, V_e, and the Poisson point process intensity of the aggregates, θ_a, and the polymers, θ_e. N_a and N_e were determined via Poisson point distributions of the expected values for each regions. The expected values for the aggregate region λ_a, and that for the exclusion λ_e were given by:

$$N_a = \lambda_a = V \times \theta_a, \tag{2.1}$$

$$N_e = \lambda_e = V \times \theta_e, \tag{2.2}$$

where V was the volume of the modeled space for the CGMD simulation. Then, the radius of the exclusion polymer, R_e, was determined as follows:

$$R_e = \left(\frac{-3 \times \log\left(1 - V_e\right)}{4 \times \pi \times \theta_e} \right)^{\frac{1}{3}}. \tag{2.3}$$

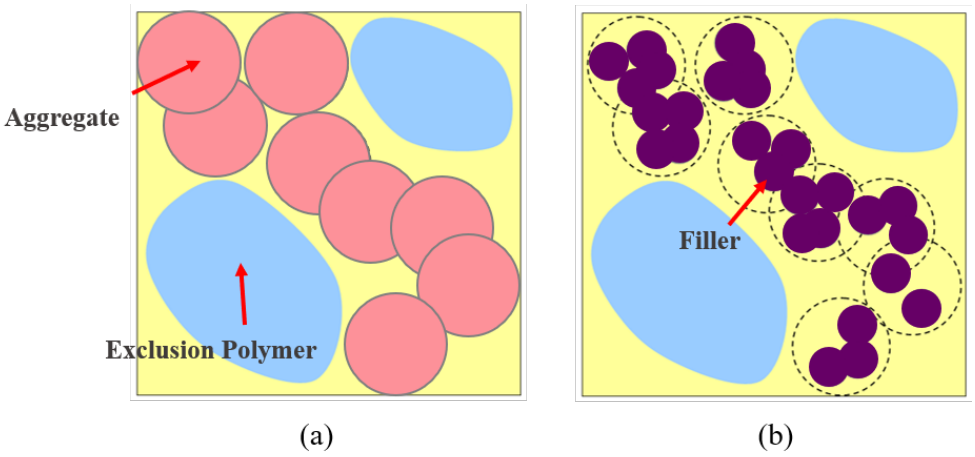


Figure 2.1: Methodology of determining the filler configuration: (a) 1st step; (b) 2nd step. In the 1st step, aggregate regions where filler particles are able to be placed and exclusion polymers where the filler particles are not placed are designed. In the following 2nd step, specified number of filler particles are distributed in the aggregate regions.

In the second step which determined the locations of filler particles, the specified number of filler particles were placed in the aggregate region based on the two given parameters; volume fraction, V_f, of the filler and filler-particle radius. If a filler candidate position determined by the random sampling was located in the aggregate regions, new filler particle was added at the candidate position. The new filler particles were located until the volume fraction of filler exceeded V_f. In this study, the radius of filler particles was 10 $[\sigma]$ as described in Section 2.2. Although the minimum distance between the centers of the filler particles should be 20 $[\sigma]$ to prevent their overlapping, we apply a minimal distance of 18 $[\sigma]$, because the smaller volume fraction of the aggregate region lowers the probability of model success. Thus, our filler particles overlap, and the configuration obtained by our multi-step process uses the molecular dynamics simulation algorithm to eliminate the overlaps. We selected parameters that likely produce high elasticity based on our prior knowledge, because we aimed to sample the high-elasticity morphologies. Specifically, many papers have reported that the elastic modulus increases when

the filler particles are aggregated [VHK09][HMDT16][KK18]. Hence, small values were used for the aggregate radius and the Poisson point process intensity for the aggregate. Meanwhile, a large volume fraction and small Poisson point process intensity were applied for the polymers in the exclusion, because the fraction of the aggregate region is small in the aggregated structure of the filler particles.

45 filler morphologies were created within the range of the parameters in the multi-step process described in Table 2.1. Figure 2.2 represents the 4 input parameter distributions of the filler configurations. Figure 2.3 shows 6 of the 45 morphologies. Here, a dimension of the cubic cell and number of filler particles were 300 [σ] and 1,000, respectively. The volume fraction of filler particles of all models was 15[%].

2.3.2 CGDM-measured stresses of the morphologies

Each filler configuration was merged with 1,000 polymer chains of 20,000 bead lengths modeled using the Kermer-Grest model [KG90]. The polymer beads were distributed at a density of 0.85 [m/σ^3] in the CGMD space, where m is the CGMD unit of mass. By conducting reaction simulations after the merging of polymer melt and fillers, 60,000 cross-linking bonds were created. The interaction between polymer and filler particles was modeled using Lennard-Jones potential as follows:

$$U_{LJ}(r) = 4\varepsilon \left[\left(\frac{\upsilon}{r}\right)^{12} - \left(\frac{\upsilon}{r}\right)^{6} + \frac{1}{4} \right] \tag{2.4}$$

where r, ε, and υ denote the distance between polymer and filler, the strength of the interaction, and the diameter of the sphere beads, respectively. υ was set to 1.0 in this study. ε was set to 15.0 with cutoff distance $r_c = 2.5$. This values represents the attractive interaction which is the interaction between polymer and carbon black [DB93][Pie12]. The stress-strain responses up to a strain of 0.3 were simulated at a elongation velocity of 0.01 [σ/τ]. All simulations were carried out with a molecular dynamics simulation software, J-OCTA/VSOP [Cor] and LAMMPS [Pli97]. The stress-strain responses are shown in Figure 2.4.

Table 2.1: Parameter range for filler configurations.

	Minimum	Maximum
Radius of the aggregate [σ]	0.1	2.0
Poisson point process intensity for the aggregate	0.3	2.0
Volume fraction of the exclusion polymer	0.1	0.6
Poisson point process intensity for the exclusion polymer	0.1	1.0

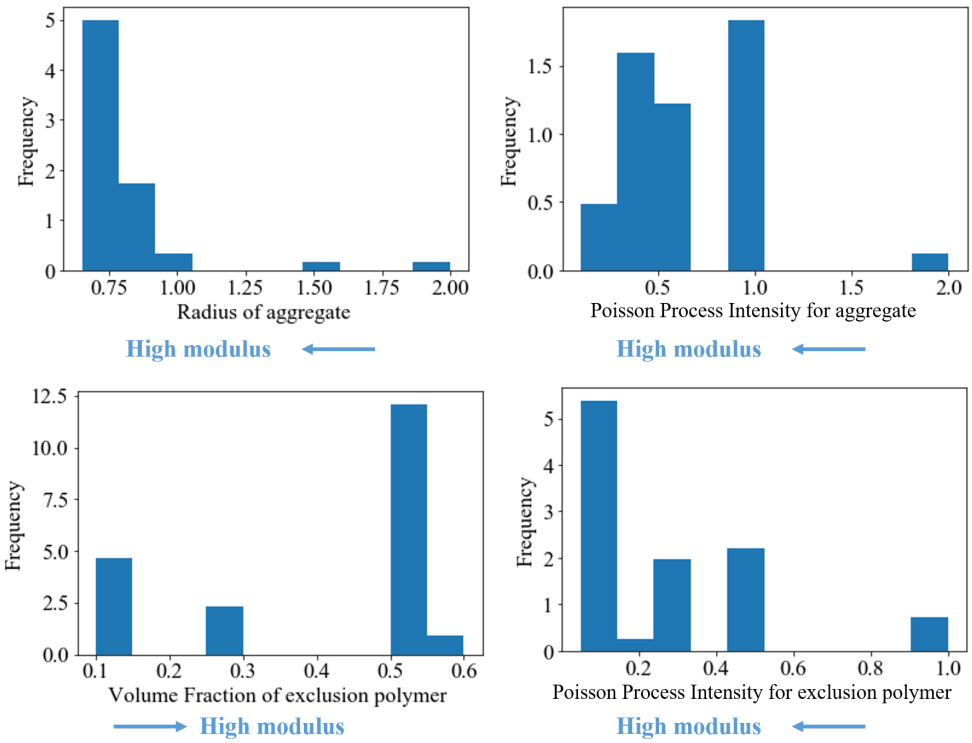


Figure 2.2: Distributions of four input parameters for filler morphology to generate the training data for the CNN-based surrogate model. Distributions of all parameters were designed to produce the high modulus.

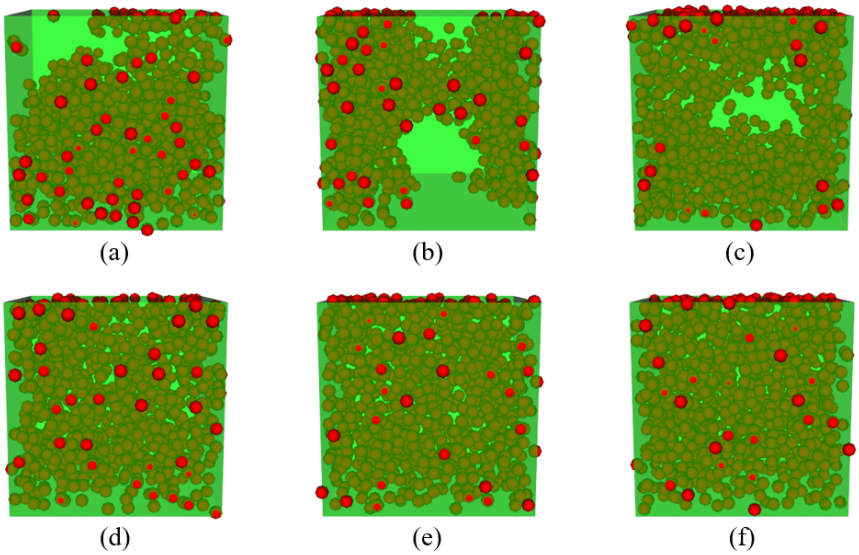


Figure 2.3: Example of visualized filler configuration. The green box is the entire region of the large-scale CGMD simulation. The red particles are the filler particles. The radius and expected values of the aggregate, the volume fraction, and the expected values of the exclusion polymer are (a) 0.7,0.3,0.3,0.1, (b) 0.7,0.6,0.5,0.1, (c) 0.8,0.6,0.5,0.1, (d) 1.0,1.0,0.1,1.0, (e) 1.5,1.0,0.1,1.0, and (f) 2.0,2.0,0.1,1.0, respectively.

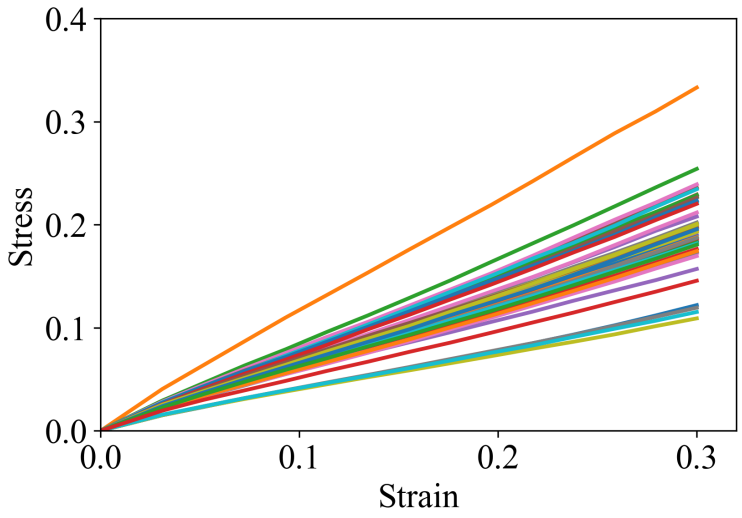


Figure 2.4: Stress-Strain curves measured by CGMD up to a strain of 0.3. Each line represents the Stress-Strain curve induced by the filler morphology.

2.3.3 Data augmentation procedure

The training data which composed of filler morphology image at strain of 0.0 and stress at a strain of 0.3 were generated from these CGMD results for the CNN-based surrogate model. The number of input graphical image could increase by creating the mirror image. However, the variation of the stresses induced by these created morphologies did not increase, because the mirror images generated per a morphology correspond to the same identical stress. To alleviate this problem, the filler morphology information in the local region, not the entire CGMD region, were converted to the training data, with the aim of data augmentation. Namely, we increased the number of instances in the training data by dividing the simulation results of an entire large-scale geometrical region into middle-scale regions, a portion of the large-scale region as explained later. Each training instance was then converted into a 3D image of the middle-scale filler morphology and stresses at a strain value 0.3 of the corresponding region. The binary image was created using the filler density distribution. The stress of each divided middle-scale region was calculated based on the CGMD simulation algorithm, defined as $Stress_Z - (Stress_X + Stress_Y)/2$, where the elongation direction is Z [YQ14][GLS+14]. Here, subscripts represents the components of the stress. The beads and bonds, in the middle-scale region, were extracted under the periodic condition. Then, the stress was calculated as the summation of the interaction force between two beads, the bond force, and the pressure arising from bead velocity as follows:

$$Stress = \frac{1}{V}\left(\sum_{i=0}^{N}\frac{P_i^2}{m_i} + \sum_{i=0}^{N-1}\sum_{j>i}^{N} r_{ij}f_{ij}\right), \tag{2.5}$$

where, V is the volume of the entire CGMD region, N is the number of beads, P_i and m_i are the momentum and mass of the beads i respectively. r_{ij} stands for a vector between bead i and bead j calculated by $r_i - r_j$, and f_{ij} is the force exerted on the bead i by the bead j.

Some reports have shown that the filler morphology in filled rubber has a hierarchical structure ranging from nanometer- to micrometer-scale [TNSM19][Dan75] [SBS03][Mih15] and the filler-filler interaction is partially responsible for the stress

[VHK09][IA96]. Therefore, the stress arises from not only the filler particles inside the considered region but also nearby filler particles outside the region. To consider filler particles both inside and outside the target region, the image that was used included the fringe, in addition to its own region, to reflect the influence of the filler particles outside the divided region. This was the size effect of the large-scale CGMD.

The concrete process of the data augmentation was as follows. We created two images from one filler morphology. One 3D image was stacked the XZ plane images along the Y direction. The other was stacked the YZ plane images along the X direction. The 3D images stacking the XY plane image along the Z direction—which was the deformation direction—were not generated, because the X and Y directions and the deformation direction Z were not symmetric in terms of the elongation. Furthermore, mirror images of X, Y, and Z directions were generated. Finally, 5 divided regions were extracted along the X, Y, and Z directions, namely, $125 = 5 \times 5 \times 5$ regions were extracted from the entire CGMD region. Through this data augmentation process, 2,000 images were created from one filler morphology. Thus, 90,000 (125 samples per a large-scale CGMD region $\times$ 8 mirror images $\times$ 2 types of images $\times$ 45 large-scale CGMD results) training instances of the divided regions were generated from the 45 large-scale CGMD results.

Figure 2.7 shows the distributions of the stresses of the entire region and those of the divided region for the data augmentation. The stress of the divided region was observed to be more widely distributed than that of the entire region, which means that the training data generated by the local region was composed of the various morphologies. The size of the divided region and the size of the fringe are discussed in Section 2.5.

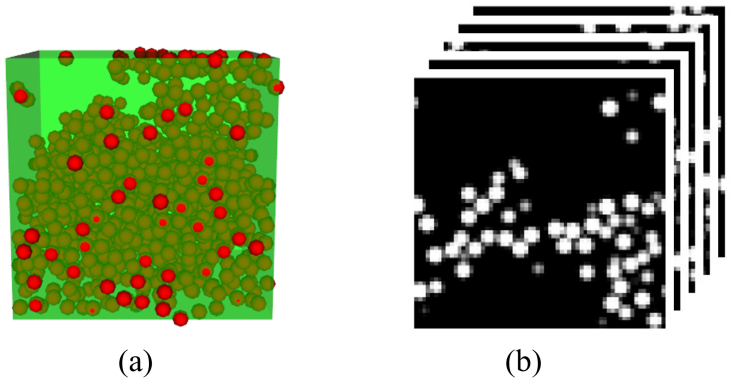


Figure 2.5: Example of a filler configuration and 3D image: (a) Visualized filler configuration and (b) 3D image.

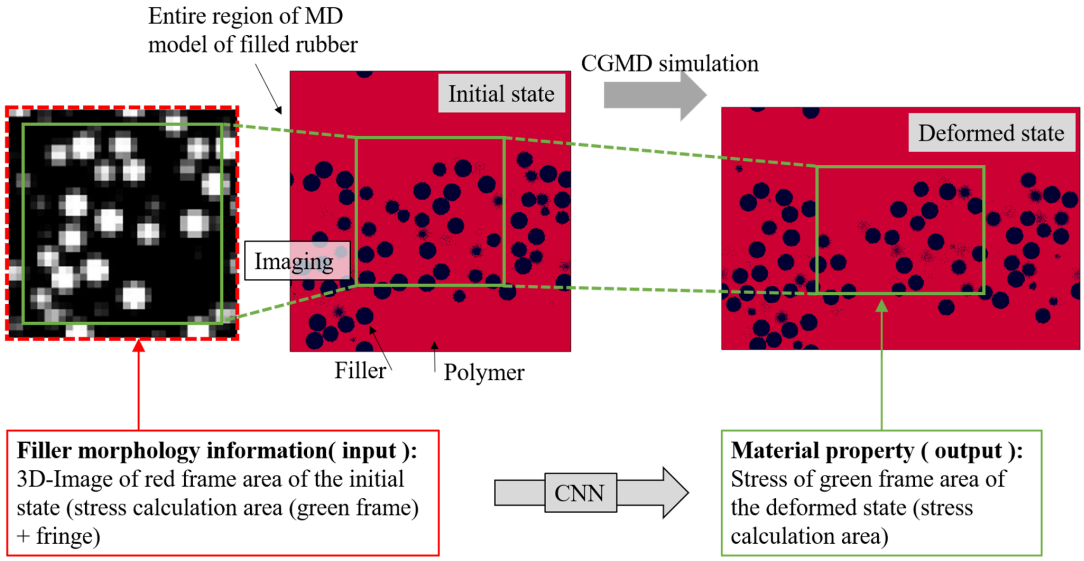


Figure 2.6: Schematic for training data instance composed of the imaged filler morphology information (input data) and the material property (output data). Imaged region of dotted red frame in bottom figure is slightly larger than the green region where material property is measured, because outside region of the green region influences on the property of the green region. The material property results from the large-scale CGMD simulation.

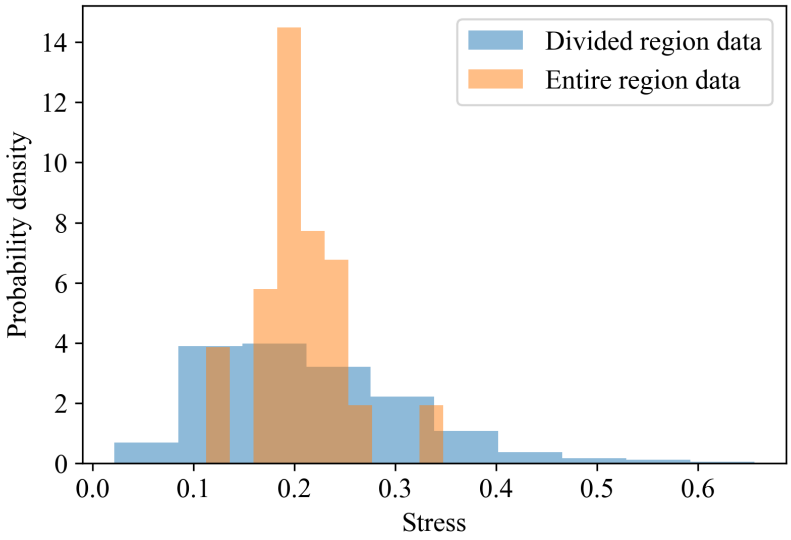


Figure 2.7: Distributions of stress in the training data. The blue bars and the orange bars represent the stresses in the divided region of the CGMD space and the entire CGMD region, respectively.

2.4 Configuration of CNN-based surrogate model

We used PyTorch [pyt] to construct a CNN with two 3D-convolutional layers and one fully connected layer. The number of features of both convolutional layers was 50. The kernel of size of 4×4×4 moved with a stride of 1 in both layers. The pooling size of the first convolutional layer was 2, and global average pooling [LCY14] was used to connect the second convolutional layer to the fully connected layer. A leaky rectified linear unit (leaky ReLU [MHN13]) was used as the activation function to avoid zeroing signals during training. Our network architecture is shown in Figure 2.8.

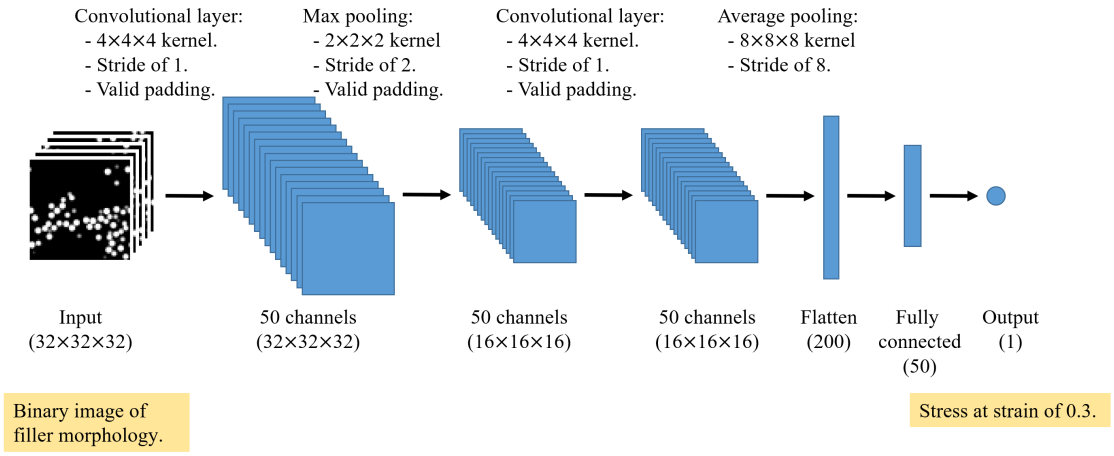


Figure 2.8: CNN architecture.

2.5 Training of the CNN-based surrogate model and its performance evaluation

2.5.1 Data sets for constructing the CNN-based surrogate model

The dataset described in Section 2.3 were partitioned into 10 data segments, which were grouped into three sets: training, validation, and test datasets. One data seg-

ment was used as the validation dataset, another was used as the test dataset, and the remaining eight segments were used for the training. The training dataset was used for the training of the CNN-based model, i.e., learning the parameters. Then, the optimal parameters of the CNN-based model were determined by estimating the accuracy of the model using the validation data. The test dataset not used for training and validation was used to measure the estimation performance.

2.5.2 Training of the CNN-based surrogate model

The CNN-based surrogate model was trained by minimizing a mean squared error between the value resulted by the CGMD simulation in training data and the value estimated by the model. The CNN-based surrogate model was trained for 60 epochs, and the generalization performance (prediction accuracy) was measured every 2 epochs using the validation data. After all, the CNN-based surrogate model provided the highest performance using the validation dataset, i.e., the surrogate model provided the smallest mean squared error between the estimated stresses and the CGMD-measured stresses as reference, was selected. Adam [KB15] was used as the optimization algorithm. During training, 25% of the elements of the tensors in the hidden layers in the CNN was zeroed via dropout [WG15]. The learning rate and batch size were 0.0025 and 50, respectively.

2.5.3 Influence of an input image size and its fringe size on accuracy

In order to determine the size of the fringe of an input image, where is the region converted to the input image along with the stress measured region, we investigated the relationship between the size of fringe and the prediction accuracy. The prediction accuracy was measured by the test dataset. The ratio of the cell lengths of the divided region—stress measured region—in X, Y, and Z directions was 1/2 of the entire CGMD space, hence the volume of the divided region was 1/8. The top five morphologies, ranked by their CGMD-measured stress magnitude, were used as the test dataset, in order to evaluate the extrapolation prediction accuracy of

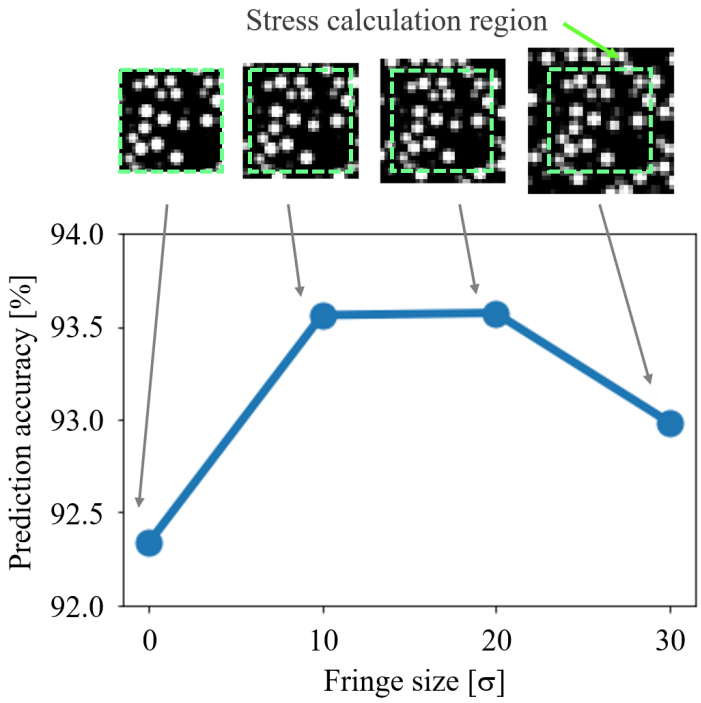


Figure 2.9: Relationship between fringe size and prediction accuracy. The prediction accuracy is a ratio of the predicted stress by the CNN-based surrogate model to the CGMD-measured stress.

the trained CNN-based model. The data of 40 morphologies, except for these five, were used as training or validation data. The most accurate surrogate model for the validation data in the course of 60 training epochs was used for performance analysis using the test data. The averages of the extrapolation prediction accuracies induced by the fringe sizes of 0, 10, 20, and 30 [σ] were compared. Note that, the size of the divided region was 150 [σ], because the entire CGMD region was 300 [σ], and the number of pixels of the input image along each direction was 32. The stresses of the entire regions, calculated as the average over the estimated stresses of the divided regions included in the corresponding entire region, were compared with the correct answer (i.e., the result of CGMD). Figure 2.9 elucidates the prediction accuracy of the fringe sizes of 10 or 20 [σ] was similarly high. Therefore, 10 [σ] was selected as the fringe size because of its smaller cost for image creation.

Next, we explain the relationship between the size of the divided region and

the corresponding accuracy. The accuracies of the divided region sizes of 120, 150, 180, and 240 [σ] (i.e., 40, 50, 60, and 80% of the entire region, respectively) were compared. Note that the size of the fringe was 10 [σ] based on the result of a previous paragraph. Figure 2.10 shows that 150 [σ] indicated the highest accuracy. We deduced that the variety of the stress of the broader divided region was smaller than that of the narrower divided region because the stress of the broader divided region was close to that of the entire region. As a result, the distribution of the training data of the divided region was narrower and similar to that of the entire region's training dataset. Thus, the accuracy decreased. On the other hand, when the divided region was smaller, the stress distribution is wider. However, the accuracy still declined, owing to other effects from increasing factors that were not represented in the binary images (e.g., crosslinking of polymer). Thus, we set the stress calculation region in the divided region to 150 [σ]$\times$150 [σ]$\times$150 [σ], and the imaging region to 170 [σ] $\times$ 170 [σ] $\times$ 170 [σ] by adding a fringe of size of 10 [σ] to both sides of the stress calculation region. In this study, we determined the effect of the fringe size first, then the effect of the divided region size for efficiency.

We established the surrogate model for the divided region through the aforementioned process. As explained in the Section 2.3, the input data and the output data were the binarized 3D image of filler morphology and its stress at a strain of 0.3, respectively. The input data was an information of the filler morphology in 170 [σ]$\times$ 170 [σ]$\times$ 170 [σ], which includes the surrounding of 10 [σ]. Namely, the surrogate model can predict the stress of the target space of 150 [σ]$\times$ 150 [σ]$\times$ 150 [σ] from the surrounding of 170 [σ]$\times$ 170 [σ]$\times$ 170 [σ].

2.5.4 Extrapolation accuracy of CNN-based surrogate model using the test data

We calculated the stresses of the all 45 filler morphologies by changing the test data, and compared with the CGMD measured stress—correct values—for the purpose of the evaluation of the extrapolation performance of the CNN-based surrogate model. The stresses calculated by using the test dataset were presented in Figure 2.11. The estimated stresses by the CNN-based surrogate model were presented with a green

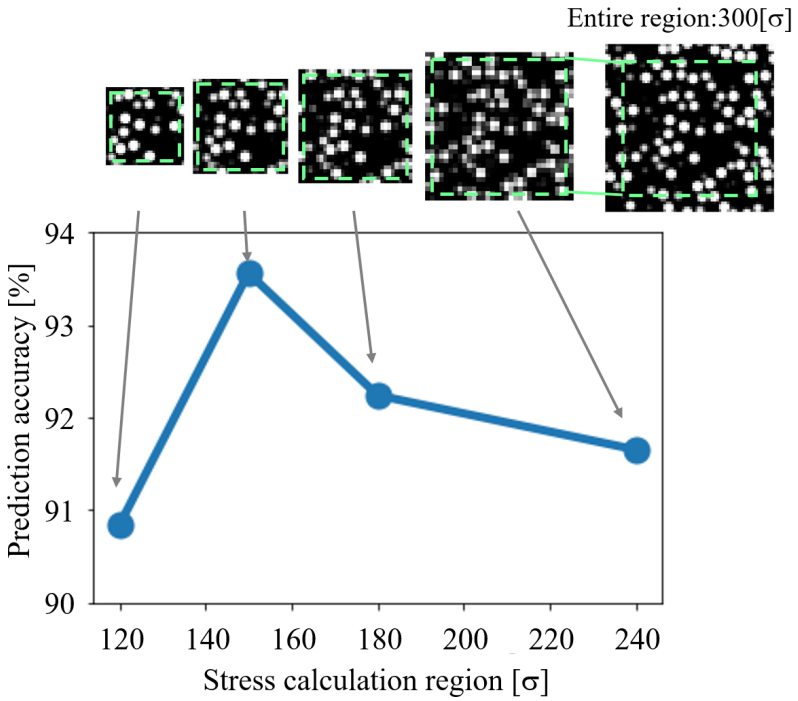


Figure 2.10: Relationship between the middle-scale region and the prediction accuracy. The prediction accuracy is the ratio of the predicted stress by the CNN-based surrogate model to the CGMD-measured stress. Here, the fringe size was 10 [σ].

line in this figure. The stresses provided by the CGMDs were drawn by a blue line. This figure indicates the stress in the entire CGMD region 300 [σ]$\times$ 300 [σ]$\times$ 300 [σ]. The stress in the entire region can be calculated by averaging the CNN measured stress of the divided region as described in previous subsection 2.5.3. To show the high extrapolation accuracy of the CNN-based surrogate model trained by the divided region, we presents stress values estimated by the CNN trained by morphology images in the entire region of the CGMD simulations. They are indicated by an orange line in Figure 2.11. The X axis represents the filler morphologies sorted by the stress provided by the CGMDs at a strain of 0.3. We confirmed that the prediction accuracies of these two CNNs were high in the moderate stress level such as 0.2. However, the estimation accuracies of the CNN trained by the images

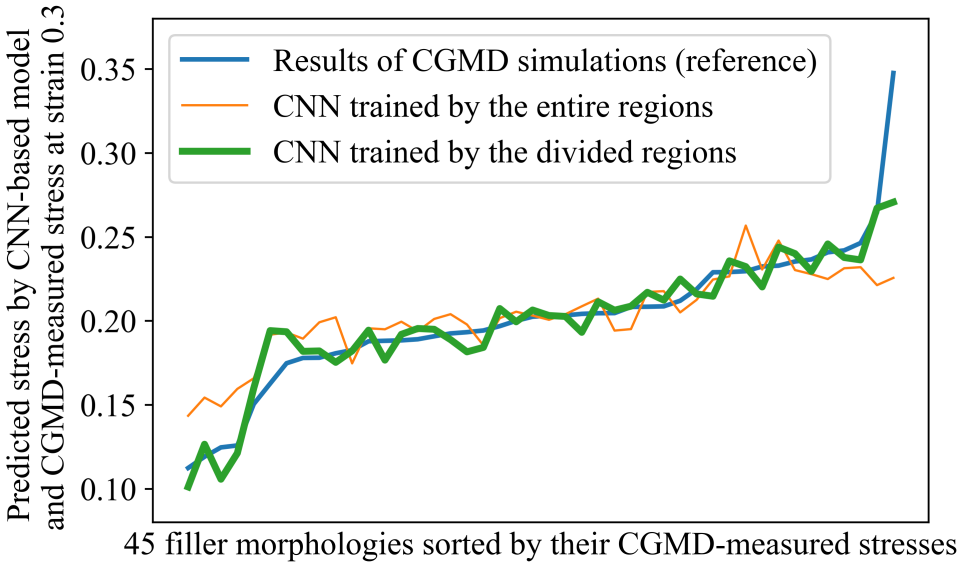


Figure 2.11: Comparison of the prediction stresses by the CNN-based surrogate model trained by the divided regions and the references. The results of the proposed method were compared with the stresses predicted by the CNN-based surrogate model trained by the entire regions of the CGMD simulation.

of the entire region were lower in the ranges of the extremely large or small stress values. We speculate that the extrapolation accuracy of the CNN using the entire region of the CGMD simulation decline because the training data do not include the extremely large stress. In contrast, the estimation accuracy is high in case of the model trained with the data of the divided region. This improvement resulted from the wider distribution of the stress of the divided regions used for training as shown in Figure 2.7. Thus, the training by using the morphologies in the divided regions strengthens the extrapolation ability of the surrogate model.

2.6 Conclusion

We introduced a surrogate model of a large-scale CGMD with the aim of rapid and accurate estimation of the mechanical properties of polymerized and nanoscale filled rubber. The surrogate model was established using the CNN, the input and output data of the surrogate model were 3D binary images of the filler configuration, and the stress at a strain of 0.3. We augmented the training data by dividing the simulation results on an entire large-scale geometrical region into those of middle-scale regions. This technique provided the training dataset including various filler morphologies and wide distributed stresses. In addition to the divided region, the surrounding regions were converted to the input image, in order to maintain the size effect of the large-scale CGMD simulation and high prediction accuracy. 90,000 training instances of the middle-scale regions were generated from the 45 large-scale CGMD results. The resultant surrogate model trained by using the images of the middle-scale regions provided higher extrapolation accuracy for material elongation than that provided by the surrogate model trained using images of the entire large-scale region. Thus, the response of a large-scale region is easily predicted by integrating the responses of the middle scales regions. Note that the established CNN-based surrogate model took approximately 10 seconds, including imaging of the divided region, to measure the stress of the entire CGMD region, while the CGMD simulation required a month to calculate the stress.

Chapter 3

Search Strategy for Rare Microstructure to Optimize Material Properties

3.1 Introduction

As described in Chapter 1, exploration and analyzing the microstructures providing the desired property are needed to reveal the microstructure-property linkage. The exploration of the microstructures means creating new microstructures candidates, measuring a material property, and selecting microstructures providing the desired property. The two major barriers to microstructures exploration are the huge computational cost for measuring the material property and the lack of effective exploration techniques. To overcome the former, we established a highly accurate surrogate model for the large-scale CGMD of filled rubber in Chapter 2. In this Chapter, we propose an efficient exploration method for the complex filler morphologies inducing given properties.

Two types of methods have been suggested for generating possible filler morphologies: probabilistic methods such as generating filler positions based on the Poisson point process [FJF$^+$16], and deterministic methods that directly determine each filler position [HTH$^+$18][HAK$^+$07][HTH$^+$08][Tak13]. In the probabilistic methods, the stochastic parameters such as Poisson process intensity characterizing the filler morphology that induces the desired material properties are not easily searched, because material properties largely vary depending on the randomly sampled filler morphologies even under the same parameters [MF17]. In the determin-

istic methods, the filler morphologies are fixed by the input parameters, which are the coordinates of each filler particle in a three-dimensional space. Nevertheless, the number of target parameters increases dramatically with the number of filler particles (n) as $O(n)$, which prevents sufficient morphology exploration.

We propose a novel morphology search method which is hybrid of the probabilistic and deterministic methods. It is the combination of CNN based surrogate model for the large-scale CGMD, a Markov chain Monte Carlo (MCMC) technique [Has70], a gradient descent method, and CGMD simulation. To the best of our knowledge, exploration techniques with MCMC have not been applied to the filler morphology search, although it was used for manufacturing [KWKF18]. When the filler morphology is sampled iteratively, it is desirable to use coordinates of filler particles as the search parameters, because the varieties of morphologies can be included in the exploration space. However, parameter search that scales as $O(n)$ is hardly feasible for large number of the filler particles, n, because of huge computational cost and curse of dimensionality [LBBH98][KWPD$^+$20]. To overcome this problem, we specifically propose an efficient and effective technique to intensively sample filler morphology that induces desired material properties. This search is conducted by replica exchange MCMC [ED05] and surrogate model-based simulation in a discrete representation space of the filler morphology. Once candidate filler morphologies predicted to provide good material properties are searched, they are updated by the gradient ascent method using the surrogate model-based simulation in order to further find filler morphologies that is expected to provide better desired properties. Finally, CGMD simulations are carried out to validate whether the searched filler morphologies actually provide the desired properties, because the properties evaluated during the search using the replica exchange MCMC and the gradient ascent method are merely the predicted values by the CNN-based surrogate model for efficient search.

The remainder of this chapter is organized as follows. In the Section 3.2, a new methodology to investigate the relationship between a material property and a change of the microstructure during the deformation is proposed. The exploration objective is explained in the Section 3.3. The developed exploration method is explained in the Section 3.4. The exploration performance and the exploration

results are explained in Section 3.5 and Section 3.6, respectively. The last Section 3.7 presents the conclusion.

Note that the proposed exploration method is not limited to the exploration of the filler morphologies. For instance, a microphase-separated structure if polymer alloy and an ionic solid can be applied. Whereas, a crystal structure of a metal may not be suitable for the proposed method, because the microstructure of the material does not vary. In addition, any simulator can be used to measure the material property and its dependence on the microstructure, insted of using the CNN-based surrogate model established in Chapter 2, if the simulation speed is sufficiently high.

3.2 Preliminary studies

In this section, a method for analyzing the CGMD simulation result is proposed, and the mechanism to cause the difference of the material properties between two filler morhpologies is presented. It is expected that the efficiency to search the morphologies having large stress is improved by using the features of the filler morphology increasing the stress as a prior knowledge. Two filler morphologies presented in Figure 3.1 were created: an aggregated model shown in Figure 3.1 (a) and an uniformity arranged model shown in Figure 3.1 (b) which is an ideal dispersed morphology. The filler locations of the aggregated model was determined by the multi-step Poisson point processes, same as in Section 2.3. Both morphologies consisted of 1,000 filler particles with the radius of $10[\sigma]$ and 1,000 polymer chains of length of 20,000 beads. The polymer phases included 60,000 cross-linking bonds. Not only these physical information such as the radius of fillers, but also the simulation conditions of CGMD, e.g., the interaction between filler and polymer, and elongation velocity, were identical with those in the Section 2.3. The stress-strain responses up to a strain of 0.3 were simulated using a molecular dynamics simulation software, J-OCTA/VSOP [Cor] and LAMMPS [Pli97]. Figure 3.2 shows the simulated stress-strain relations. It is clear that the impact of filler morphology on the property, namely the structure increases the stress, is reproduced qualitatively.

Stresses of the system were decomposed into “bond stress” and “nonbond stres”

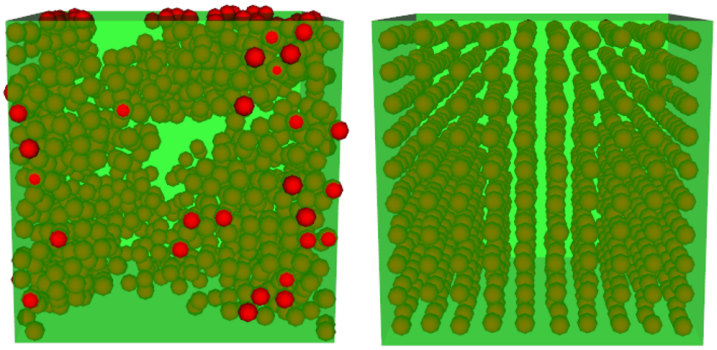


Figure 3.1: Filler positions for large-scale CGMD: (a) aggregated model, (b) uniformity arranged model. Red dots and green domain represent filler particles and polymer phase, respectively.

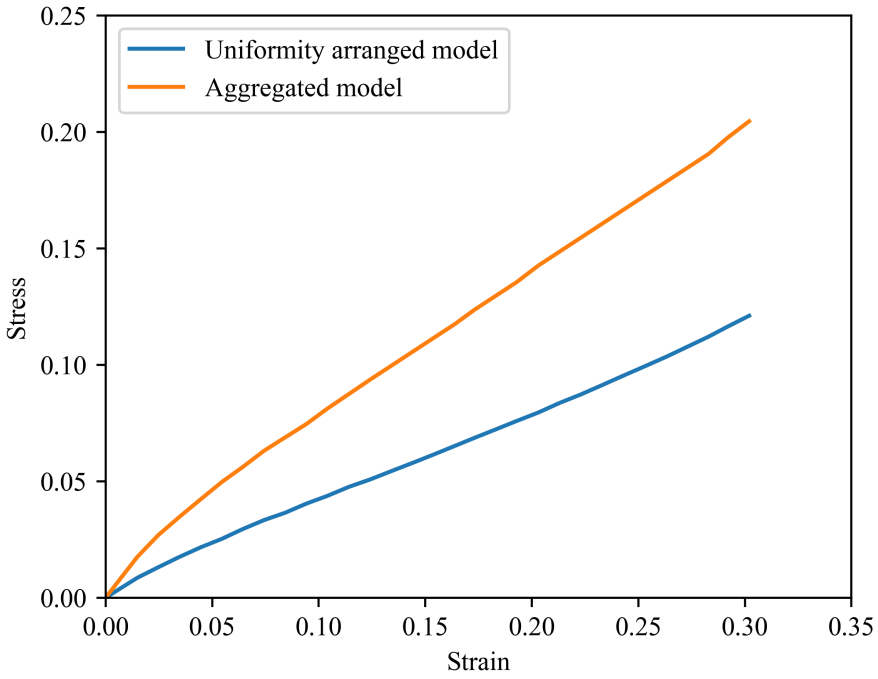


Figure 3.2: Simulated stress-strain curves of the uniformity arranged model and the aggregated model.

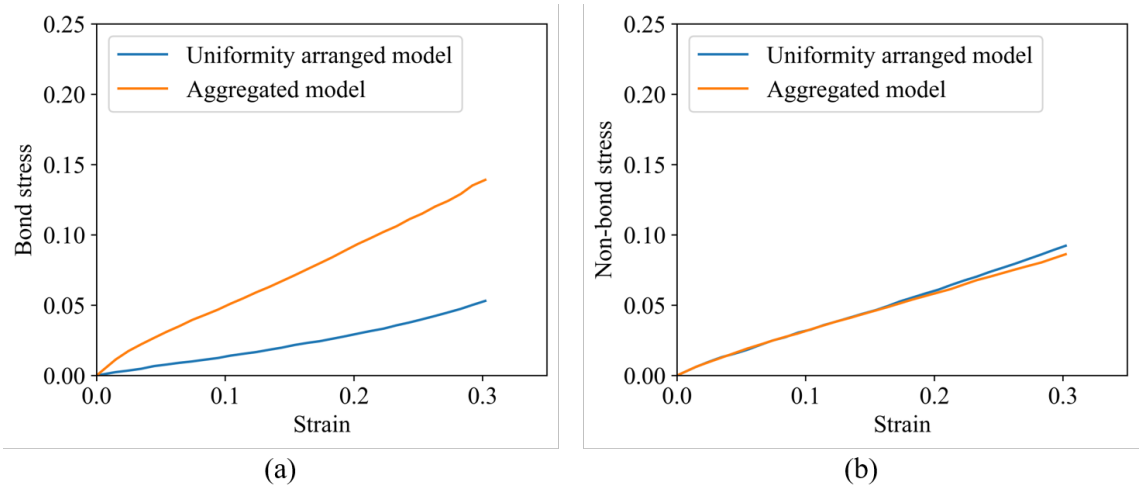


Figure 3.3: Decomposed stress-strain curves of the uniformity arranged model and the aggregated model: (a) bond stress and (b) nonbond stress.

in order to clarify the origin of the difference in the stress-strain responses impacted by filler morphology as shown in Figure 3.3. The bond stress arises from the bond force/stretch, and represents the energy elasticity. The nonbond stress arises from the interaction energy between beads and the kinetic energy, and represents the entropy elasticity. Figure 3.3 shows the bond stress mainly induces the difference in the stress of the system. The bond stresses of both models were decomposed into the bond stress in the polymer phase and the bond stress in the filler phase to investigate the origin in detail as shown in Figure 3.4. Consequently, we confirmed the difference in filler phase induces the difference in the responses of the systems, because there are clear differences in the bond stress in the filler phase.

The number of filler aggregates was measured in order to investigate a reason of the difference in the filler bond stress. A set of the filler particles, between which the distance was less than 1.0 $[\sigma]$, were considered as a filler aggregate. Figure 3.5 indicates there is no aggregate in the uniformity arranged model during the deformation, because the number of the aggregate is equal to 1000; the total number of filler particles. Meanwhile, the number of the filler aggregates of the aggregated model increases, namely, the filler aggregates breaks during the deformation. It is inferred that the breakage of the filler aggregate increases the stress of the filler

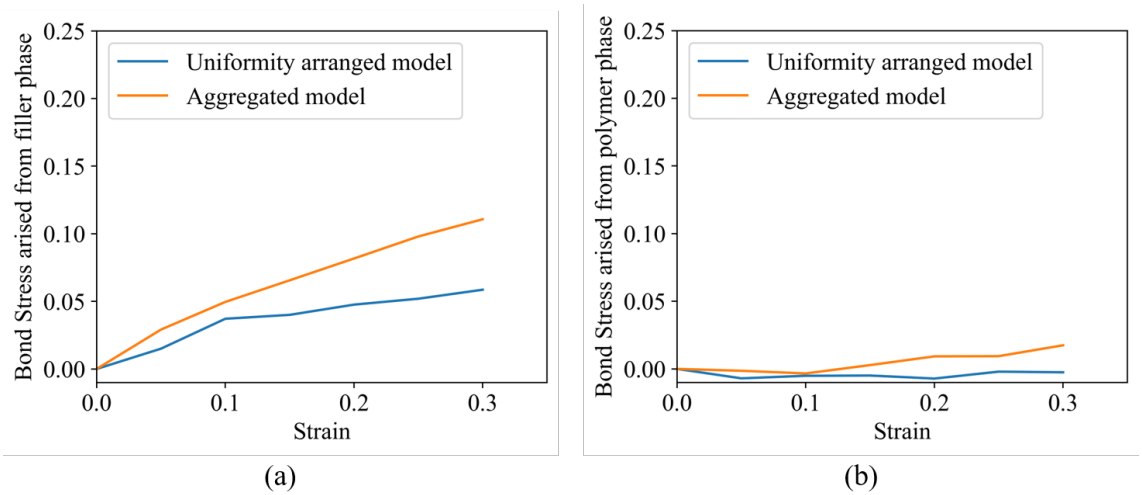


Figure 3.4: Decomposed bond stress-strain curves of the uniformity arranged model and the aggregated model: (a) filler phase and (b) polymer phase.

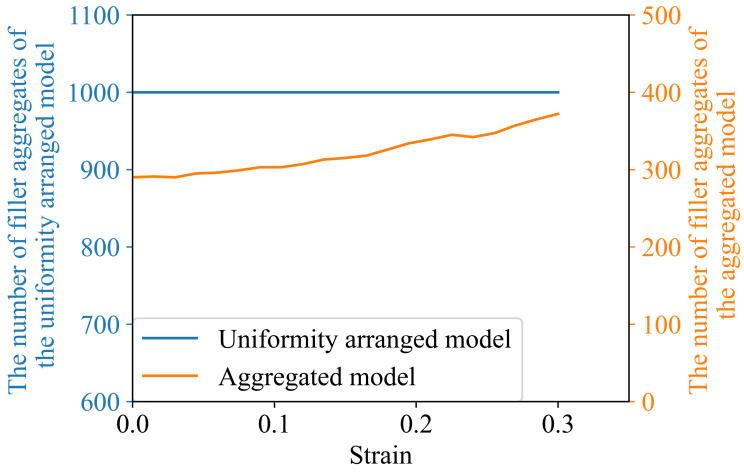


Figure 3.5: The change in the number of aggregates during the deformation.

phase due to the contact between filler particles induced by the breakage. This result suggests that a development of the sampling method to search some special filler locations is needed to find the morphologies providing the extremely high stress, because the filler positions boosting the contact of filler particles are the key to control the stress.

3.3 Problem setting for filled rubber microstructure

We investigated the relationship between filler morphology and stress at strain of 0.3 using a random sampling technique and CGMD simulation in order to obtain filler morphologies having high elastic modulus that improve tire abrasion resistance. The space size was $150[\sigma] \times 150[\sigma] \times 150[\sigma]$ (σ: unit length used in the CGMD), and radius of filler particles is $10[\sigma]$ in all morphologies. Stresses were calculated using the molecular dynamics simulation software LAMMPS [Pli97] and VSOP/J-OCTAP [Cor]. The number of random samples were 5,000 where various filler morphologies were generated. Figure 3.6 shows the result of this investigation. The increase of the elastic modulus along with the aggregation of more filler particles is observed, which is consistent with our existing knowledge [Klü03][VHK09]. The result included only one morphology exceeding stress 0.65. Even for the lower stress 0.6, only six morphologies exceeded this number. The filler morphologies having stress more than 0.65 are rarely found by the random sampling. However, this does not imply nonexistence of any filler morphologies having higher stress. There may be some other filler morphologies providing high stress.

Our exploration objective was to obtain filler morphologies that induce stress of 0.6 or higher. It is well known that the stress of filled rubber is roughly proportional to volume fraction of filler [E. 45][DTT+19], and filler particles percolate beyond approximately from 22 vol.% to 25 vol.% [LLJ+22]. Moreover, mechanical properties change once filler particles percolate [CZC+14][KMAS96]. Based on these studies, the volume fraction of filler was restricted to 20 vol.% represented by 250 filler particles during the exploration, in this study, in order to understand the mechanisms to generate the stress in a phase not having filler percolation. The space size and the radius of filler particle were $150[\sigma] \times 150[\sigma] \times 150[\sigma]$ and $10[\sigma]$, respectively, same as the random sampling and the divided region converted to the training data in Section 2.3. The CNN-based surrogate model developed in the Chapter 2 is used to measure the properties during the sampling for the efficient search.

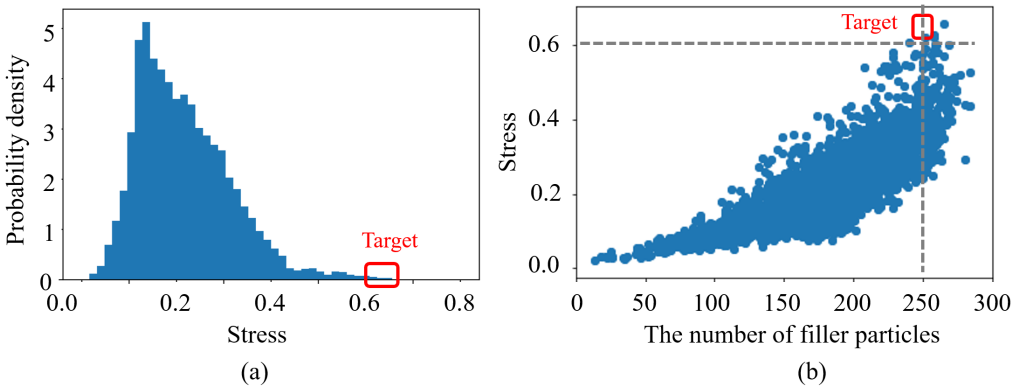


Figure 3.6: Result of the random sampling: (a) is the distribution of stress at strain of 0.3. (b) is a plot of the number of filler particles and stress. The stress is roughly proportional to the number of filler particles. Approximately 250 fillers are needed to reach the stress of 0.6, which is the sampling objective.

3.4 Exploration method for rare filler morphology

In Section 3.2, the importance of the development of the exploration method to search some special filler locations was explained. In this section, a novel exploration method for the filler location is proposed. The proposed method consists of three steps. In the first step, desired filler morphologies are explored widely in a discrete representation space of the filler morphology. In the second step, the filler morphologies are searched locally to find morphologies providing much better property. In the last step, the physical computer simulation is performed in order to validate whether the searched filler morphologies actually provide the desired properties, because the properties evaluated during the first 2 steps are merely the predicted values by the high-speed surrogate model of the physical computer simulation.

The multicanonical MCMC [ISK14] and the replica exchange MCMC [ED05] are sampling techniques for rare events. The multicanonical MCMC uses a single

MCMC technique that sequentially draws samples from an implicitly given probability distribution in a possibly high-dimensional space. Weights for the samples are iteratively updated to ensure their uniform distribution with respect to the feature of interest. Accordingly, it could efficiently produce samples meeting specific conditions including rare target conditions of the feature, with their weights precisely preserving their probabilities.

The replica exchange MCMC employs layered MCMCs in parallel. The MCMC sequence in the top layer follows the probability distribution of interest by maintaining its detailed balance of the sequence. The deeper layers follow more flattened distributions in the same manner, respectively. Samples in the pairwise layers are exchanged under a detailed balance in order to widely search for rare events. In this study, the replica exchange MCMC capable of simultaneous parallel searches was employed for sampling filler morphology, because our purpose was to obtain as many high stress morphologies as possible.

3.4.1 Replica exchange MCMC for filler morphology search

The replica exchange MCMC draws samples from T probability distributions in parallel, where each distribution has inverse temperature parameters α_t ($t = 1, \cdots, T$) and T is total number of temperatures. The search area of each MCMC sequence in the sample spaces depend on the inverse temperature α_t when the probability distribution follows the Boltzmann distribution. A low temperature is used in the top layer to locally search for rare conditions of interest, while the deeper layers with higher temperatures search wider areas in the sample space because their distribution is wider than the top layer. Occasional exchange of the samples between the MCMC sequences having different temperatures enables to search for local solutions in the wide sample space.

In this study, the probability distribution $P\left(S^t\right)$ of the filler morphology S at temperature t is designed using the Boltzmann distribution as follows:

$$E\left(S^t\right) = \frac{1}{\lambda f\left(S^t\right)}, \tag{3.1}$$

$$P\left(S^t\right) = exp\left(-\frac{E\left(S^t\right)}{\alpha_t}\right), \tag{3.2}$$

where, $f(\cdot)$ is the function that calculates the stress at strain of 0.3 from filler morphology S^t. The surrogate model for the CGMD of filled rubber based on our method proposed in Chapter 2 was used to calculate $f(S^t)$. The energy $E(S^t)$, which is inversely proportional to the stress, is designed to have higher probability of generating morphologies that provide greater stresses. Each MCMC sequence searches the filler morphology space iteratively, following the different probability distributions that depend on the temperature via the coefficient α_t. λ is a hyper parameter to tune the dependency of the probability distributions on the stresses.

In the high-temperature sequence, filler morphologies are iteratively searched according to a flattened state distribution, so that a wide filler morphology space is searched without being trapped in local solutions. In contrast, the low-temperature sequence focuses on the local search for rare filler morphologies by following the probability distribution near the target stress f_{th}. That is, it iteratively searches for rare filler morphology without significantly changing the filler morphology characteristics. In addition, the change in filler morphology at high temperatures is reflected in the sequence at low temperature via the exchange between their sequences. Thus, the replica exchange MCMC can be used to obtain many local solutions, including rare filler morphologies that provide high stresses, from the wide filler morphology space. This suggests that we efficiently obtain the local solutions searched in all temperature sequences by analyzing the sequence history of the low temperature $t = 1$. In this study, the filler morphologies providing the maximum stress in the continuous MCMC sequence steps at $t = 1$ were extracted as the candidate tentative filler morphologies. These tentative filler morphologies will be used as initial filler morphologies to further improve their stresses by gradient descent search as described in the next subsection 3.4.2.

Each MCMC sequence of the replica exchange MCMC tracks the transition of filler morphology S_n^t following the target distribution $P(S_n^t)$ where S_n^t is filler morphology at a MCMC step n. Then, the MCMC update of the filler morphology at every step n is conducted by the following metropolis procedure. Let $Q(S^t|S_n^t)$ and $Q(S_n^t|S^t)$ be the transition probabilities from the filler morphology S_n^t to S^t and from S^t to S_n. S^t is a candidate filler morphology of step n+1 at temperature

t. The acceptance of S^t is determined as follows:

$$S_{n+1}^t = \begin{cases} S_t & if \ \frac{P(S^t)Q(S_n^t|S^t)}{P(S_n^t)Q(S^t|\ S_n^t)} > r, \\ S_n^t & otherwise \end{cases} \tag{3.3}$$

where $r \sim P_U([0,1])$ is sampled from a uniform distribution.

The exchange of S_n^t and S_n^{t+1}, that is, the exchange of filler morphologies between the adjacent temperatures t and $t+1$ sequences, was attempted at every m steps of n, *i.e.*, n *s.t.*, $n \ mod \ m = 0 \ for \ all \ n \in N$, under the detailed balance, where N represents the number of total sequence steps. m is sufficiently larger than the relaxation periods of the sequences. Here,

$$\text{randomly choose } t \quad \in \quad T-1, \tag{3.4}$$

$$\text{Swap}\left(S_n^t, S_n^{t+1}\right) \quad if \quad \frac{P\left(S_n^{t+1}|\ t\right)P\left(S_n^t|\ t+1\right)}{P\left(S_n^t|\ t\right)P\left(S_n^{t+1}|\ t+1\right)} > r, \tag{3.5}$$

where $P\left(S_n^t|t\right)$ is the probability of the filler morphology S_n^t at temperature t.

As mentioned in subsection 3.1, our purpose is to sample the filler morphology represented by the coordinates of the filler particle centers. Thus, the sampled parameter space for 250 particles has $250 \times 3 = 750$ dimensions (the X, Y, and Z coordinates of 250 particles). The search of 750 dimension is hardly performed, because of so called the curse of dimensionality. To overcome this issue, we reduce the search space by introducing a spin function that indicates the existence/nonexistence of a filler in a morphology, and then searched for filler morphology in the reduced search space. Specifically, filler candidate points were distributed in the space, and the state of each point was controlled by the spin function. Given $X \subset R^3$ be the set of predefined filler candidate positions, the state of each filler candidate point $x \in X$: s(x) is defined as follows:

$$s\left(x\right) = \begin{cases} 1 & \text{if } x \text{ is occupied by a filler particle,} \\ -1 & \text{otherwise} \end{cases} \tag{3.6}$$

The filler morphology S_n^t is represented by $S_n^t = \{s\left(x\right)|x \in X\} \in \{1,-1\}^{|X|}$ *s.t.* $|\{x \in X|s\left(x\right) = 1\}| = N_{filler}$, where N_{filler} is the number of filler particles in X. $\{x \in X|s\left(x\right) = 1, s\left(x\right) \in S_n^t\}$ is a set of points x that filler particles exist in a candidate filler morphology S_n^t.

The candidate filler morphology S^t in formula (3.3) is generated following the procedure described below. First, randomly selected point with $s\left(x\right)=1$ in S_n^t is flipped into $s\left(x\right)=-1$ which represents the polymer. Then, a point y in the polymer state, i.e., $s\left(y\right)=-1$, is randomly selected from the neighbor of $x; X_n^-(x|S_n^t)$ where the distance between x and y is less than or equal to d. $X_n^-(x|S_n^t)$ is formally represented as follows:

$$X_n^-\left(x|S_n^t\right)=\left\{y\in X|\|y-x\|<d, s(y)=-1, s(y)\in S_n^t\right\}. \tag{3.7}$$

Subsequently, the selected polymer state $s(y)=-1$ is flipped into the filler state $s(y)=1$. The transition probability $Q\left(S^t|S_n^t\right)$ from the current filler configuration S_n^t to the new configuration $S^t=\{s\left(x\right)=-1,\ s\left(y\right)=1,\ s\left(z\right)\in S_n^t$ is unchanged for all $z\neq x,y\ \}$ is defined as follows:

$$Q\left(S^t\middle|\ S_n^t\right)=\frac{1}{|X_n^-\left(x|S_n^t\right)|}, \tag{3.8}$$

by introducing a uniform probability to move a filler particle from its current position x to one of its neighboring polymer's positions y.

3.4.2 Filler morphology search using the gradient ascent method

The second step employs the gradient ascent method to search for the desired filler morphologies, starting from a tentative filler morphology S explored by the aforementioned replica exchange MCMC procedure. Every S is the candidate tentative morphology providing the maximum stress in a certain interval of the MCMC sequence at $t=1$. The interval is the period between the successive replica exchanges of the MCMC sequences at $t=1$ and $t=2$. The details are shown in Figure 3.7.

Given a parameter vector $X(S)$ which is the concatenations of 3-dimensional continuous position vectors x_i of all filler particles $i=1,\ldots,N_{filler}$ in a filler morphology S, $X\left(S\right)$ is iteratively updated during the gradient ascent search to enhance the stress at the strain 0.3. This search enables us to sample the filler morphologies with more desired property than the candidates resulted by the replica exchange MCMC. The mini-batch gradient ascent method [PLW19][RM51] is employed to

update $X(S)$ of every candidate filler morphology S:

$$X(S) \leftarrow X(S) + \eta g, \tag{3.9}$$

$$g = \frac{1}{|B|} \sum_{i \in B} \frac{\partial f(S)}{\partial x_i}, \tag{3.10}$$

where B, η, and g are the mini-batches of fillers, the learning rate, and the gradient, respectively. Note that $f(S)$ is the estimated stress at strain of 0.3 by the CNN-based surrogate model established in Chapter 2, and its gradient $\partial f(S)/\partial x_i$ of a filler particle x_i is measured as follows:

$$\frac{\partial f(S)}{\partial x_i} = \frac{f(x_i + \delta | X(S)) - f(x_i - \delta | X(S))}{2\delta}, \tag{3.11}$$

where δ is the virtual displacement of the filler particle and $f(x_i + \delta | X(S))$ is f where all $x \in X(S)$ except x_i is fixed. The update of the filler position is repeated until $f(X(S))$ exceeded the threshold, $f_{th} < f(X(S))$ or fall into the local solution, that is, $f(X(S))$ converges. Figure 3.8 is a schematic drawing of the proposed method that combines the replica exchange MCMC and the gradient descent method for the filler morphology search.

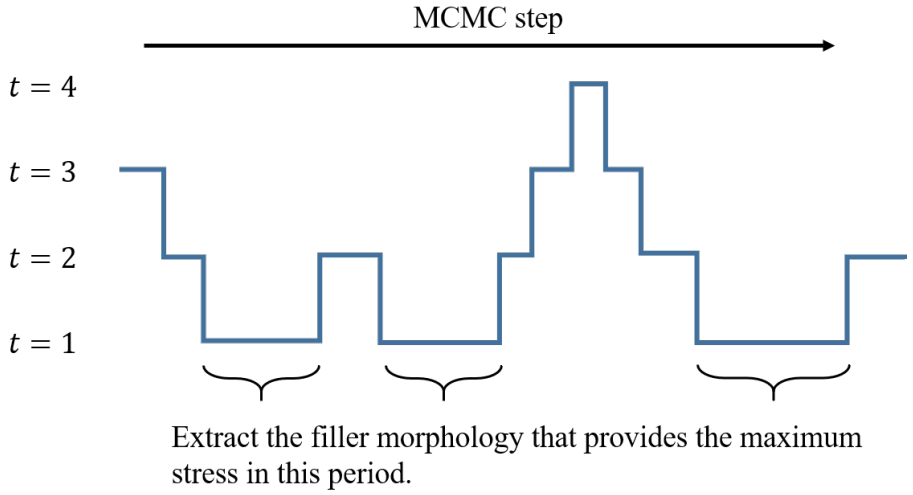


Figure 3.7: Schematic for extracting filler morphologies used as an initial state in the gradient ascent method from a history of replica exchange MCMC. Three morphologies were extracted in this example history.

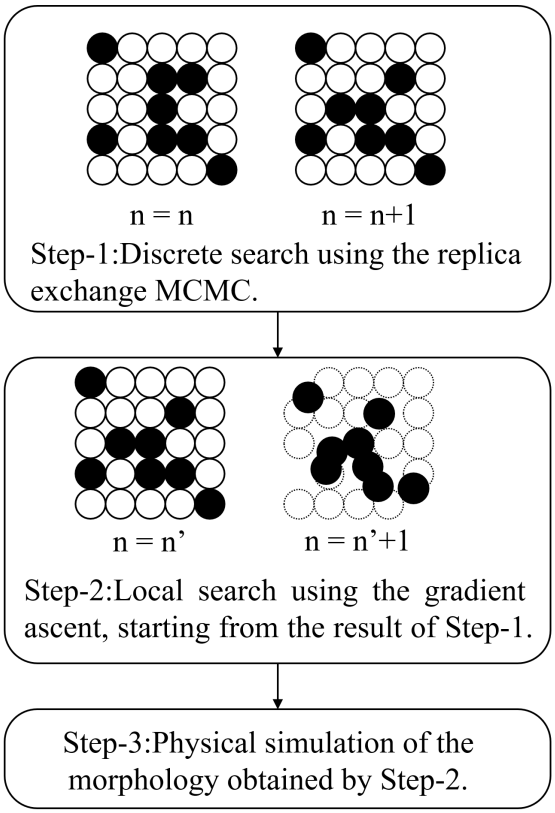


Figure 3.8: Schematic drawing of the proposed method. Circles in the Step-1 represent the filler candidate positions. The filler morphologies are defined by a set of the candidate points in order to discretize the filler morphology space. The discretization of the morphology allows the morphology exploration in the wide range. Open circles and filled circles are polymer and filler, respectively. The left figure in the Step-2 is the initial state of this step, which is obtained by Step-1. In this step, the local filler morphology space is searched by the update of the filler positions as a continuous value. The right figure shows an updated filler configuration.

3.4.3 Validation simulation of the mechanical property using computer simulation

During the search using the replica exchange MCMC and the gradient ascent method, the stresses predicted by the CNN-based surrogate model were evalu-

ated for the effective search. Thus, high stress values of the filler morphologies resulted by the search is not physically ensured. Accordingly, the validation of the high stress values of these filler morphologies is performed by using a physical model based computer simulations in the last step. In this dissertation, CGMD which was used to generate the training data of the CNN-based surrogate model described in Chapter 2 is employed.

3.5 Exploration performance

Exploration performance of the proposed method was compared with those of random sampling method, combined method of random sampling and gradient method, and method using replica exchange MCMC only. The random sampling provides the baseline performance. The combined method of random sampling and gradient ascent shows the effect of the gradient ascent, and the last method shows the effect of the replica exchange MCMC. As described in the Section 3.3, every exploration trial employed 250 filler particles, and the goal was to find the filler morphologies providing the stress over 0.65 in terms of CGMD result. Every exploration method was applied using the computation resource of 10,000[node×hour].

A total of $12 \times 12 \times 12 = 1,728$ filler candidate points were set in a grid manner, that is, 12 points were set in each of X, Y, and Z directions at equal intervals, to define a filler morphology in every trial. The radius of the filler was $10[\sigma]$. In the random sampling, 250 of the 1,728 candidate filler points were randomly selected as fillers. In the combined method of the random sampling and the gradient ascent, the randomly selected filler coordinates were improved by the gradient ascent until the stress converged as described in Subsection 3.4.2. In the method using the replica exchange MCMC, 4 parallel MCMC sequences were employed. Figure 3.9 presents the target distributions $P(S^t)$ defined in Equation (3.2). The hyper-parameter α_t in Equation (3.2) reflecting the temperature t to the distribution was set to $(\alpha_1, \alpha_2, \alpha_3, \alpha_4) = (0.5,\ 2.5,\ 10,\ 70)$. The hyper-parameter λ in Equation (3.1) was set to 1/8. $P(S^{t_1})$ was designed to search the filler morphologies having higher stress, whereas $P(S^{t_4})$ was designed to search the wider filler morphology space. $P(S^{t_2})$ and $P(S^{t_3})$ were set to largely overlap with the distributions of the other layers to introduce the frequent replica exchanges between these layers which enhance search efficiency. Hyper-parameter d in Equation (3.7), which was the threshold of the neighbor filler candidate points, was $30[\sigma]$. First 5,000 steps of the MCMC sequence were abandoned for burn-in, and the exchanges of filler morphologies between the adjacent temperature sequences were attempted every 3,000 MCMC steps. The learning rate η in Equation (3.9), mini-batch size B in Equation (3.10), and virtual displacement δ in Equation (3.11) for measuring the

gradient in the gradient descent were 1.0, 5, and 0.1[σ] (1/100 of the filler radius), respectively. CGMD simulations were performed with 1020 cpus using a HPCI system. Table 3.1 presents the sampling parameters used for this search.

Table 3.1: Parameters for the morphology exploration.

Replica exchange MCMC	Total number of temperatures T	4
	α_t in Equation(3.2)	$(\alpha_1, \alpha_2, \alpha_3, \alpha_4)$ =(0.5, 2.5, 10, 70)
	Hyper parameter λ in Equation(3.1)	1/8
	Parameter d in Equation(3.7)	30[σ]
	Interval of replica exchange	3,000[MCMC steps]
Gradient ascent	learning rate η	1.0
	mini-batch size B	5.0
	virtual displacement δ	0.1[σ]

Table 3.2 and Figure 3.10 present the comparison of the exploration performances. Table 3.2 shows the number of the explored filler morphologies providing the CGMD-measured stress equal to or larger than 0.65, and the averages of the CGMD-measured stresses over all explored filler morphologies. Figure 3.10 shows distributions of the CGMD-measured stresses. The histogram of each method was drawn by the CGMD-measured stresses of twenty morphologies randomly sampled from the morphologies resulted by each method. The random sampling, which provides the baseline performance, did not find filler morphologies providing the stress over 0.65, and the average stress of explored morphologies was the smallest. Both the gradient ascent method and the replica exchange MCMC method could find the morphologies providing larger stress than the random sampling respectively, but only one morphology having the stress over 0.65 was obtained by the replica exchange MCMC. Whereas, the proposed method combining the replica exchange MCMC and the gradient ascent found eleven morphologies over 0.65. This result

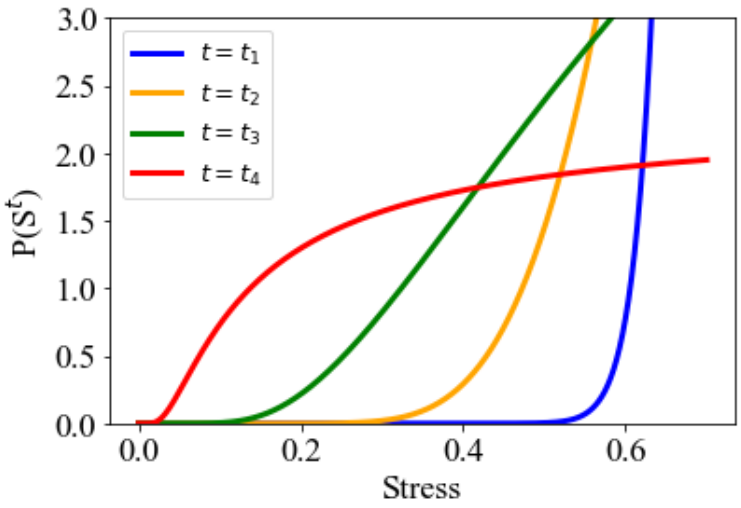


Figure 3.9: Target distributions of each temperature. The blue line, $t = t_1$, is the probability distribution at the lowest temperature. The red line, $t = t_4$, is the probability distribution at the highest temperature. The orange and green lines, $t = t_2$ and $t = t_3$, are the probabilities at the temperatures between and $t = t_1$.

demonstrates the high exploration efficiency of the proposed method. In the proposed method, 20 morphologies were presumed to provide large stress over 0.65 by the CNN-based surrogate model, and 11 morphologies among the 20 provided by the CGMD-measured stress were actually over 0.65. This result indicated the superior extrapolation capability of the CNN-based surrogate model as described in Chapter 2, while the CNN was the interpolation model of the training instances providing the stresses up to 0.6.

Table 3.2: Performance comparison of the random sampling method, the combined method of the random sampling and the gradient descent, the method using the replica exchange MCMC only, and the proposed method.

Sampling technique	The number of the sampled filler morphologies providing CGMD measured stress of 0.65 or larger.	Average of CGMD-measured stresses.
Random sampling method	0	0.33
Combined method of random sampling and gradient decent	0	0.46
Replica Exchange MCMC	1	0.52
Proposed method (replica exchange MCMC and gradient decent)	11	0.66

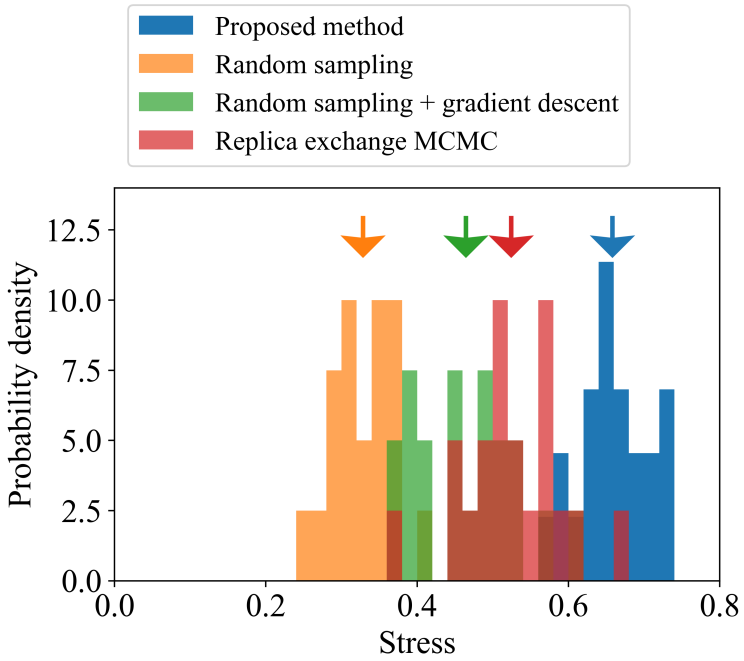


Figure 3.10: Distributions of the CGMD-measured stress of the morphologies obtained by each method. These histograms are normalized and the width of bins is 0.02. Arrows of the same colors with the distributions represents the averages of each stress distribution. The proposed method presents the larger stress distribution than the other methods. This result elucidates the high sampling performance of the proposed method.

3.6 Insights on optimal filter morphologies

We performed the filler morphology exploration using the proposed method with the parameters described in the Section 3.5. Then, 130 candidate morphologies that CNN-based surrogate model showed stress over 0.6 were obtained. The distribution of the CGMD-measured stress of these 130 morphologies is presented in Figure 3.11. The figure also compares it with the stress distribution of the random sampling based on our existing knowledge which was already shown in Figure 3.6 (a). Approximately, half of the CGMD-measured stress of the sampled morphologies are higher than the stress of 0.6 which is in the top 0.1% of the random sampling result, and some morphologies provide the extremely high stress, such as stress of 0.8 or higher. Whereas, the other half of the sampled morphologies provide the stress of 0.6 or lower. However, almost all sampled morphologies are beyond the stress of 0.4, which is in the top 3.5% of the random sampling based on our existing knowledge.

These 130 filler morphologies obtained by our proposed method were preliminary analyzed by Persistent Homology(PH) in order to gain new insights to reach the extremely high stress, though their detailed analysis were conducted in Chapter 4 [Car09]. PH is a mathematical method for investigating the hidden structure in complex data and has been applied previously to analyze polymerized materials [AEK$^+$17][OHK18][IOH17][HNH$^+$16][ZC05]. Let us assume that there are k balls centered at $z_1, z_2, \cdots, z_k$ as shown in Figure 3.12. In this study, each filler particle is represented by a ball with radius r. $k = 250$ is the total number of filler particles, and z_i denotes the coordinate of the center of the i-th filler particle. All balls are disconnected at small values of r, as shown in the upper left figure of Figure 3.12 (a). As r increases to r_1, the balls coalesce to give "birth" to a loop, as shown in the left center figure of Figure 3.12 (a). Furthermore, the empty space enclosed by the loop is completely covered by balls at $r = r_5$, as shown in the right bottom figure of Figure 3.12 (a) and the loop disappears. This example shows that a loop has a "birth" length $b_1 = r_1^2$, and a "death" length $d_1 = r_2^2$, and that the loop exists only when $b_1 < r^2 < d_1$. In addition to the loop, other loops emerges at $r_2 = \sqrt{b_2}$, and $r_4 = \sqrt{b_3}$, then disappears at $r_3 = \sqrt{d_2}$, and

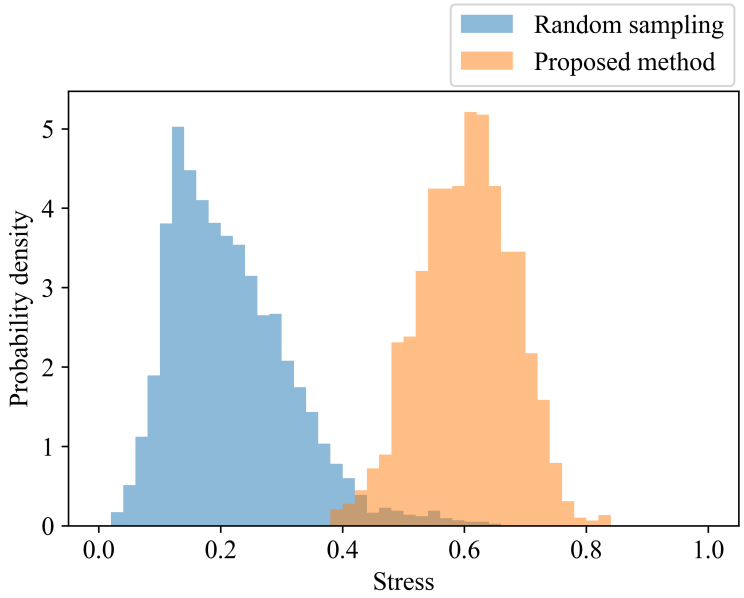


Figure 3.11: Stress distributions of the morphologies obtained by the proposed method and the morphologies sampled by the random sampling based on our existing knowledge. These histograms are normalized and the width of bins is 0.02. The resultant stresses of the proposed method exceed the stress of 0.4, which is in the top 3.5 % of the random sampling.

$r_5 = \sqrt{d_3}$, respectively. PH is the map corresponding to the region spanning from $\{z_1, z_2, \cdots, z_k\}$ to $\{(b_1, d_1), (b_2, d_2), \cdots, (b_l, d_l)\}$, where l is the number of loops formed by k filler particles in a space. The result of the PH analysis is visualized in the scatter plot of (b_i, d_i) depicted in Figure 3.12 (b), which represents a persistent diagram (PD).

Figure 3.13 (a) displays the PDs of all six morphologies providing the stress over 0.6, which were obtained by the random sampling in the Section 3.3. As described in Section 3.3, the random sampling found only these six morphologies providing the stress over 0.6. Figure 3.13 (b) displays the PDs of randomly selected three morphologies providing the stress over 0.65, which were obtained by the proposed method. Comparing these PDs indicates that the proposed method could sample

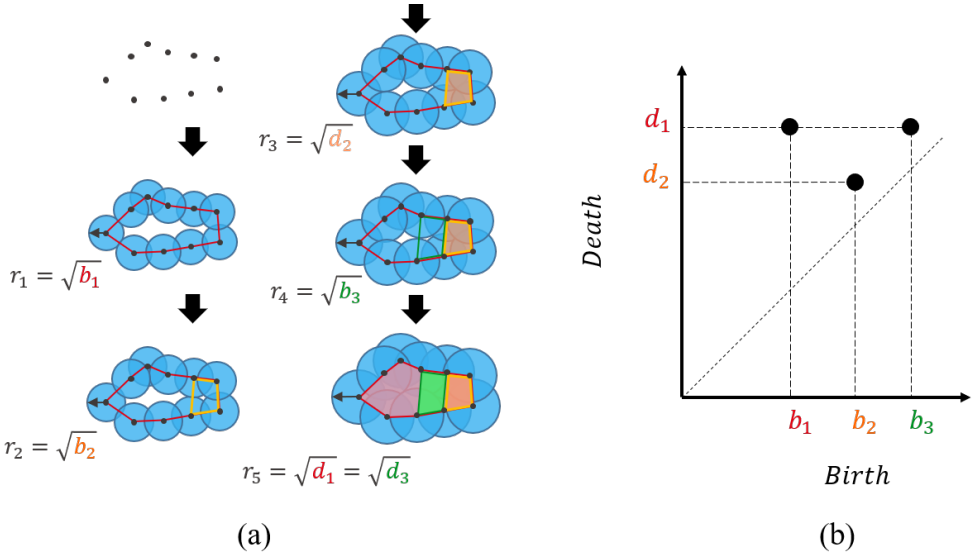


Figure 3.12: Schematic diagram illustrating the PH. (a)The balls are disconnected when the ball radius r is smaller. A loop emerges at $r_1 = \sqrt{b_1}$. Another loop emerges at $r_2 = \sqrt{b_2}$, and disappears at $r_3 = \sqrt{d_2}$. A newly loop emerges at $r_4 = \sqrt{b_3}$. The loops emerged at $r_2 = \sqrt{b_2}$ and $r_4 = \sqrt{b_3}$ disappears at $r_5 = \sqrt{d_1} = \sqrt{d_3}$. (d) PD representing the results of PH analysis.

filler morphologies not obtained by the random sampling. The morphologies obtained by the proposed method obviously show longer life time (difference between death length and birth length) in the PDs. This is resulted by the significant difference of the death length distributions between the proposed method and the random sampling method rather than their difference of the birth length distributions. This fact implies that the morphologies obtained by the proposed method comprise of larger aggregates of filler particles than the morphologies obtained by the random sampling. In addition, some morphologies obtained by the proposed method have greater aggregates whose birth lengths and death lengths are beyond 0.5 and 0.7, respectively. Such complex structures were hardly found by the random sampling.

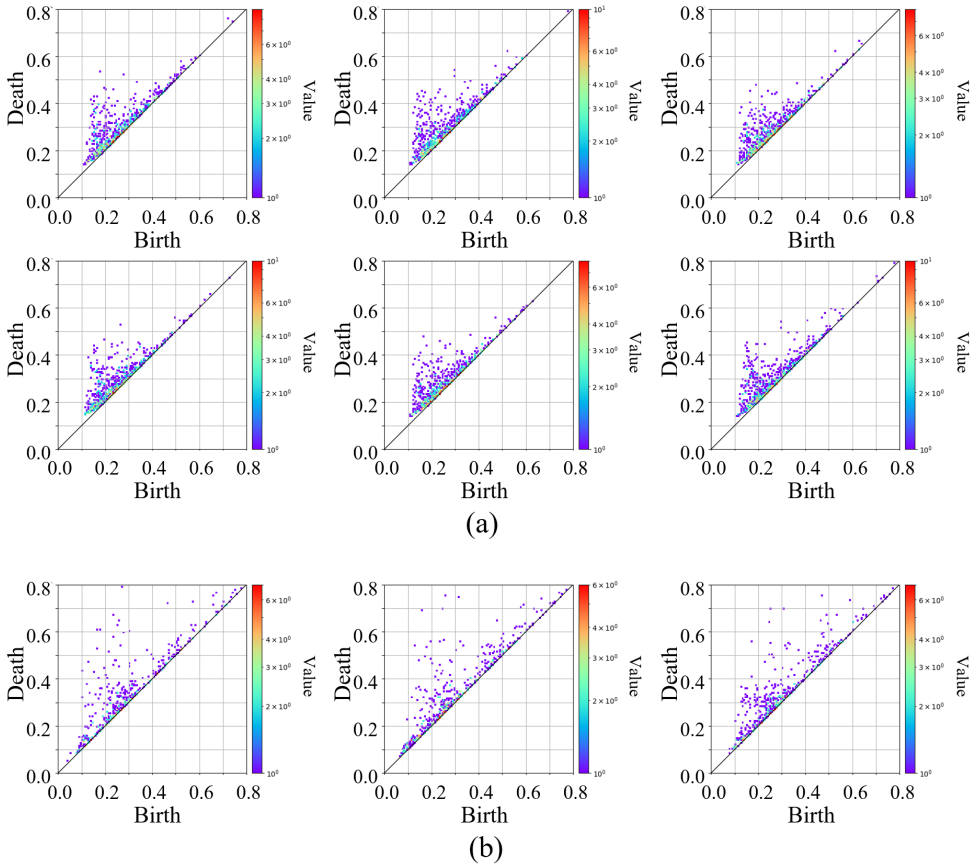


Figure 3.13: Persistent diagrams: (a) filler morphologies obtained by the random sampling, the morphology on the upper left provided the stress over 0.65, while the other morphologies provided the stress from 0.6 to 0.65, and (b) filler morphologies, which provided the stress over 0.65, sampled by the proposed method. Larger death length than the persistent diagrams of the random sampling implies there are the greater aggregates of filler particles in the morphologies obtained by the proposed method.

3.7 Conclusion

In this Chapter, we proposed a novel approach exploring for rare filler morphologies providing the desired property. The approach is a hybrid of the probabilistic and deterministic search methods. The approach is the combination of the surrogate model, the replica exchange MCMC, the gradient descent, and the physical model based computer simulation, such as CGMD. In the exploration using the replica exchange MCMC, we reduced the exploration space dramatically by introducing discrete filler candidate positions and the spin state at the candidate points. The filler morphologies explored by the replica exchange MCMC with the surrogate model were updated by the surrogate model based gradient descent in order to further find filler morphologies that provide better property. The physical model based computer simulations were lastly performed to validate whether the sampled morphologies actually show the desired property. In this dessertation, CGMD simulation was employed. We demonstrated the higher sampling efficiency of the proposed method than these of the random sampling method, the combined method of random sampling and gradient descent, and the method using replica exchange MCMC only. Lastly, we performed the exploration of the filler morhpologies having extremely high stress using the proposed method. Through the PD based comparisons of the filler morphologies obtained by the proposed method and the random sampling method, we demonstrated the possibility that the filler morphologies having the variety of the aggregate structures of the fillers induce high stress.

Some problems still remain for future. For example, the improvement of the surrogate model of CGMD simulation by using the morphologies obtained in Section 3.6 is needed. As mentioned previously, ML provides the interpolation function of the training data, hence, the prediction accuracy on the exploration space which includes a few training data is low. The training data used for the training of the surrogate model included only a few morphologies providing the high stresses. Thus, as shown in Figure 3.11, CGMD-measured stresses of the obtained morphologies are distributed from 0.4 to 0.8, while the CNN-estimated stresses of all explored morphologies were distributed from 0.6 to 0.65. The difference between

the CGMD-measured stresses and the CNN-estimated stress was caused by the prediction accuracy of the CNN-based surrogate model used in the exploration. Therefore, the improvement of the surrogate model by retraining is needed to decrease the difference. Another problem is the optimization of the hyper-parameters for the exploration. Regarding the replica exchange MCMC, the following are to be optimized to obtain many numbers morphologies in a limited exploration period —more efficient exploration—: the number of the layers, the interval of the change of the layer, the target distributions of each temperature, the distribution of the filler candidate positions, and so on. In addition, the parameters included in the gradient descent are also to be studied.

Chapter 4

Analysis on Microstructure-Property Linkages

4.1 Introduction

In Chapter 3, we proposed the novel search method for the microstructure that induced a desired material property and obtained filler morphologies leading to an extremely high stress, which could not be easily identified by random sampling. In this Chapter, we propose methods for quantitatively analyzing the microstructures, in order to reach a better understanding of the mechanical properties. To the best of our knowledge, no machine learning (ML) techniques have been applied to analyze complex filler morphologies, although ML has been applied to the microstructure analysis of metals and magnets as a part of the material design field called "materials informatics" [EFK$^+$19][HCG$^+$20]. These studies used ML to highlight the features or find the most important features explaining a property. Regarding the filled rubber, past studies succeeded constructions of the property prediction model using ML, namely, the a microstructure-property linkage same as Chapter 2 [LHA$^+$21][HM19]. However, inputs of these model were the classical features, e.g., the volume fraction of the filler or the filler type. Thus, they did not succeed in the discussion of the impact on the complex filler morphology, because these features cannot explain the effect of filler morphology sufficiently. Other studies used ML to convert an experimental image to its high resolution image [HHJ18]. However, there have no past studies using ML to investigate the mechanisms of the mechanical property, because there is no technique to deal with the complex filler morphology. In other word, to our knowledge, the study in this chapter is the first

study addressing the analysis of the complex filler morphology by extracting the important structure.

In this dissertation, two machine learning techniques are developed to extract core parts in the complex microstructure that induce the desired properties. The first method is based on a logistic regression (LR) analysis [TM16]. The microstructure is quantified by persistent homology (PH), and the core parts in the microstructure are extracted based on the trained regression coefficients. The second is a CNN based method. The core parts strongly contributing to the desired properties are highlighted by the convolution filter learnt in the CNN. By assessing results of the both methods, we clarify the features of the core parts in the microstructure and their induction mechanism of the desired properties. As a last part of our study, CGMD simulations are performed to demonstrate the validity of the insights obtained by our proposed method.

Note that the analytical method proposed in this Chapter is not limited to the analysis of the filler morphology of filled rubber, though an application example considering the filled rubber is presented in this Chapter. Whenever a dataset composed of imaged microstructure and material property is generated, our method is applicable. For example, this technique can be used for microphase-separated structure of polymer alloy, magnetic material, and metal.

The remainder of this chapter is organized as follows. The problem setting is explained in Section 4.2. In Section 4.3, the methodology to analyze the features of the filler morphology is proposed. The result of the morphology analysis is presented in Section 4.4. The validation using CGMD, i.e., whether the revealed feature actually contributes to the high stress, is performed in Section 4.5. The last Section 4.6 concludes this Chapter.

4.2 Problem setting for filled rubber analysis

In this chapter, we proposed a method to analyze the features of given filler morphologies having a desired property. The method was applied to filler morphologies that provided a stress of 0.6 or higher, which were obtained by random sampling and the sampling method developed in Chapter 3.

In the proposed analysis method, a problem which analyses the microstructures with a classifier established by ML was formulated. Once the classifier was trained, the core structures increasing the stress was identified by the classifier in order to analyse the microstructures. A positive morphological example was composed of morphologies providing a stress of 0.6 or higher at 20 vol.%, and a negative morphological example included morphologies generating a stress of 0.5 or less at 20 vol.%. The stress gap of 0.1 between the positive and negative examples was introduced to ensure clear differences between the positive and negative examples. Figure 4.1 displays the stress distribution of the filler morphologies with a filler volume fraction of 20 vol.% that is a part of morphologies presented in Figure 3.11. The radial distribution functions (RDFs), which is a classical method for quantification of the filler morphology, of the positive and negative examples are shown in Figure 4.2. These RDFs overlap over the entire region and, therefore, cannot be used to distinguish between the positive and negative examples.

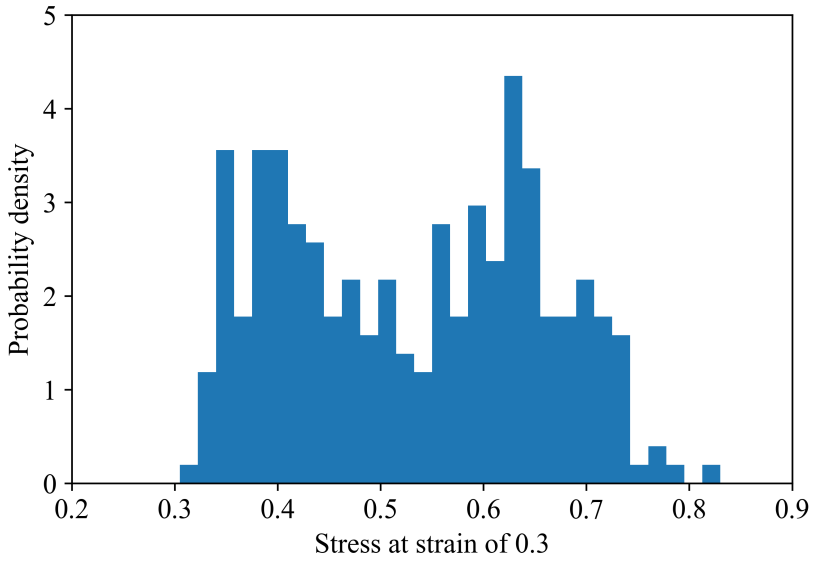


Figure 4.1: Stress distribution of the morphologies obtained by the random sampling and the proposed method in Chapter 3 with a filler volume fraction of 20 vol.%.

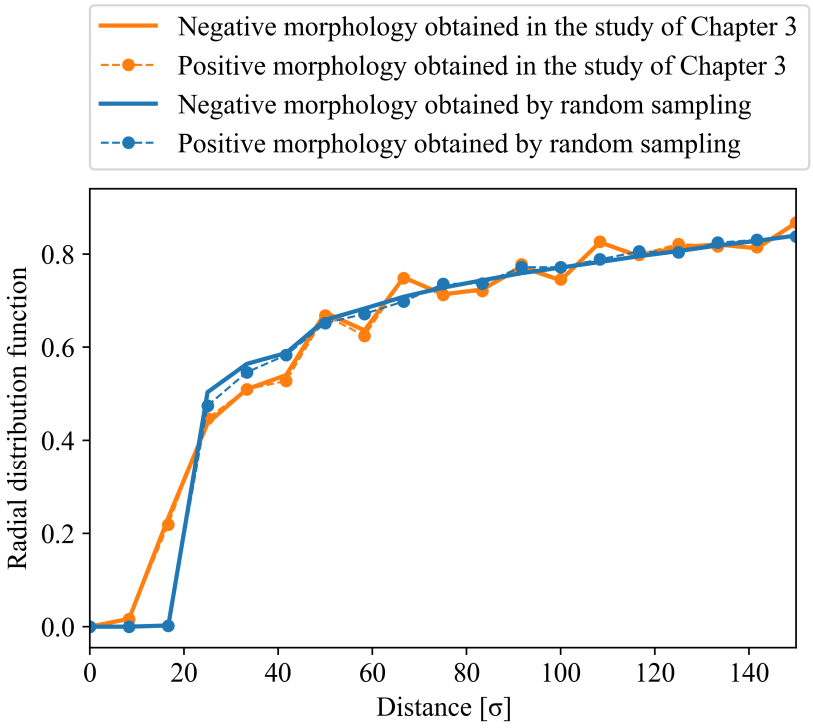


Figure 4.2: RDFs of the filler particles in the positive and negative examples. The blue lines denote the RDFs of the morphologies obtained by random sampling, and the orange lines represent the RDFs of the morphologies obtained in the study of Chapter 3. The solid and dotted lines show the RDFs of the negative and positive examples, respectively.

4.3 Analysis method for filler morphology

Two classification models were established for solving the binary classification problem: an LR-based model and a CNN-based model. In these models, a positive example includes a set of morphologies producing a stress of 0.6 or higher at a filler volume fraction of 20 vol.%, as described in Section 4.2. A negative example represents a set of morphologies leading a stress of 0.5 or less.

Trained LR coefficients can be interpreted as the weights of all input parameters because LR is a logarithmic–linear regression model. Thus, the input parameters that influence the output can be identified based on the trained weights. A barrier to using LR for the analysis of filler morphology comes from the difficulty to appropriately design the features that can characterize structures with high stress. An example feature representation is to vectorize the pixel values of an imaged filler morphology. However, a drawback of this vectorization method is its vulnerability on image conversion. For example, the vectorized image of the original image differs from the vectorized image of a rotated image because each vector component does not correspond to the pixels of the same fillers. This difference implies that an image conversion operation (such as rotation) changes the parameters or features of the input data. Thus, LR using a straightforward vectorization cannot evaluate the effect of each feature on the output stress. To avoid this problem, this study employed a devised approach that filler morphologies were quantified by a persistent homology (PH), and the quantified features are vectorized by constructing a persistence image (PI) same as past studies [IOH17][ZC05][HNH$^+$16][AEK$^+$17]. The obtained vectors were used as the input parameters to the LR model.

On the other hand, morphology quantification is not required when a CNN–based classification model is employed because it can automatically extract features of the input images through their convolutions. In this study, CNN–based classification model, which output a probability that an imaged filler morphology input was positive, was established to extract the filler particles producing a strong influence on mechanical properties. This CNN–based model that consisted of a convolutional layer of the imaged filler morphology could extract the filler particles related to the objective mechanical properties in the image.

4.3.1 LR and PH analysis

Filler morphologies were quantified by PH introduced in Section 3.6. PH is a map from the region spanned by the set of filler positions, $\{z_1, z_2, \cdots, z_k\}$, to the features of the loops consisting of fillers $\{(b_1, d_1), (b_2, d_2), \cdots, (b_K, d_K)\}$, where K is the number of loops formed by k filler particles in the region. The result of the PH analysis is visualized in the scatter plot, PD, as in Section 3.6. The PD on R^2 was converted into a vector using the PI in order to use the input data for LR. First, PD=$\{(b_i, d_i)|i = 1, \cdots, l\}$ was mapped onto the persistence surface ρ as follows:

$$\rho(x, y) = \sum_{i=1}^{l} w(b_i, d_i) exp\left(-\frac{(b_i - x)^2 + (d_i - y)^2}{2h^2}\right), \quad (4.1)$$

$$w(b, d) = \arctan(\beta (d - b)^{\gamma}). \quad (4.2)$$

Here, $\beta > 0$, $h > 0$, and $\gamma > 0$ are the given parameters. $w(b, d)$ and h are the weight function and standard deviation of the Gaussian distribution, respectively. Any function can be used as a weight function. In this study, to emphasize the characteristic loops with long lifetimes (the difference between the death length and the birth length), the arctan function used in many past studies was employed as the weight function[OHK18]. γ was set to 3. The PD space was discretized into $g \times g$ subdomains, and the persistence surface was integrated in every subdomain. The integrated persistence surface values of all the subdomains were arranged in form of a finite-dimensional vector. The integrated persistence surface values of the subdomains in the upper left half of the PD space were arranged in such a way that their birth and death occurred in the ascending order. The vectorized PD is the PI. Figure 4.3 depicts the vectorization procedure and resultant PIs of the two morphologies. As shown in the figure, the PIs significantly reflected the difference of the morphologies from each other.

The obtained dataset consisted of the PIs and stress-based positive/negative classes determined by the CGMD. The trained classification model estimating the probability p of the positive example was constructed using LR as follows:

$$\text{logit}(p) = \ln\left(\frac{p}{1 - p}\right) = \sum_{i=0}^{l} \omega_i PI_i \quad (4.3)$$

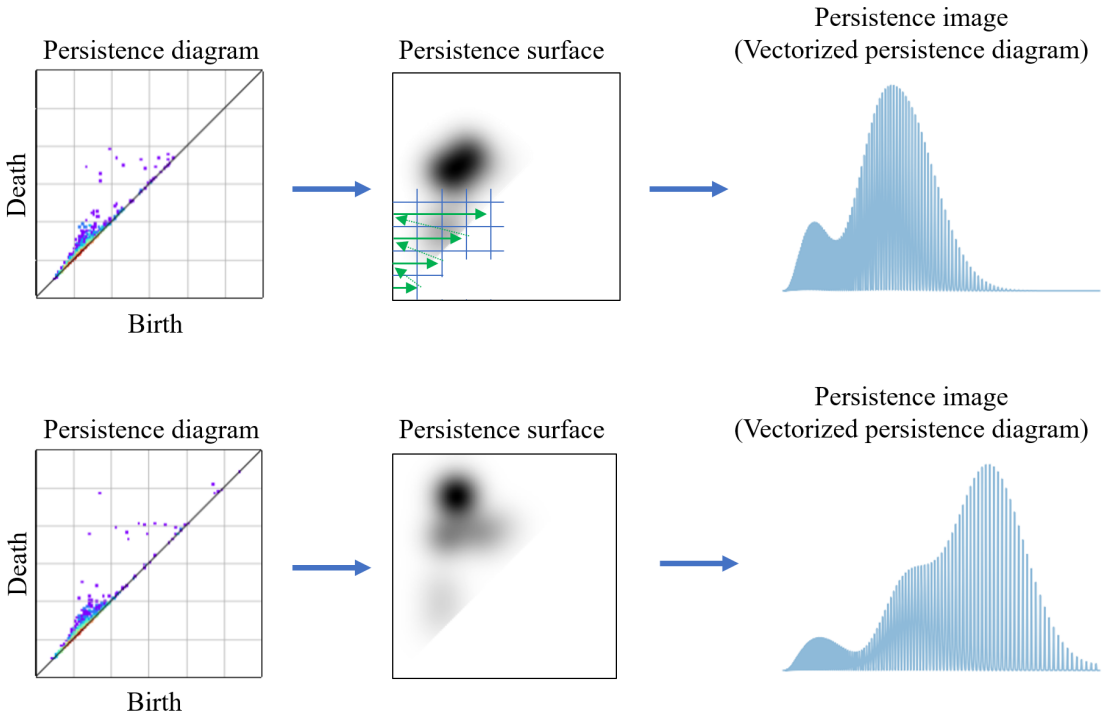


Figure 4.3: Schematic illustration of the vectorization procedure. The left plots include the PDs; the center figures are the persistence surfaces; and the right histograms contain the PIs. Two morphologies are vectorized in the upper and lower figure panels. As shown in the upper center figure, the persistence surface is divided by a grid, and representative values of all grid cell are arranged along the green arrows.

where ω_i is the weight of each PI component and is a parameter to be trained. l is the number of PI components in the upper left part of the discretized PD space, which is defined as follows:

$$l = \sum_{i=1}^{g} i \tag{4.4}$$

An L1 regularization term with a regularization parameter $c = 1.0$ was added to the loss function to avoid overfitting. L1 regularization can reduce the dimension of ω by assigning zeros to multiple regression coefficients. PD regions that dominate the output were identified based on the trained nonzero ω values, and the filler

particles related to the positive/negative example were predicted by extracting the loops corresponding to the PD regions directed by the nonzero w.

In this study, PH analysis was performed under the periodic boundary conditions similar to those of the CGMD. The obtained dataset was divided into training data, validation data, and test data with a ratio of 8:1:1. The optimal parameters were determined by estimating the accuracy of the classification model trained by the training dataset with respect to the validation data not used for training. The prediction accuracy was measured by using the test data not used for training and validation. The hyperparameters to be trained were h in Equation (4.1), β in Equation (4.2), and g in Equation (4.4). The best combination of these parameter values was found from=$\{0.001, 0.0015, 0.002\}$, $\beta = \{0.001, 0.01, 0.1\}$, and $g = \{16, 32, 64, 128\}$ by a grid search algorithm. Figure 4.4 shows the prediction accuracies estimated by the validation data. The combination $(h, \beta, g) = (0.002, 0.01, 128)$ provided the highest accuracy, and this combination gave the same level of accuracy for the test data.

Figure 4.5 shows the distribution of the trained LR coefficient in the PD space. As shown in Figure 4.3, PI, *i.e.,* an LR input vector, was generated by converting the PD representing the finite data set $\{(b_i, d_i)|i = 1, \cdots, l\}$ into the continuous data (persistence surface) and discretized. Thus, the trained coefficient, ω, can be interpreted as the weight for each region in the PD. The PD region corresponding to PI_i where the regression coefficient is positive, contributes to the positive example. In contrast, the PD region corresponding to PI_i where the regression coefficient is negative contributes to the negative example. The region between (birth, death) = (0.015,0.05–0.07) and (birth, death) = (0.018,0.03–0.04) contribute to the positive and negative examples, respectively in Figure 4.5, and some loops extracted from both regions are presented in Figure 4.6. The loops larger than the modeled space size were resulted from the PH performed under the periodic boundary conditions. We will compare the loops extracted from each class in the next section.

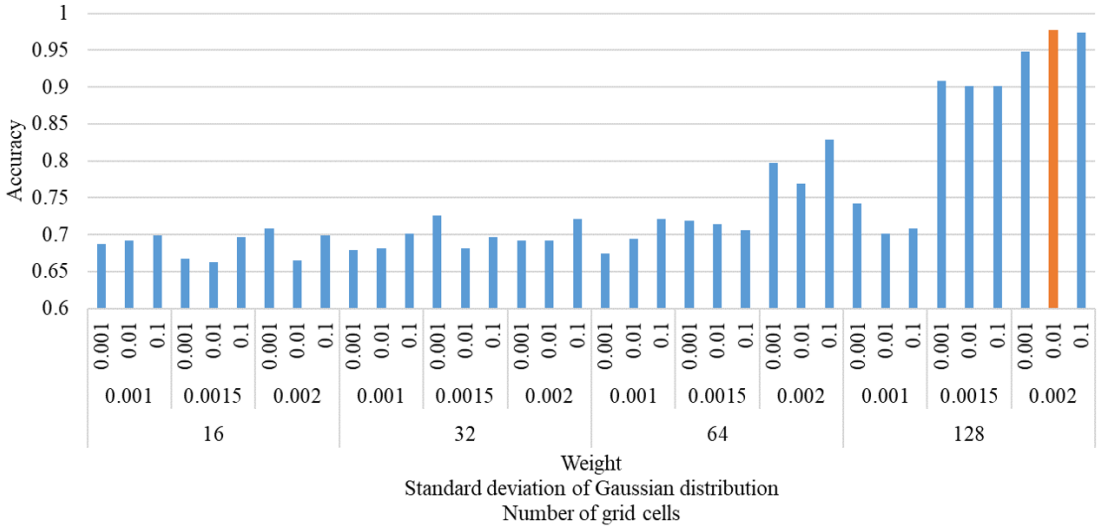


Figure 4.4: Prediction accuracies of the validation data with different combination of hyperparameters. The accuracy was defined as the ratio of the number of morphologies that predicted the correct class to the number of validation data instances. The top row in the horizontal axis is the weight on the persistence surface β; the middle row is the standard deviation of the Gaussian distribution h; and the bottom row is the number of subdomains g. The orange bar represents the combination of parameters that produces the highest accuracy.

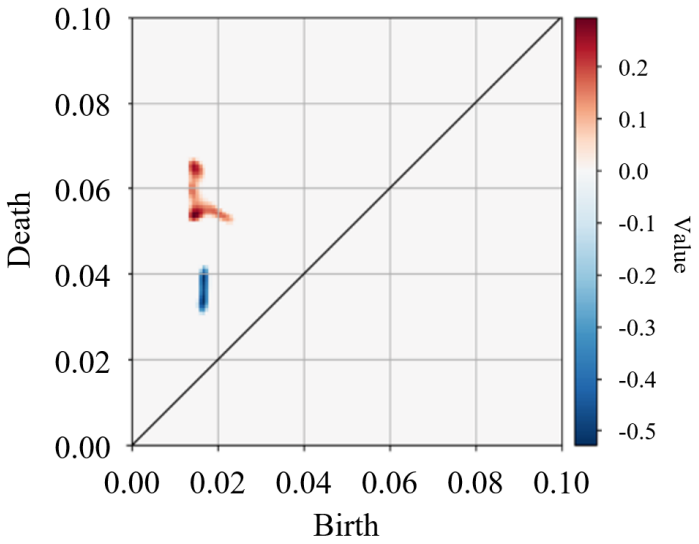


Figure 4.5: Distribution of the L1 regularized LR coefficient, which predicts a stress-based class from the vectorized filler morphology. The coefficient is visualized in the PD space. The red region corresponds to the positive coefficients and contributes to the positive example. The blue region corresponds to the negative coefficients and contributes to the negative example.

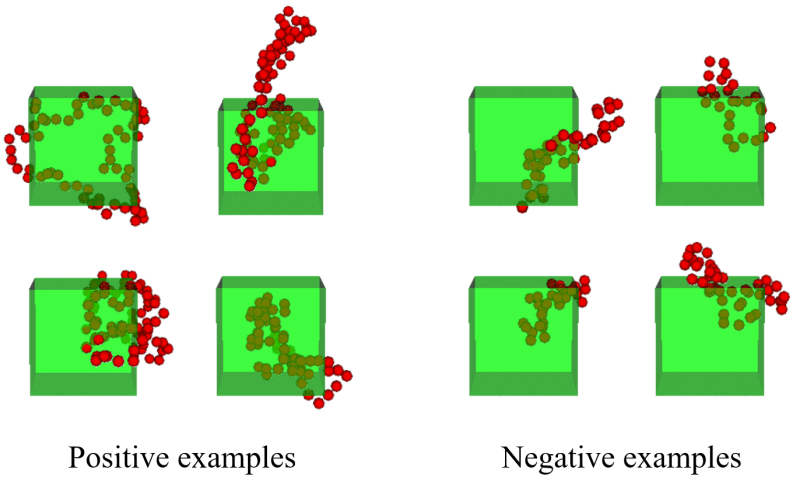


Figure 4.6: Examples of the loops composed of filler particles, which were extracted by the PH. The green box denotes the modeled space, and the red dots represent the filler particles.

4.3.2 CNN–based analysis

The CNN input data consist of a filler morphology image; therefore, morphology quantification is not required. The regions contributing to the positive and negative examples are extracted by analyzing the sensitivity of each pixel of the input image to the output using the trained classification model. Thus, the fillers in the extracted regions were considered to be strongly related to the mechanical properties of filled rubber.

However, the trained classification model is a "black box" and is hardly interpretable. Hence, extracting the dominant region (as was done by LR) employing a CNN with a complex architecture is difficult. To alleviate this issue, the simplest CNN, which contained only a convolutional layer without a fully connected layer as depicted in Figure 4.7, was utilized in this work. Here, the input image was translated into the output by the CNN via the following procedure. First, the input image was convoluted by only one filter. Second, a leaky rectified linear unit (leaky ReLU) [MHN13] and global average pooling [LCY14] were applied to the convoluted image for the reduction into a scaler. Finally, the predicted class was output through a sigmoid function. According to this architecture of the CNN, the predicted output class was a positive example when the average of the pixel values of the convoluted image was positive. The negative example was predicted when the average of the pixel values was negative. In this way, the positive/negative judgments could be done easily. In addition, the regions of the input image that dominate the output class can also be estimated from the coordinates of the pixels with positive/negative values in the convoluted image.

In the training of the CNN, batch normalization was performed to stabilize the training after the leaky ReLU [PLW19][IS15]. The kernel moved with a stride of one in the convolutional layer under the periodic boundary conditions so that both the center and the edge of the input image could be evaluated at the same weight, and the size of the convoluted image was equal to the size of the input image. Therefore, the filler particles within a kernel sized region in the input image correspond to an output pixel values in the convoluted image, and thus the filler particles with the kernel sized space resolution can be easily extracted as the fillers contributing to

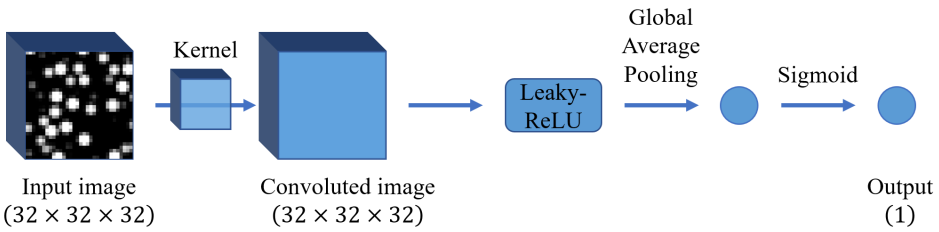


Figure 4.7: CNN architecture utilized in this work. The numbers in parentheses represent the dataset sizes. The input image of $32 \times 32 \times 32$ pixels is convoluted into the image of $32 \times 32 \times 32$ pixels under the periodic boundary conditions with a single kernel. The leaky ReLU function and global average pooling were applied to the convoluted image to reduce the dimension. Finally, the probability of the positive example is output using the sigmoid function.

the positive example if their output pixel value is positive. The same extraction of the filler particles with the kernel sized space resolution applied to the negative example.

To investigate the relationship between the kernel size and prediction accuracy, the prediction accuracies achieved at kernel sizes of $5 \times 5 \times 5$, $9 \times 9 \times 9$, and $13 \times 13 \times 13$ were compared. The dataset consisted of pairs of every input image with a size of $32 \times 32 \times 32$ as shown in Figure 4.7 and its stress-based class. The dataset was divided into training data, validation data, and test data with a ratio of 8:1:1 similarly to the dataset used for LR in Section 4.3.1. The batch size and learning rate were 50 and 0.0005, respectively. Adam was used as the optimization algorithm [KB15]. The prediction accuracy was measured every four epochs by using validation data not used for training, in order to select a model presumed to provide the highest generalization performance. The resultant CNN learning curves are shown in Figure 4.8. The prediction accuracies of all kernel sizes at an epoch of 100 were equal to 1.0. The prediction accuracies measured using the test data were also 1.0.

Figure 4.9 shows a comparison between the input image and the convoluted

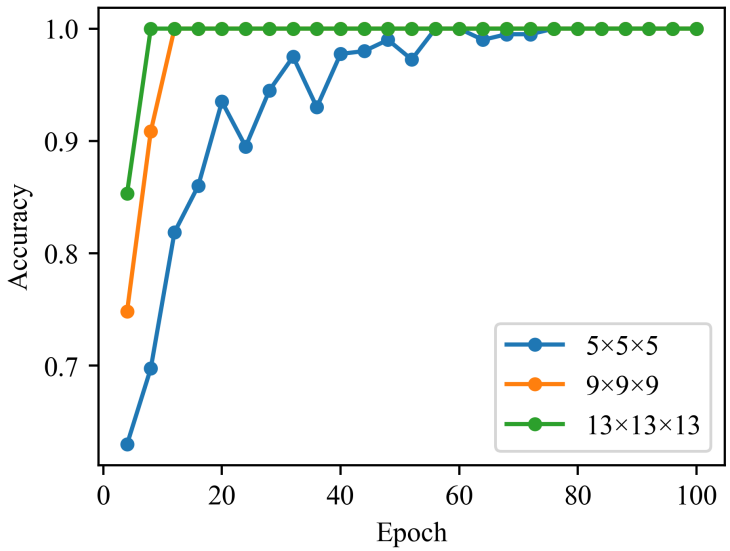


Figure 4.8: Relationships between the epoch number and prediction accuracy determined by applying the validation data. The prediction accuracy was equal to the ratio of the number of morphologies that predicted the correct class to the number of validation data instances. The blue line, orange line, and green line correspond to the prediction accuracies of the kernels with sizes of $5 \times 5 \times 5$, $9 \times 9 \times 9$, and $13 \times 13 \times 13$, respectively.

image, which is passed through the convolution filter learnt by the CNN. The sizes of both images were $32 \times 32 \times 32$, and 16 cross-sectional images of every 2 pixels in depth were presented. Because the elastic modulus of the filled rubber is roughly proportional to the filler volume fraction, the region contributing to the positive example (the pixels of the convoluted image with positive values) is presumed to be a region where many fillers exist in the input image. Actually, the red pixels with positive values of the convoluted image obtained using the kernel with a size of $9 \times 9 \times 9$ matched a filler in the input image as shown in the lower left figure of Figure 4.9. In contrast, the red regions, which had the positive pixel values of the convoluted image with a kernel size of $5 \times 5 \times 5$, were located in the rubber region of the input image. The number of pixels and the space size of the input image

were $32 \times 32 \times 32$ and $170[\sigma] \times 170[\sigma] \times 170[\sigma]$, respectively; thus, approximately $5.3[\sigma]$ was imaged with a pixel. Hence, four pixels were required to image the filler particle with the radius $r = 10\,[\sigma]$ used in this study. Therefore, the kernel with a size of $5 \times 5 \times 5$ could not convolute all information about filler aggregates (including connections with the adjacent filler particles) because the kernel convoluted only one filler particle. Accordingly, the CNN predicted the class by evaluating the rubber region rather than the filler aggregates, and the pixels with positive values in the convoluted image were distributed across the rubber region. On the other hand, a stripped pattern was constructed in the convoluted image using the kernel with a size of $13 \times 13 \times 13$. This is because the kernel size of $13 \times 13 \times 13$ is too coarse to capture the characteristics of the filler distributions in the input image. Meanwhile, the kernel with a size of $9 \times 9 \times 9$ convoluted the space including almost two fillers along the X-, Y-, and Z-directions, respectively. This implies that this kernel evaluated the structure of filler aggregates by convoluting the information of the adjacent filler particles. This procedure resulted in a good match between the pixels with positive values in the convoluted image and the filler particles in the input image.

Figure 4.10 shows the histograms of the fraction of positive pixels in the convoluted image geometrically matching the filler particles in the input image. All morphologies of more than 50 of the positive samples were used for its construction. More than 90% of the positive pixels of the image convoluted by the kernel with a size of $9 \times 9 \times 9$ matched the filler particles in the input image. This result illustrates that the kernel size of $9 \times 9 \times 9$ is appropriate to clarify the filler aggregate-property linkage.

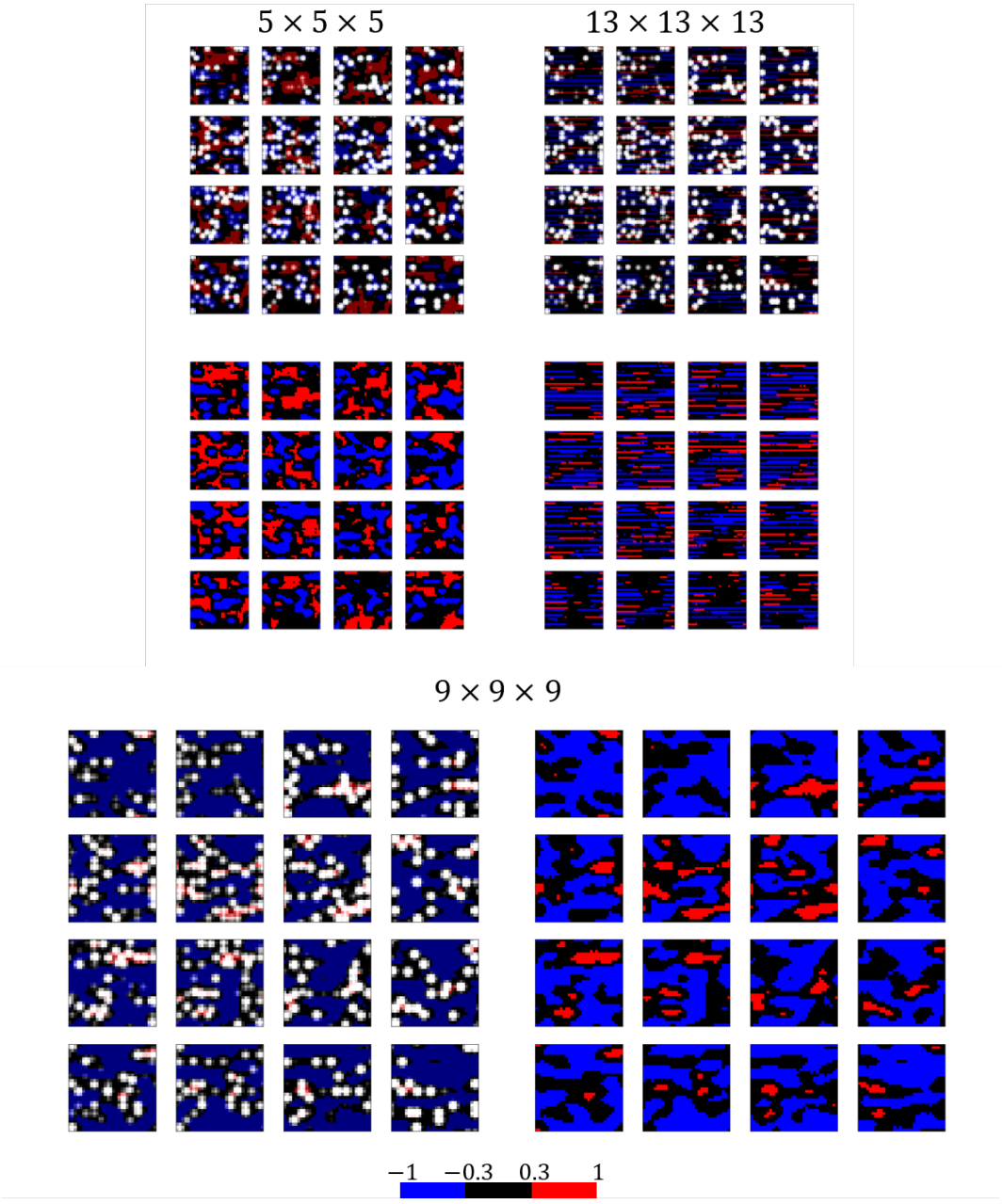


Figure 4.9: Input and convoluted images obtained using the kernels with sizes of $5 \times 5 \times 5$, $9 \times 9 \times 9$, and $13 \times 13 \times 13$. The left figure of $9 \times 9 \times 9$ and the upper figures of $5 \times 5 \times 5$ and $13 \times 13 \times 13$ represent the superimposed images of input and convoluted images. The white circles and black areas denote the filler particles and rubber regions in the input images, respectively. The red and blue areas are visualized in the convoluted images depicted in the lower row and represent the pixels with positive and negative values, respectively. The red areas contribute to the positive example, and the blue areas contribute to the negative example. The pixels with values ranging from -0.3 to 0.3 are visualized in black to emphasize the areas with large contributions.

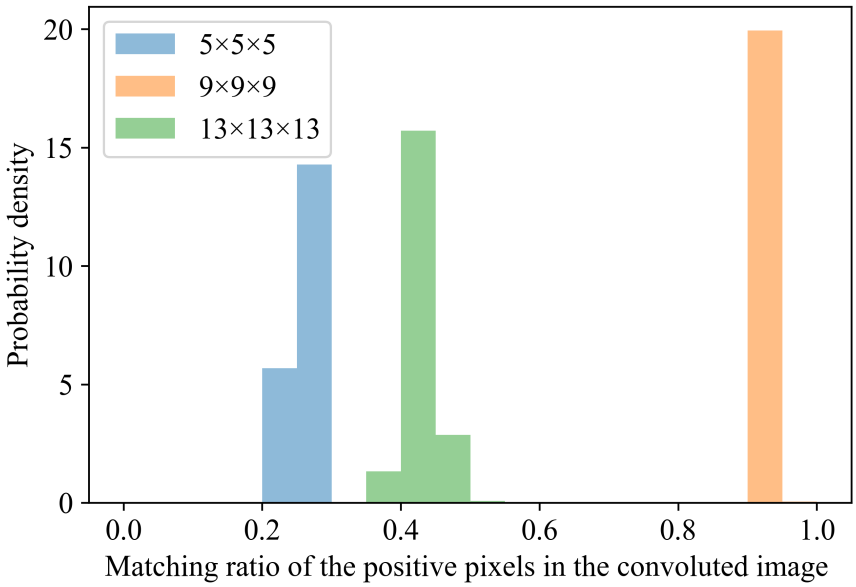


Figure 4.10: Ratio of the positive pixels in the convoluted image to the filler particles in the input image, which was defined as an A/B fraction. These histograms are normalized. Here, A is the number of pixels with positive values in the convoluted image that overlap with the filler particles in the input image. B is the total number of pixels with positive values in the convoluted image. The blue, orange, and green colors correspond to the kernel sizes $5 \times 5 \times 5$, $9 \times 9 \times 9$, and $13 \times 13 \times 13$, respectively.

4.4 Analysis result

4.4.1 Filler aggregates extracted by the PH and CNN methods

First, the loops consisting of the filler particles extracted from all morphologies in the positive and negative examples by the PH method were compared based on the regression coefficients of LR with L1 regularization presented in Section 4.3. For doing so, we introduced the following radius of gyration, R_g.

$$R_g = \sqrt{\frac{1}{F}\sum_{n=1}^{F}(r_n - r_g)^2} \tag{4.5}$$

$$r_g = \frac{1}{F}\sum_{n=1}^{F} r_n \tag{4.6}$$

F is the number of filler particles, and r_g and r_n are the center of gravity of the loop and the coordinate of the filler particle contained in this loop, respectively.

In this study, the loop extracted by the PH was considered as a filler aggregate because the loop represented a set of filler particles from the PH perspective. Figure 4.11 indicates that both R_g and F values of the positive example are apparently larger than those of the negative example, suggesting that the positive example included larger aggregates than those of the negative example.

The aggregate sizes were compared in all directions to investigate the shape difference between the aggregates extracted from the positive and negative examples as shown in Figure 4.12. In this study, the size in each direction was defined as the difference between the largest and smallest coordinates along this direction. The aggregates extracted from the positive example were larger than those extracted from the negative example in all directions. Specifically, the difference in aggregate size in the Z-direction (the elongation direction of the system) between the positive and negative examples was apparently larger than those in the X- and Y-directions. Hence, the morphological characteristics leading to a higher stress in the positive example were larger size in all directions, especially along the deformation direction.

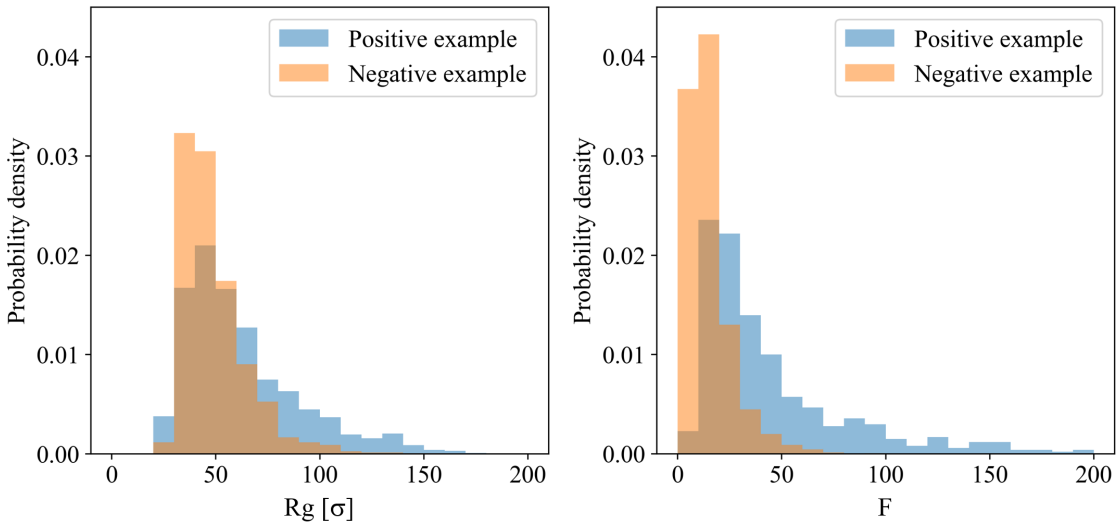


Figure 4.11: Normalized histograms of the radius of gyration, R_g, and the number of filler particles in the loop, F, of the filler aggregate extracted by the PH. The blue bars and orange bars denote the aggregates extracted from the positive and negative examples, respectively.

Note that PH did not impose a restriction on the overlapping constituent particles over multiple loops. Therefore, some filler particles were extracted as constituents of different loops as depicted in Figure 4.13. In this study, the loop extracted by the PH was considered a filler aggregate, as described above. This means that the i-th and j-th loops in Figure 4.13 represent different aggregates, although they were connected physically with the filler particles surrounded by the orange circles. On the other hand, some past studies reported that local rubber regions sandwiched by the filler aggregates deform considerably during the deformation process. The resultant stresses are presumed to be the main source of stress in the entire system [AYY$^+$08][MNW$^+$21][KK18]. This implies that the distribution of filler aggregates may be a key factor affecting the mechanical properties of filled rubber. However, it is difficult to measure the actual spatial distribution of the filler aggregates using the PH loops because these aggregates easily overlap with each other.

Next, the filler morphologies were analyzed using the CNN. In this study, the

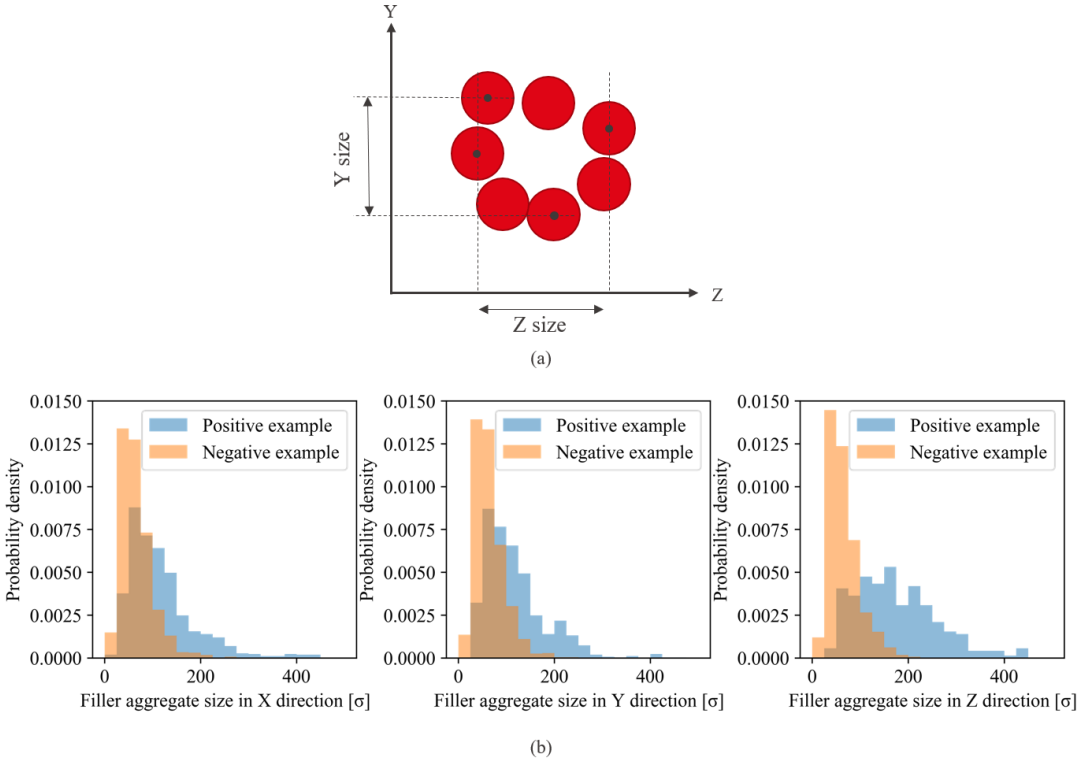


Figure 4.12: (a) Definition of the aggregate size. The red circles and black points represent the filler particles and their centers, respectively. The size in each direction is the difference between the largest and smallest coordinates along this direction. (b) Aggregate size distribution in each direction. The blue and orange bars denote the results obtained for the positive and the negative examples, respectively. Z-direction is the elongation direction of the system, while X- and Y-directions are compressed during deformation.

simplest CNN consisting of a convolutional layer with a kernel was employed, as described in section 4.3.2. This CNN was able to easily extract the filler particles contributing to the stress based on the pixel values of the convoluted image. The pixels with positive values of the convoluted image passing through the filter with the size $9 \times 9 \times 9$ match the filler particles in the input image as shown in Figure 4.10. Therefore, a set of the adjacent pixels with positive values in the convoluted

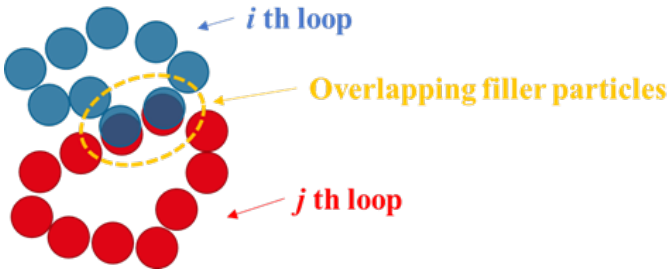


Figure 4.13: Schematic illustration of the filler particles belonging to multiple loops. The blue and red circles denote the filler particles constituting different loops. The particles surrounded by the orange circle belong to both the i-th and j-th loops connected physically. However, these two loops are considered different aggregates.

image was considered as a filler aggregate. Pixels with a value of 0.3 or higher were extracted as they strongly contributed to the positive example. In this study, filler aggregates were represented by the filler particles located in the area contributing to the positive example of the convoluted image, although the aggregate in a broad sense also included the filler particles located in the neighborhood of the extracted area. The aggregate size was measured in each direction as the difference between its largest and smallest coordinate as depicted in Figure 4.14(a) similar to the PH analysis. Figure 4.14(b) displays the distributions of filler aggregate sizes, which indicate that the aggregates extracted from the positive example tended to be larger than those extracted from the negative example. In particular, the size difference in the Z-direction (the elongation direction of the system), was large. This was similar to the result of the PH analysis. However, the results presented in Figure 4.12(b) indicate that the sizes of the aggregates extracted by the PH were larger than those of the aggregates extracted by the CNN in all directions. This difference resulted from the nature of these algorithms utilized for extracting filler aggregates by these two techniques: the PH could extract larger aggregates than CNN because some filler particles constituted multiple PH loops.

The aggregates extracted from all morphologies in the positive example by the PH and those extracted by the CNN were compared. The aggregate extracted by

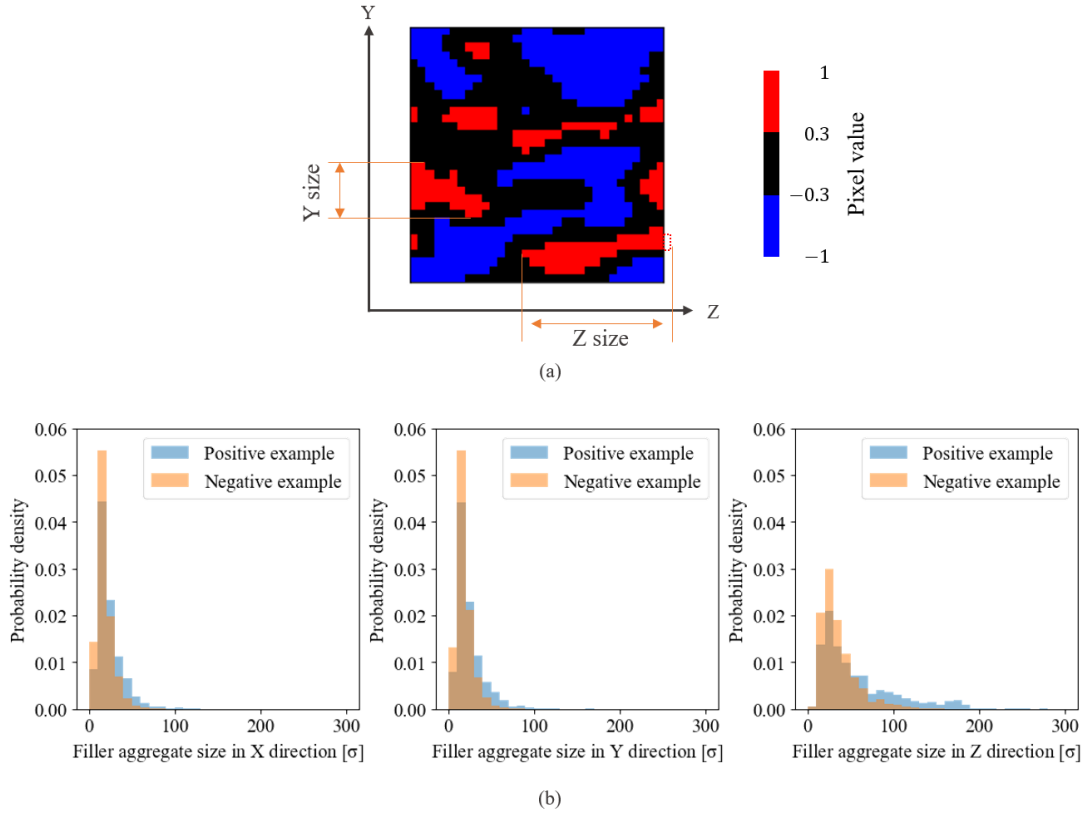


Figure 4.14: Example of the aggregate extracted by the CNN and size distributions of filler aggregates. (a) Cross-section of the convoluted image. The aggregate size is defined as the difference between the largest and smallest pixel coordinates. The red/blue regions are the set of pixels with positive/negative values that contributes to the positive/negative example, respectively. The black region includes pixels with small values ranging from -0.3 to 0.3 and does not affect the output. The adjacent red pixels are extracted under the periodic boundary conditions. (b) Histograms of the size of the set of pixels with positive values, namely aggregate sizes, obtained from all morphologies in the positive (blue bars) and negative (orange bars) examples. Z is the elongation direction of the system.

both methods could be considered a core structure that strongly increases the stress and constitutes the positive example. The results presented in Figure 4.15 indicate that more than 80% of filler particles in the morphologies were extracted by the PH. However, only 40% of filler particles in the morphologies were extracted by the CNN. The histogram of the filler particles extracted by the CNN almost overlaps the histogram of the particles extracted by both the CNN and PH. Hence, the filler particles extracted by the CNN were considered a subset of the particles extracted by the PH and presumed to strongly contribute to the mechanical properties of filled rubber.

Based on the all results described in this subsection, the main characteristics of the morphologies that induce an extremely high stress are summarized as follows.

- The larger aggregates induces the higher stress, because the large aggregates in all directions were extracted as the core structure contributing to the large stress, in the analyses using both of the LR and CNN.
- The coincidence of the elongation direction and the longitudinal direction of the aggregate boost the stress, because the size of the extracted aggregate along the elongation direction were especially large.

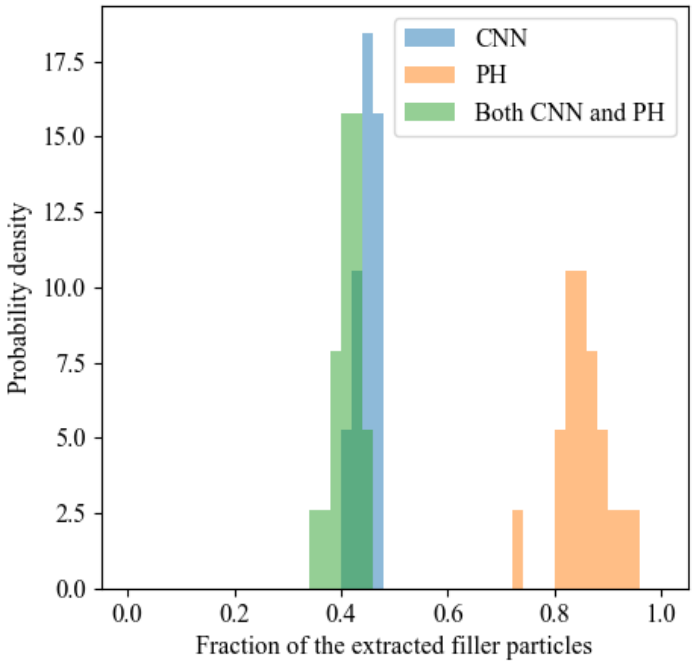


Figure 4.15: Fractions of the filler particles extracted by the PH and CNN that contributed to the positive example. Their values were computed as the ratios of the numbers of pixels of the extracted particles to the number of pixels for all filler particles. The blue bars denote the ratios of the filler particles extracted by the CNN method only; the orange bars represent the ratios of the filler particles extracted by the PH method only; and the green bars denote ratios of the filler particles common to the fillers extracted by the CNN and the fillers extracted by the PH.

4.4.2 Comparison between the extracted and non-extracted filler particles

The extracted filler particles contributing to the positive example and the non-extracted filler particles were compared to clarify a filler morphology producing a higher stress. The filler morphologies were compared using the two-point spatial correlation $L(\boldsymbol{r})$ defined by Equation (4.7) [TBC88][YYAB$^+$18][CDY$^+$18][LK17], where r was a direction vector. $L(\boldsymbol{r})$ was equivalent to the probability that the material of a starting point of r was same as the material of an end point of $\boldsymbol{r}$.

$$L(\boldsymbol{r}) = \frac{1}{\rho|V|}\sum_{\boldsymbol{x}\subset V} m_{\boldsymbol{x}} m_{\boldsymbol{x}+\boldsymbol{r}}, \tag{4.7}$$

$$m_{\boldsymbol{x}} = \begin{cases} 1 & \text{if the material of } \boldsymbol{x} \text{ is filler} \\ 0 & \text{otherwise} \end{cases} \tag{4.8}$$

where V, $\boldsymbol{x}$, and $m_{\boldsymbol{x}}$ are a set of the location vectors of all pixels in the images, a location vector of a pixel, and a material indicator of a pixel located at $\boldsymbol{x}$, respectively. $|V|$ is the volume of V. ρ is either the volume fraction of the filler particles extracted by the CNN in V or the volume fraction of filler particles not extracted in V. It was not used in the standard $L(\boldsymbol{r}) = \frac{1}{|V|}\sum_{\boldsymbol{x}\subset V} m_{\boldsymbol{x}} m_{\boldsymbol{x}+\boldsymbol{r}}$ employed in the some studies [TBC88][YYAB$^+$18][CDY$^+$18][LK17]. In this study, $L(\boldsymbol{r})$ of the extracted and the non-extracted filler particles must be normalized using their volume $\rho|V|$, respectively. The upper left and upper right figures in Figure 4.16 show $L(\boldsymbol{r})$ averaged over the fillers non-extracted and extracted from all morphology examples, respectively. Figure 4.16 presents the spatial correlation in the YZ plane of r-space. As shown in Figure 4.12 and Figure 4.14, the features of the extracted filler aggregate along X and those along Y are significantly similar. Hence, only the spatial correlations in the YZ plane were presented in Figure 4.16, because the spatial correlation in the XY plane and that in YZ plane were almost identical. The bottom left and bottom right figures depict $L(\boldsymbol{r})$ averaged over the fillers extracted from all morphologies in the negative and positive examples, respectively. All $L(\boldsymbol{r})$ were computed under the periodic boundary condition in the range of -85$[\sigma] \leq r_i \leq 85\,[\sigma]$, where $r_i, (i = X, Y, Z)$ was the orthogonal coordinate of r. Note

that the cell size was $170[\sigma] \times 170\,[\sigma] \times 170\,[\sigma]$, thus the probability of finding the same material in the half size of the cell were computed as $L\,(\boldsymbol{r})$. Both $L\,(\boldsymbol{r})$ of filler particles extracted from the positive examples and $L\,(\boldsymbol{r})$ of filler particles extracted from the negative examples exhibit an anisotropic distribution with high probability along the elongation direction as presented in the bottom row of Figure 4.16. This anisotropic distribution indicated that the aggregate size along the elongation direction was larger than the aggregate sizes in the other directions, which was consistent with the aggregate characteristics described previously. Meanwhile, $L\,(\boldsymbol{r})$ of the filler particles not extracted by the CNN (see the upper left figure of Figure 4.16) exhibit an isotropic distribution representing the isotropic aggregate shapes such as spheres. Therefore, it was concluded that the reinforcement effect of the isotropically shaped aggregates was not strong, and that the anisotropically shaped aggregates with larger sizes along the elongation direction strongly influenced the produced stress.

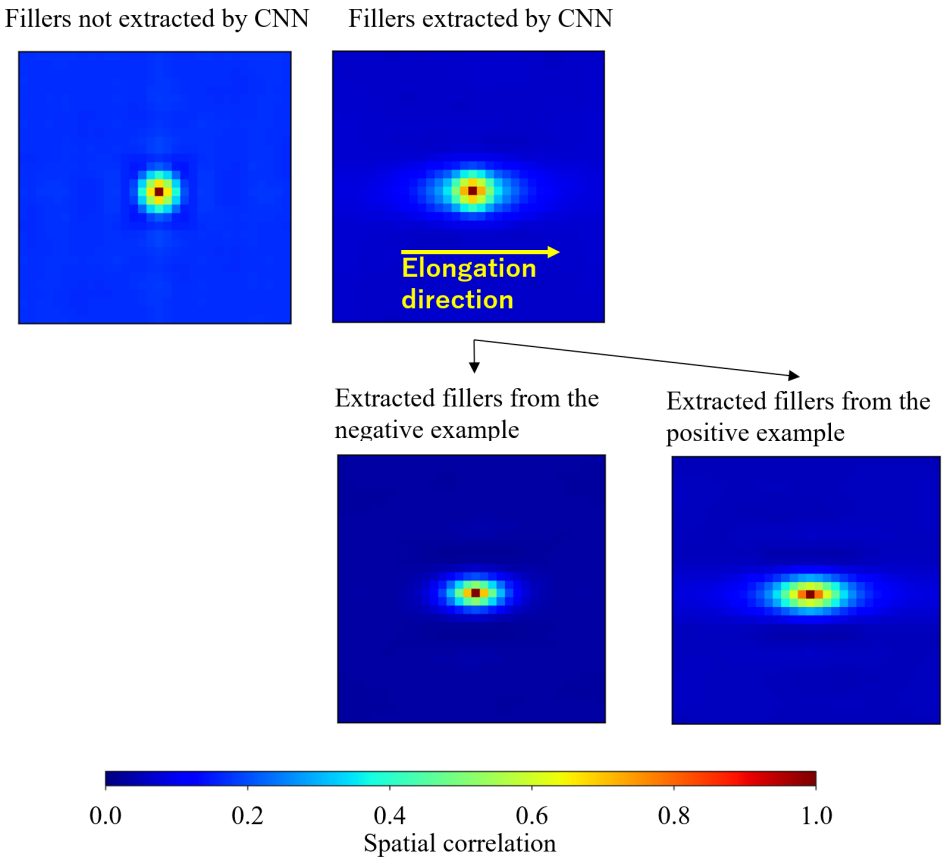


Figure 4.16: Spatial correlations in the YZ plane of r-space including $r = (0, 0, 0)$ of the CNN-extracted fillers from all morphology examples that contribute to the high stress and that of the non-extracted fillers (upper row figures). The isotropic spatial correlation of the fillers not extracted by the CNN suggests the isotropically shaped filler aggregates. Meanwhile, the anisotropic spatial correlation of the filler particles extracted by the CNN indicates that the probability of filler orientation along the elongation direction is high. Furthermore, bottom two figures show the spatial correlations of the extracted fillers from all positive examples and all negative examples, respectively. The higher orientation probability of the filler particles extracted from the positive example along the elongation direction suggests that the aggregate size measured along the elongation direction in the positive example is larger than the size of the negative example.

4.5 Validation using computer simulation

CGMD simulations were performed to assess if the CNN extracted filler particles actually contributed strongly to the mechanical properties and provided the high stress. For this purpose, the difference of stresses at the strain of 0.3 generated by the CNN extracted fillers were compared with the stress generated by the same number of randomly arranged fillers. Ten filler morphologies consisting of the fillers extracted by the CNN and other ten filler morphologies consisting of randomly arranged fillers, i.e., twenty morphologies in total, were generated. Then, CGMD simulations stretching these morphologies to a strain of 0.3 were performed under the same strain velocity with the CGMD simulation in Section 2.3, and the resultant stresses were compared.

Here, the morphologies provided the stress of 0.6 or higher were used to extract the fillers using CNN. The filler particles , which geometrically matched the positive pixels in the convoluted image, were extracted from the morphologies. The space size of all morphologies and the radius of filler particles were $170[\sigma] \times 170\,[\sigma] \times 170\,[\sigma]$ and $10[\sigma]$, respectively, same as the Section 4.2. Note that these extracted filler aggregates of all filler morphologies were oriented along Z-direction, and the elongation direction of the CGMD simulations was also Z-direction. In addition, CGMD simulations of the CNN extracted filler morphologies stretching along the X- and Y-directions were also performed to investigate the relationship between the elongation directions and filler aggregate shapes.

Figure 4.17 shows the stress distributions resulted by these CGMD simulations. A comparison between the blue and green bars in Figure 4.17 revealed that the stresses generated by the CNN-extracted aggregates were larger than the stresses produced by the randomly arranged filler particles during the elongation along the Z-direction. This result confirmed the validity of the proposed method for extracting filler aggregates that would likely contribute to the mechanical properties. It is also confirmed that the anisotropic shape of filler aggregate increases the stress. A comparison of the blue and orange bars in Figure 4.17 shows that the produced stress increases when the elongation direction matches the principal direction of the filler aggregates. This result suggests that the connection of filler particles along

the elongation direction has a stronger impact on the reinforcement effect than the collision of filler particles induced during the deformation along the X- and Y-directions.

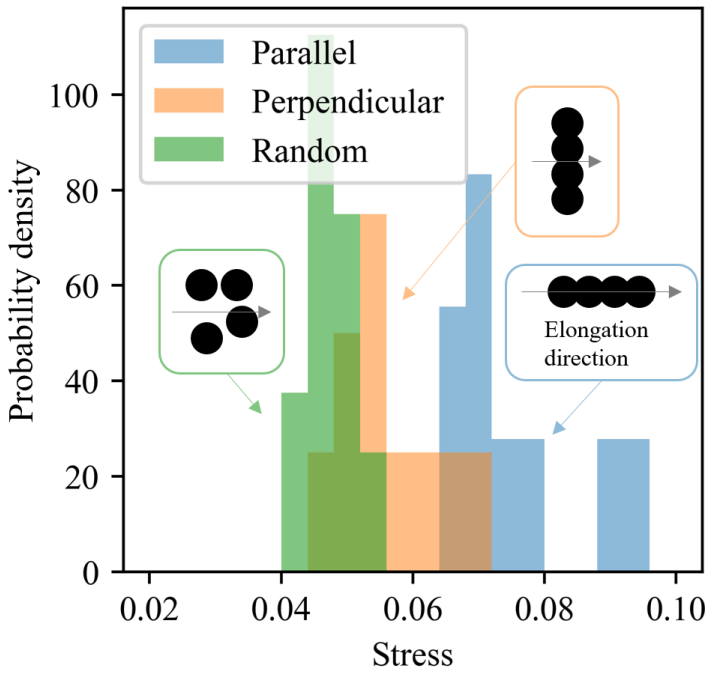


Figure 4.17: Distributions of the CGMD-simulated stress at a strain of 0.3. The blue bars denote the results obtained for the CNN-extracted aggregates from the positive example. The Z-direction was the elongation direction. The orange bars represent the elongation of the CNN-extracted filler aggregates along the X- and Y-directions. The elongation direction was perpendicular to the aggregate principal direction (Z) in these cases. The green bars denote the results obtained for the filler configurations, in which the particle positions were randomly determined with the filler volume equal to that for the blue bars. Schematic diagrams of the filler aggregates and elongation direction are shown in the rectangles with the frame colors identical to those of the corresponding bars. The black circles and arrows designate the filler particles and the elongation direction, respectively.

4.6 Conclusion

We developed a machine learning based method for analyzing the relationship between the microstructure and the desired property. Then we analyzed the features of filler morphology producing an extremely high modulus to better understand the mechanical properties of filled rubber. For this purpose, we formulated a binary classification problem for the CGMD-measured stress at a strain of 0.3 and investigated the filler morphologies obtained in Chapter 3 by two different methods. First, filler morphology was quantified by the PH and PI, and an LR-based classification model was developed. The filler aggregates that strongly contributed to the stress were extracted based on the coefficients of the trained classification model. Second, a CNN was applied to establish another classification model. The aggregates contributing to stress generation were extracted based on the image convoluted by the kernel. They revealed that the aggregate size along the elongation direction was an important factor affecting stress generation because both methods extracted the filler aggregates whose sizes in the elongation direction were larger on average than those in the other directions. It was also found that the larger aggregates induced higher stress values. In addition, the CNN-based classification model revealed that the dense aggregate distribution (the short distance between aggregates) was another important factor influencing the stress value. These results that anisotropical shape of the aggregate and deformation along the primary direction of the aggregate were the key to increase the stress were confirmed by the CGMD simulations.

In this Chapter, we focused on only the size of the filler aggregate along X, Y, and Z direction for an easy understanding. An analysis using another representation of the filler aggregate is future work. In addition, an investigation between the stress and other features of filler morphology, e.g., the distribution of the filler aggregate, also remains for future work.

Chapter 5

Conclusion

5.1 Discussion

In this dissertation, the novel methodology for the material design was developed. The developed method for the investigation into the microstructure-property linkage using machine learning and computer simulation is composed of the following steps:

Step-1

Development of a surrogate of a physical model for a high speed simulation of a material property. We employed a CNN to learn the surrogate model from the physical simulation results.

Step-2

Global search for desired microstructures in their discrete representation space, and the succeeding local search to find the microstructures providing the better desired properties. We employed a replica exchange MCMC and a gradient descent method for the global search and the local serach, respectively. In these search, the use of high-speed simulations is essential for the efficient search. We used the surrogate model of the CGMD simulation developed in Step-1 for the high-speed simulations. Finally, the original physical model based computer simulations are carried out to confirm the material properties of the searched microstructures.

Step-3

Quantitative analysis of the microstructures and material property linkage using machine learning techniques. Core parts impacting on the material prop-

erty in the complex microstructure are extracted by using machine learning. We employed the two machine learning techniques: CNN and logistic regression analyses.

In this dissertation, we focused on the linkage between the filler morphology of the filled rubber and its stress at strain of 0.3. However, the proposed method can be applied to analyses on any microstructure and material property linkages if the dateset which consist of the imaged mictostructure and material property value is generated same as the dateset used in this study. For example, in case of the filled rubber, the proposed method can be applied to analyze other properties, such as hysteresis, toughness, and frequency characteristics. A microphase-separated structure of polymer alloy for the better permittivity or gas permeability, and electronegativity of an ionic solids are also suitable to use the proposed method. Furthermore, any methods of Step-1, 2 and 3 can be independently applied to analyses on the material properties. For instance, the sampling method in Step-2 is not limited to its use with the surrogate model established in Step-1, and can be combined with any simulator as far as it enables high speed simulations. In addition, the analytical method in Step-3 is not limited to the application to the microstructures obtained in Step-2, and can be used for any microstrucures. For instance, some characteristic structures inducing different material properties can be extracted by comparing a set of microstructures having a material property and a set of microstructures having another property.

5.2 Conclusion

This dissertation proposed the novel methodology for study on the material microstructure.The methodology was applied to the filler morphology and stress linkage analysis.

First, we introduced the high-speed simulator established using a CNN as a surrogate model learnt from the small number of the CGMD simulation results in Chapter 2. We established the high-speed simulator which estimates the material properties. We demonstrated the superior estimation accuracy of the high-speed

simulator through numerical examples. This technique allows us to perform an extremely fast iterative sampling of the microstructure needed in following Chapter 3.

Next, we proposed an efficient sampling method for the complex microstructure inducing given properties in Chapter 3. The method is a combination of the replica exchange MCMC, the gradient descent method, the high-speed simulator, and the original physical model based computer simulation. The replica exchange MCMC searches the microstructures in their discrete representation space globally, and the succeeding gradient descent method searches locally to find the microstructure providing better desired properties. In these sampling, the high-speed simulator introduced in Chapter 2 is employed to efficiently compute the mechanical property and its dependence on the microstructure for the efficient sampling. Finally, the physical model based computer simulations are carried out to confirm the material properties of the searched microstructures. The performance of the proposed method was evaluated through numerical examples.

Chapter 4 proposed two methods for quantitatively analyzing the microstructures. Two machine learning techniques are developed to extract core parts in the complex microstructure that induce the desired properties. The first method is based on a logistic regression analysis. The microstructure is quantified by persistent homology, and the core parts in the microstructure are extracted based on the trained regression coefficients. The other is a CNN based method. The core parts strongly contributing to the desired properties are highlighted by the convolution filer learnt in the CNN. Comparing the results of both methods, we clarified the features of the core parts in the microstructure and their mechanism inducing the desired properties. Lastly, the physical model based computer simulations are performed to validate the linkage between the core parts in the microstructure and the desired properties.

The developed method in this dissertation can provide the desired microstructures hardly obtained based on the experimental study and simulation based study, and reveal the features controlling the material properties. Thus, the method can be widely applied to other microstructured materials and we believe that this method strongly contributes to the advancement of materials science in various fields. Com-

bining the computer simulation and ML, the computational cost which is one of the biggest issue of the computer simulation was reduced dramatically, and the iterative sampling and the desired parametric study were to be feasible. Additionally, this dissertation is the first subject employing the ML for the analysis of the complex filler morphology. Meanwhile, the exploration performance of the desired morphologies depends on the estimation accuracy of the ML-based high speed simulator used in the exploration. Hence, a study on a method for improving the prediction accuracy of the surrogate model is needed, in order to explore the desired morphology more efficiency.

Moreover, materials are required to balance multiple properties in high levels in many cases. Extension of our proposed methodology to the analyses on linkages between microstructures and multiple properties remains as an important future work.

Bibliography

[AC19] A. Agrawal and A. Choudhary. Deep materials informatics: Applications of deep learning in materials science. *MRS Communications*, 9(3):779–792, 2019.

[AEK+17] H. Adams, T. Emerson, M. Kirby, R. Neville, C. Peterson, P. Shipman, S. Chepushtanova, E. Hanson, F. Motta, and L. Ziegelmeier. Persistence images: A stable vector representation of persistent homology. *Journal of Machine Learning Research*, 18:1–35, 2017.

[APM+21] R. Abdusalamov, P. Pandit, B. Milow, M. Itskov, and A. Rege. Machine learning-based structure-property predictions in silica aerogels. *Soft Matter*, 17(31):7350–7358, 2021.

[AYY+08] K. Akutagawa, K. Yamaouchi, A. Yamamoto, H. Heouri, H. Jinnai, and Y. Shinbori. Mesoscopic mechanical analysis of filled elastomer with 3D-finite element analysis and transmission electron microtomography. *Rubber Chemistry and Technology*, 81(2):182–189, 2008.

[BGD+13] G. P. Baeza, A. Genix, C. Degrandcourt, L. Petitjean, J. Gummel, M. Couty, and J. Oberdisse. Multiscale filler structure in simplified industrial nanocompositeSilica/SBR systems studied by SAXS and TEM. *Macromolecules*, 46(1):317–329, 2013.

[BRHS+20] A. Belessiotis-Richards, S. G. Higgins, S. P. Sansom, A. Alexander-Katz, and M. M. Stevens. Coarse-grained simulations suggest the epsin N-terminal homology domain can sense membrane curvature without its terminal amphipathic helix. *ACS Nano*, 14(12):16919–1692, 2020.

[BS00] D. Beach and J. Schroeder. Overview of tire technology. *Rubber World*, 222(6):44–53, 2000.

[Car09] G. Carlsson. Topology and data. *Bulletin of the American Mathematical Society*, 46(2):255–308, 2009.

[CDY+18] A. Cecen, H. Dai, Y. C. Yabansu, S. R. Kalidindi, and L. Song. Material structure-property linkages using three-dimensional convolutional neural networks. *Acta Materialia*, 146:76–84, 2018.

[CMWC14] J. Carrete, N. Mingo, S. Wang, and S. Curtarolo. Nanograined half-heusler semiconductors as advanced thermoelectrics: An ab initio high-throughput statistical study. *Advanced Functional Materials*, 24(47):7427–7432, 2014.

[Cor] JSOL Corporation. Available online: https://www.j-octa.com/.

[CSW+12] S. Curtarolo, W. Setyawan, S. Wang, J. Xue, K. Yang, R. H. Taylor, L. J. Nelson, Gus L.W. Hart, S. Sanvito, M. Buongiorno-Nardelli, N. Mingo, and O. Levy. A distributed materials properties repository from high-throughput ab initio calculations. *Computational Materials Science*, 58:227–235, 2012.

[CZC+14] S. Chong, P. Zhang, W. Claus, R. Schuster, and S. Zhao. Combined dielectric and mechanical investigation of filler network percolation behavior, filler-filler contact, and filler-polymer interaction on carbon black-filled hydrogenated acrylonitrile-butadiene rubber. *Rubber Chemistry and Technology*, 87(4):647–663, 2014.

[CZN+21] L. Chen, W. Zhang, Z. Nie, S. Li, and F. Pan. Generative models for inverse design of inorganic solid materials. *Journal of Materials Informatics*, 1(4):1–15, 2021.

[Dan75] E. M. Dannenberg. Effects of surface chemical interactions on the properties of filler-reinforced rubbers. *Rubber Chemistry and Technology*, 48(3):410–444, 1975.

[DB93] J. B. Donnet and R. C. Bansal. *Carbon black: science and technology, Second Edition.* 1993.

[DCN+16] M. De Jong, W. Chen, R. Notestine, K. Persson, G. Ceder, A. Jain, M. Asta, and A. Gamst. A statistical learning framework for materials science: application to elastic moduli of k-nary inorganic polycrystalline compounds. *Scientific Reports*, 6(34256):1–11, 2016.

[DE90] M. Doi and S. Edwards. The theory of polymer dynamics. *Oxford University Press*, 1990.

[DJP20] D. Arias-Molinares and J. C. García-Palomares. The Ws of MaaS: Understanding mobility as a service fromaliterature review. *IATSS Research*, 44:253–263, 2020.

[DTT+19] H. Doi, K. Takahashi, K. Tagashira, J. Fukuda, and T. Aoyagi. Machine learning-aided analysis for complex local structure of liquid crystal polymers. *Scientific Reports*, 9(16370):1–12, 2019.

[E. 45] E. Guth. Theory of filler reinforcement. *Rubber Chemistry and Technology*, 18(3):596–604, 1945.

[ED05] D. J. Earl and M. W. Deem. Parallel tempering: Theory, applications, and new perspectives. *Physical Chemistry Chemical Physics*, 7(23):3910–3916, 2005.

[EFK+19] L. Exl, J. Fischbacher, A. Kovacs, H. Oezelt, M. Gusenbauer, K. Yokota, T. Shoji, G. Hrkac, and T. Schrefl. Magnetic microstructure machine learning analysis. *Journal of Physics Materials*, 2(1):1–19, 2019.

[EM95] M. Enrico and G. A. Mansoor. A simple expression for radial distribution functions of pure fluids and mixtures. *The Journal of Chemical Physics*, 103(11):4672–4677, 1995.

[FJF+16] B. Figliuzzi, D. Jeulin, M. Faessel, F. Willot, M. Koishi, and N. Kowatari. Modelling the microstructure and the viscoelastic behaviour of carbon black filled rubber materials from 3D simulations. *Technische Mechanik*, 36(1-2):32–56, 2016.

[FKR12] V. A. Froltsov, M. Klüppel, and G. Raos. Molecular dynamics simulation of rupture in glassy polymer bridges within filler aggregates. *Physical Review E*, 86(041801):1–10, 2012.

[FLE+14] F. S. Bellucci, L. O. Salmazo, E. R. Budemberg, A. R. Guerrero, R. F. Aroca, M. A. de Lima Nobre, and A. E. Job. Morphological characterization by SEM, TEM and AFM of nanoparticles and functional nanocomposites based on natural rubber filled with oxide nanopowders. *Materials Science Forum*, 798-799:426–431, 2014.

[GEK00] G. S. Grest, R. Everaers, and K. Kremer. Stress relaxation of entangled polymer networks. *Journal of Non-Crystalline Solids*, 274:139–146, 2000.

[GLS+14] Y. Gao, J. Liu, J. Shen, L. Zhang, Z. Guo, and D. Cao. Uniaxial deformation of nanorod filled polymer nanocomposites: A coarse-grained molecular dynamics simulation. *Physical Chemistry Chemical Physics*, 16(30):16039–16048, 2014.

[GN21] G. Santos and N. Nikolaev. Mobility as a service and public transport: A rapid literature review and the case of moovit. *Sustainability*, 13(7):1–18, 2021.

[HAK+07] K. Hagita, T. Arai, H. Kishimoto, N. Umesaki, Y. Shinohara, and Y. Amemiya. Two-dimensional pattern reverse Monte Carlo method for modelling the structures of nano-particles in uniaxial elongated rubbers. *Journal of Physics Condensed Matter*, 19(33):1–9, 2007.

[Has70] W. K. Hastings. Monte carlo sampling methods using Markov chains and their applications. *Biometrika*, 57(1):97–109, 1970.

[HCG+20] E. A. Holm, R. Cohn, N. Gao, A. R. Kitahara, T. P. Matson, B. Lei, and S. R. Yarasi. Computer vision and machine learning for microstructural characterization and analysis. *Metallurgical and Materials Transactions A: Physical Metallurgy and Materials Science*, 51(12):5985–5999, 2020.

[HHJ18] K. Hagita, T. Higuchi, and H. Jinnai. Super-resolution for asymmetric resolution of FIB-SEM 3D imaging using AI with deep learning. *Scientific Reports*, 8(5877):1–8, 2018.

[HM19] D. Huri and T. Mankovits. Automotive rubber part design using machine learning. *IOP Conference Series: Materials Science and Engineering*, 659(1), 2019.

[HMDT16] K. Hagita, H. Morita, M. Doi, and H. Takano. Coarse-grained molecular dynamics simulation of filled polymer nanocomposites under uniaxial elongation. *Macromolecules*, 49(5):1972–1983, 2016.

[HNH+16] Y. Hiraoka, T. Nakamura, A. Hirata, E. G. Escolar, K. Matsue, and Y. Nishiura. Hierarchical structures of amorphous solids characterized by persistent homology. *Proceedings of the National Academy of Sciences of the United States of America*, 113(26):7035–7040, 2016.

[HTH+08] K. Hagita, A. Takashi, K. Hiroyuki, U. Norimasa, S. Hiroya, S. Yuya, and A. Yoshiyuki. Structural changes of silica particles in elongated rubber by two-dimensional small-angle X-ray scattering and extended reverse Monte Carlo analysis. *Rheologica Acta*, 47(5):537–541, 2008.

[HTH+18] K. Hagita, T. Tominaga, T. Hatazoe, T. Sone, and H. Takano. Filler network model of filled rubber materials to estimate system size dependence of two-dimensional small-angle scattering patterns. *Journal of the Physical Society of Japan*, 87(014802):1–10, 2018.

[HZCW18] J. Han, L. Zhang, R. Car, and E. Weinan. Deep potential: A general representation of a many-body potential energy surface. *Communications in Computational Physics*, 23(3):629–639, 2018.

[IA96] H. Ismail and Z. Ahmad. Effect of a multifunctional additive on curing characteristics and mechanical properties of carbon blacks filled natural rubber compounds. *Iranian Polymer Journal*, 5(3):207–212, 1996.

[IKT17] Y. Iwasaki, A. G. Kusne, and I. Takeuchi. Comparison of dissimilarity measures for cluster analysis of X-ray diffraction data from combinatorial libraries. *npj Computational Materials*, 3(4):1–8, 2017.

[IOH17] T. Ichinomiya, I. Obayashi, and Y. Hiraoka. Persistent homology analysis of craze formation. *Physical Review E*, 012504(95):1–6, 2017.

[IS15] S. Ioffe and C. Szegedy. Batch normalization: Accelerating deep network training by reducing internal covariate shift. *32nd International Conference on Machine Learning, ICML 2015*, 37:448–456, 2015.

[ISK14] Y. Iba, N. Saito, and A. Kitajima. Multicanonical MCMC for sampling rare events. *Annals of the Institute of Statistical Mathematics*, 66(3):611–645, 2014.

[ISS+19] Y. Iwasaki, R. Sawada, V. Stanev, M. Ishida, A. Kirihara, Y. Omori, H. Someya, I. Takeuchi, E. Saitoh, and S. Yorozu. Identification of advanced spin-driven thermoelectric materials via interpretable machine learning. *npj Computational Materials*, 5(103):1–6, 2019.

[J.9] J. P. Flory. *Statistical mechanics of chain molecules*. Hanser Pub. Inc., 1969.

[JS09] H. Jinnai and R. J. Spontak. Transmission electron microtomography in polymer research. *Polymer*, 50(5):1067–1087, 2009.

[JSK+07] H. Jinnai, Y. Shinbori, T. Kitaoka, K. Akutagawa, N. Mashita, and T. Nishi. Three-dimensional structure of a nanocomposite material consisting of two kinds of nanofillers and rubbery matrix studied by transmission electron microtomography. *Macromolecules*, 40(18):6758–6764, 2007.

[KB15] D. P. Kingma and J. L. Ba. Adam: A method for stochastic optimization. *3rd International Conference on Learning Representations, ICLR 2015 - Conference Track Proceedings*, pages 1–15, 2015.

[KDL+19] G. Kim, H. Diao, C. Lee, A. T. Samaei, T. Phan, M. De Jong, K. An, D. Ma, P. K. Liaw, and W. Chen. First-principles and machine learning predictions of elasticity in severely lattice-distorted high-entropy alloys with experimental validation. *Acta Materialia*, 181:124–138, 2019.

[KG90] K. Kremer and G. S. Grest. Dynamics of entangled linear polymer melts: A molecular-dynamics simulation. *The Journal of Chemical Physics*, 92(8):5057–5086, 1990.

[KK17] J. Krmela and V. Krmelova. Tire casings and their material characteristics for computational modeling of tires. *Engineering for Rural Development*, 16:230–235, 2017.

[KK18] T. Kojima and M. Koishi. Influence of filler dispersion on mechanical behavior with large-scale coarse-grained molecular dynamics simulation. *Technische Mechanik*, 38(1):41–54, 2018.

[Klü03] M. Klüppel. The role of disorder in filler reinforcement of elastomers on various length scales. *Advances in Polymer Science*, 164:1–86, 2003.

[KMAS96] L. Karasek, B. Meissner, S. Asai, and M. Sumita. Percolation concept : Polymer-filler gel formation, electrical conductivity and dynamic electrical properties of carbon-black-filled rubbers. *Polymer Journal*, 28(2):121–126, 1996.

[KMHX17] K. Nakajima, M. Ito, H. K. Nguyen, and X. Liang. Nanomechanics of the rubber-filler interface. *Rubber Chemistry and Technology*, 90(2):272–284, 2017.

[KMK14] M. Koishi, H. Miyajima, and N. Kowatari. Conceptual design of tires using multi-objective design exploration. *11th World Congress on Computational Mechanics, 5th European Conference on Computational Mechanics, and 6th European Conference on Computational Fluid Dynamics*, pages 3180–3189, 2014.

[KOT77] H. Kaga, K. Okamoto, and Y. Tozawa. Stress analysis of a tire under vertical load by a finite element method. *Tire Science and Technology*, 5(2):102–118, 1977.

[KWKF18] K. Kisamori, T. Washio, Y. Kameda, and R. Fujimaki. A rare and critical condition search technique and its application to telescope stray light analysis. *SIAM International Conference on Data Mining*, pages 567–575, 2018.

[KWPD+20] M. F. Kasim, D. Watson-Parris, L. Deaconu, S. Oliver, P. Hatfield, D. H. Froula, G. Gregori, M. Jarvis, S. Khatiwala, J. Korenaga, J. Topp-Mugglestone, E. Viezzer, and S. M. Vinko. Up to two billion times acceleration of scientific simulations with deep neural architecture search. *APS Division of Plasma Physics Meeting 2020*, pages 1–10, 2020.

[LBBH98] Y. LeCun, L. Bottou, Y. Bengio, and P. Haffner. Gradient-based learning applied to document recognition. *Proceedings of the IEEE*, pages 2278–2323, 1998.

[LBXY19] T. Lookman, P. V. Balachandran, D. Xue, and R. Yuan. Active learning in materials science with emphasis on adaptive sampling using uncertainties for targeted design. *npj Computational Materials*, 5(21):1–17, 2019.

[LCY14] M. Lin, Q. Chen, and S. Yan. Network in network. *2nd International Conference on Learning Representations, ICLR 2014 - Conference Track Proceedings*, pages 1–10, 2014.

[LHA+21] K. Linka, M. Hillgärtner, K. P. Abdolazizi, R. C. Aydin, M. Itskov, and C. J. Cyron. Constitutive artificial neural networks: A fast and general approach to predictive data-driven constitutive modeling by deep learning. *Journal of Computational Physics*, 429(2):1–17, 2021.

[LK12] H. Lorenz and M. Klüppel. Microstructure-based modelling of arbitrary deformation histories of filler-reinforced elastomers. *Journal of the Mechanics and Physics of Solids*, 60(11):1842–1861, 2012.

[LK17] M. I. Latypov and S. R. Kalidindi. Data-driven reduced order models for effective yield strength and partitioning of strain in multiphase materials. *Journal of Computational Physics*, 346:242–261, 2017.

[LLJ+22] J. Liu, B. Li, Y. Jiang, X. Zhang, G. Yu, C. Sun, and S. Zhao. Investigation of filler network percolation in carbon black (CB) filled hydrogenated butadiene-acrylonitrile rubber (HNBR). *Polymer Bulletin*, 79(21):1–10, 2022.

[LWK19] Z. Liu, C. T. Wu, and M. Koishi. Transfer learning of deep material network for seamless structure–property predictions. *Computational Mechanics*, 64(2):451–465, 2019.

[MF17] J. Matejka and G. Fitzmaurice. Same stats, different graphs: Generating datasets with varied appearance and identical statistics through simulated annealing. *Conference on Human Factors in Computing Systems*, 1:1290–1294, 2017.

[MHN13] A. L. Maas, A. Y. Hannun, and A. Y. Ng. Rectifier nonlinearities improve neural network acoustic models. *in ICML Workshop on Deep Learning for Audio, Speech and Language Processing*, pages 1–6, 2013.

[Mih15] S. Mihara. Insight into chemical reaction and reinforcement mechanism of silica filled rubber during processing. *Nippon Gomu Kyokaishi*, 88(10):425–430, 2015.

[MNW+21] T. Miyata, T. Nagao, D. Watanabe, A. Kumagai, K. Akutagawa, H. Morita, and H. Jinnai. Nanoscale stress distribution in silica-nanoparticle-filled rubber as observed by transmission electron microscopy: Implications for tire application. *Applied Nano Materials*, 4(5):4452–4461, 2021.

[Moc89] J. Mockus. *Bayesian approach to global optimization: theory and applications*. Springer, 1989.

[MP16] G. J. Mulholland and S. P. Paradiso. Perspective: Materials informatics across the product lifecycle: Selection, manufacturing, and certification. *APL Materials*, 4(053207):1–7, 2016.

[Nak11] Y. Nakajima. Application of computational mechanics to tire design-yesterday, today, and tomorrow. *Tire Science and Technology*, 39(4):223–244, 2011.

[OHK18] I. Obayashi, Y. Hiraoka, and M. Kimura. Persistence diagrams with linear machine learning models. *Journal of Applied and Computational Topology*, 1(3-4):421–449, 2018.

[Pie12] H. O. Pierson. *Handbook of carbon, graphite, diamonds and fullerenes*. William Andrew, 2012.

[PK20] J. Plagge and M. Klüppel. Micromechanics of stress-softening and hysteresis of filler reinforced elastomers with applications to thermo-oxidative aging. *Polymers*, 12(6):1350, 2020.

[Pli97] S. Plimpton. Short-range molecular dynamics. *Journal of Computational Physics*, 117(6):1–42, 1997.

[PLW19] X. Peng, L. Li, and F. Y. Wang. Accelerating minibatch stochastic gradient descent using typicality sampling. *IEEE Transactions on Neural Networks and Learning Systems*, pages 1–11, 2019.

[PRS+17] S. P. Patil, A. Rege, Sagardas, M. Itskov, and B. Markert. Mechanics of nanostructured porous silica aerogel resulting from molecular dynamics simulations. *Journal of Physical Chemistry B*, 121(22):5660–5668, 2017.

[PS21] W. Pezeshkian and J. M. Siewert. Simulating realistic membrane shapes. *Curr Opin Cell Biol.*, 71:103–111, 2021.

[pyt] PyTorch. Available online: https://pytorch.org/.

[R.6] R. F. Egerton. *Electron energy-loss spectroscopy in the electron microscope*. 1996.

[RLK19] J. M. Rickman, T. Lookman, and S. V. Kalinin. Materials informatics: From the atomic-level to the continuum. *Acta Materialia*, 168(15):473–510, 2019.

[RM51] H. Robbins and S. Monro. A stochastic approximation method. *The Annals of Mathematical Statistics*, 22(3):400–407, 1951.

[RME06] G. Raos, M. Moreno, and S. Elli. Computational experiments on filled rubber viscoelasticity: What is the role of particle - Particle interactions? *Macromolecules*, 39(19):6744–6751, 2006.

[SBS03] J. S. Smith, D. Bedrov, and G. D. Smith. A molecular dynamics simulation study of nanoparticle interactions in a model polymer-nanoparticle composite. *Composites Science and Technology*, 63(11):1599–1605, 2003.

[SDG03] F. W. Starr, J. F. Douglas, and S. C. Glotzer. Origin of particle clustering in a simulated polymer nanocomposite and its impact on rheology. *Journal of Chemical Physics*, 119(3):1777–1788, 2003.

[SLA12] J. Snoek, H. Larochelle, and R. P. Adams. Practical bayesian optimization of machine learning algorithms. *Advances in Neural Information Processing Systems*, 25:1–9, 2012.

[Tak13] M. Takenaka. Analysis of structures of rubber-filler systems with combined scattering methods. *Polymer Journal*, 45(1):10–19, 2013.

[TAP+19] P. M. Tagade, S. P. Adiga, S. Pandian, M. S. Park, K. S. Hariharan, and S. M. Kolake. Attribute driven inverse materials design using deep learning Bayesian framework. *npj Computational Materials*, 5(127):1–14, 2019.

[TBC88] S. Torquato, J. D. Beasley, and Y. C. Chiew. Two-point cluster function for continuum percolation. *The Journal of Chemical Physics*, 88(10):6540–6547, 1988.

[TM16] J. Tolles and W. J. Meurer. Logistic regression relating patient characteristics to outcomes. *JAMA*, 16(5):533–534, 2016.

[TNSM19] T. Hashimoto, N. Amino, S. Nishitsuji, and M. Takenaka. Hierarchically self-organized filler particles in polymers: cascade evolution of dissipative structures to ordered structures. *Polymer Journal*, 51(2):109–130, 2019.

[VHK09] T. A. Vilgis, G. Heinrich, and M. Klüppel. *Reinforcement of polymer nano-composites: Theory, experiments and applications*. Cambridge University Press, 2009.

[WG15] H. Wu and X. Gu. Towards dropout training for convolutional neural networks. *Neural Networks*, 71:1–10, 2015.

[WM04] M. Weyland and P.A. Midgley. Electron tomography. *Materials Today*, 7(12):32–40, 2004.

[WOW+19] J. Wang, S. Olsson, C. Wehmeyer, A. Pérez, N. E. Charron, G. De Fabritiis, F. Noé, and C. Clementi. Machine learning of coarse-grained molecular dynamics force fields. *ACS Central Science*, 5:755–767, 2019.

[YCHB21] Z. Yang, Y. Chi-Hua, and M. J. Buehler. Deep learning model to predict complex stress and strain fields in hierarchical composites. *Science Advances*, 7(15):1–10, 2021.

[YQ14] S. Yang and J. Qu. Coarse-grained molecular dynamics simulations of the tensile behavior of a thermosetting polymer. *Physical Review E*, 90(012601):1–8, 2014.

[YYAB+18] Z. Yang, Y. C. Yabansu, R. Al-Bahrani, W. Liao, A. N. Choudhary, S. R. Kalidindi, and A. Agrawal. Deep learning approaches for mining

structure-property linkages in high contrast composites from simulation datasets. *Computational Materials Science*, 151:278–287, 2018.

[YYJ+19] Z. Yang, Y. C. Yabansu, D. Jha, W. Liao, A. N. Choudhary, S. R. Kalidindi, and A. Agrawal. Establishing structure-property localization linkages for elastic deformation of three-dimensional high contrast composites using deep learning approaches. *Acta Materialia*, 166:335–345, 2019.

[ZC05] A. Zomorodian and G. Carlsson. Computing persistent homology. *Discrete and Computational Geometry*, 33(2):249–274, 2005.

[ZHW+18] L. Zhang, J. Han, H. Wang, R. Car, and E. Weinan. DeePCG: Constructing coarse-grained models via deep neural networks. *Journal of Chemical Physics*, 149(3):1–10, 2018.

Appendix

A CGMD simulation

We employed the Kremer-Grest model [KG90] representing the Rouse chain, which described the conformational dynamics of an ideal chain, for a modeling of polymer chains. This model has been widely used as a coarse-grained model of a polymer chain [HMDT16], because this model consisting of a bead and a spring can simulate dynamics of the polymer chains in wider range of time/space scale than the traditional molecular dynamics simulation reproducing a detailed molecular structure. A polymer chain model consisted of bead-necklace chains of length 20,000 beads and included 60,000 cross-linking bonds, and polymer beads were distributed at density of 0.85 following the previous report [KG90]. Figure A.1(a) shows a polymer chain. The cross-linking bonds were created by cross-linking reaction simulations representing a sulfur vulcanization [GEK00] [DB93], which was conducted after putting filler particles into the polymer melt system. The interaction between polymer beads was modeled using Lennard-Jones potential as follows:

$$U_{LJ}(r) = 4\varepsilon\left[\left(\frac{\upsilon}{r}\right)^{12} - \left(\frac{\upsilon}{r}\right)^{6} + \frac{1}{4}\right] \tag{A.1}$$

where r,ε, and υ denote the distance between beads, the strength of the interaction, and the diameter of the sphere beads, respectively. Both ε and υ were set to 1.0 in this study. The cutoff distance r_c which was the valid range of the interaction potential was set to $2^{\frac{1}{6}}$. This value meant repulsive interaction. The bonds, U_{bond}, connecting adjacent polymer beads were modeled using finite extensible nonlinear elastic potential, U_{FENE}, as follows:

$$U_{bond}(r) = U_{FENE}(r) + U_{LJ}(r) \tag{A.2}$$

$$U_{FENE}(r) = -\frac{1}{2}kR_0^2 ln\left[1 - \left(\frac{r}{R_0}\right)^2\right] \tag{A.3}$$

where $k = 30$ and $R_0 = 1.5$ stand for spring constant and finite extended length of bonds, respectively. A filler was a solid particle combined beads by bonds. The

bead and bond were identical with those used for the polymer chains, and the interaction between filler beads was modeled by Lennard-Jones potential described in Equation (A.1) with cutoff distance $r_c = 2^{\frac{1}{6}}$. Figure A.1(b) presents a filler particle. The interaction between the filler beads and polymer bead was modeled by the Lennard-Jones potential of Equation (A.1) with cutoff distance $r_c = 2.5$. This value represented attractive interaction which was the interaction between polymer and carbon-black (one of the most famous filler) [DB93]. The strength of the interaction ε was set to 15.0.

The dynamics of the beads were described with a Langevin equation as given by:

$$m\frac{d^2x}{dt^2} = F - m\zeta\frac{dx}{dt} + W \tag{A.4}$$

where m, x, t, F, ζ, and W were a mass of the bead, a coordinate of the bead, time, force interacting on the bead, a friction constant, and Gaussian white noise, respectively. The mass m was set to 1 in this study. The stress-strain response was simulated under the uniaxial deformation at the strain velocity of 0.005 $[\sigma/\tau]$ that deformed the polymers in rubbery state under the NVT ensemble, in which the velocity-Verlet algorithm was used for numerical integrations of the Langevin equation. Here, σ and τ were unit length and unit time used in the CGMD, respectively. The time step of numerical integration and temperature were set to $\delta t = 0.006$ and $T = 1$, respectively. The friction constant of the Langevin equation in Equation (A.4) was $\zeta = 0.5$. The simulation was carried out under the periodic boundary condition.

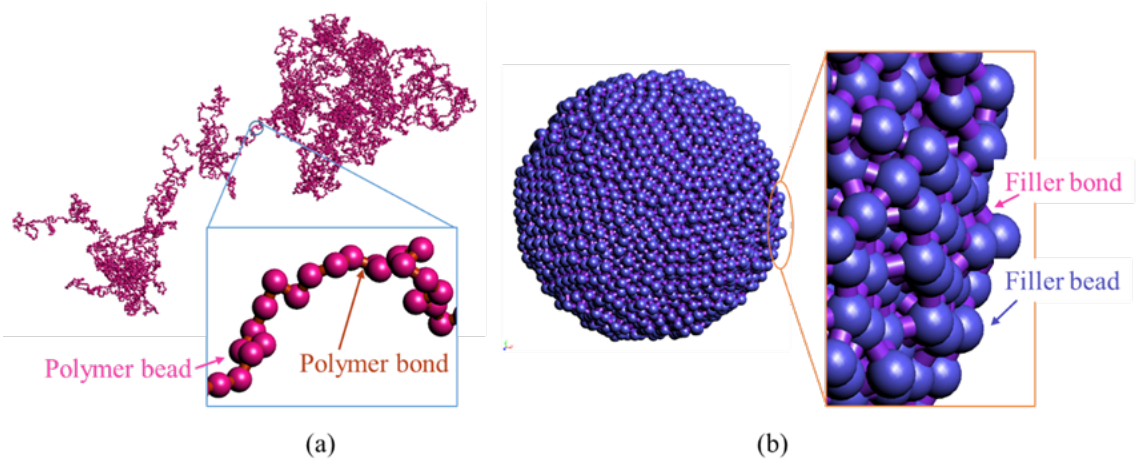


Figure A.1: Example of CGMD model: (a) presents the polymer chain consisted of 20,000 beads. The pink spheres represent the polymer beads. The orange cylinders represent the polymer bond defined by Equation (A.2). The interaction between polymer beads are represented by Lennard-Jones potential described in Equation (A.1). (b) presents the filler particle. Spheres colored in dark purple represent the filler bead, and light purple cylinders represent the bond connecting adjacent filler beads. The interaction between beads and bond potential are identical with those used for the polymer chains.

List of Publications

Journal Papers

J-1 T. Kojima and M. Koishi. Influence of filler dispersion on mechanical behavior with large-scale coarse-grained molecular dynamics simulation. *Technische Mechanik*, 38(1): 41-54, 2018.

J-2 T. Kojima, T. Washio, S. Hara, and M. Koishi. Synthesis of computer simulation and machine learning for achieving the best material properties of filled rubber. *Scientific Reports*, 10(18127): 1–11, 2020.

J-3 T. Kojima and M. Koishi. Mechanisms of mechanical behavior of filled rubber by coarse-grained molecular dynamics simulations. *Tire Science and Technology*, 48(2):78–106, 2020.

J-4 T. Kojima, T. Washio, S. Hara, M. Koishi, and N. Amino. Analysis on microstructure–property linkages of filled rubber using machine learning and molecular dynamics simulations. *Polymers*, 13(16); 2683, 2021.

J-5 T. Kojima, T. Washio, S. Hara, and M. Koishi. Search strategy for rare microstructure to optimize material properties of filled rubber using machine learning based simulation. *Computational Materials Science*, 204(1112007), 2022.

Conference

C-1 T. Kojima, T. Washio, S. Hara, and M. Koishi. Search strategy for rare microstructure to optimize material properties of filled rubber using machine learning based simulation. *Mechanistic Machine Learning and Digital Twins for Computational Science, Engineering Technology*, September 26-29, 2021.